



저작자표시-비영리-변경금지 2.0 대한민국

이용자는 아래의 조건을 따르는 경우에 한하여 자유롭게

- 이 저작물을 복제, 배포, 전송, 전시, 공연 및 방송할 수 있습니다.

다음과 같은 조건을 따라야 합니다:



저작자표시. 귀하는 원저작자를 표시하여야 합니다.



비영리. 귀하는 이 저작물을 영리 목적으로 이용할 수 없습니다.



변경금지. 귀하는 이 저작물을 개작, 변형 또는 가공할 수 없습니다.

- 귀하는, 이 저작물의 재이용이나 배포의 경우, 이 저작물에 적용된 이용허락조건을 명확하게 나타내어야 합니다.
- 저작권자로부터 별도의 허가를 받으면 이러한 조건들은 적용되지 않습니다.

저작권법에 따른 이용자의 권리는 위의 내용에 의하여 영향을 받지 않습니다.

이것은 [이용허락규약\(Legal Code\)](#)을 이해하기 쉽게 요약한 것입니다.

[Disclaimer](#)

공학박사학위논문

Studies on Molecular Design and Synthesis of Novel Thermally Activated Delayed Fluorescence Materials for Organic Light Emitting Diodes

유기발광다이오드를 위한 신규 열 활성화 지연 형광체의

분자 설계 및 합성에 관한 연구

2023년 2월

서울대학교 대학원

재료공학부

유 치 현

**Studies on Molecular Design and Synthesis of Novel
Thermally Activated Delayed Fluorescence Materials for
Organic Light Emitting Diodes**

유기발광다이오드를 위한 신규 열 활성화 지연 형광체의

분자 설계 및 합성에 관한 연구

지도 교수 박 수 영

2023년 2월

서울대학교 대학원

재료공학부

유 치 현

위 원 장 안 철 희 (인)

부위원장 박 수 영 (인)

위 원 박 종 욱 (인)

위 원 권 민 상 (인)

위 원 박 상 규 (인)

**Studies on Molecular Design and Synthesis of Novel
Thermally Activated Delayed Fluorescence Materials for
Organic Light Emitting Diodes**

A THESIS SUBMITTED IN PARTIAL FULFILLMENT OF
THE REQUESTMENTS FOR THE DEGREE OF
DOCTOR OF PHILOSOPHY
IN ENGINEERING AT THE GRADUATE SCHOOL OF
SEOUL NATIONAL UNIVERSITY

February 2023

By

Chi Hyun Ryoo

Supervisor

Prof. Soo Young Park

Abstract

Molecular Design and Synthesis of Novel Thermally Activated Delayed Fluorescence Materials for Organic Light Emitting Diodes

Chi Hyun Ryoo

Department of Materials Science and Engineering

The Graduate School

Seoul National University

For the past two decades, organic light emitting diodes (OLEDs) have drawn tremendous attention for the next generation of displays. In the light emitting materials or OLEDs, phosphors are in the spotlight as high-efficiency OLED light emitting materials because it can boost the internal quantum efficiency (IQE) of electroluminescence up to 100%. Red and green emitting phosphors have been developed with good color purity and high quantum efficiency. However, in the blue region, development of new emitter is still demanded due to the instability of the material, making it difficult to commercialize blue OLED.

Recently, studies on new materials using variety of mechanism overcoming the limitations of existing emitters (fluorescence, phosphorescence) are conducted very actively. Especially, studies on thermally activated delayed fluorescence (TADF) emitters achieving 100% IQE by using TADF phenomenon is drawing tremendous attention in the field of OLEDs. In this study, I studied on molecular design and synthesis of novel thermally activated delayed fluorescence materials for organic light emitting diodes on the basis of these background.

In Chapter2, a series of indolo[3,2-b]indole (IDID) derivatives are designed as a novel structural platform for thermally activated delayed fluorescence (TADF) emitters. Intramolecular charge transfer (ICT)-type molecules consisting of IDID donor (D) and various acceptor (A) moieties are synthesized and characterized in the protocol of the systematical structure–property correlation. IDID derivatives exhibit high efficiency, prompt fluorescence as well as TADF with emission ranges tuned by the chemical structure of the acceptor units. Interestingly, almost all of the IDID derivatives show an identical energy level of the lowest triplet excited state (T_1) attributed to the locally excited triplet state of the IDID backbone ($^3LE_{ID}$), while that of their lowest singlet excited state (S_1) is largely tuned by varying the acceptor units. Thus, we demonstrate the underlying mechanism in terms of the molecular engineering. Among the compounds, Tria-phIDID and BP-phIDID generate efficient delayed fluorescence based on the small energy gap between the lowest singlet and triplet excited states (ΔE_{ST}). Organic light-emitting diodes with these Tria-phIDID and BP-phIDID as a dopant in the emitting layer show highly efficient electroluminescence with maximum external quantum efficiencies of 20.8% and 13.9%, respectively.

In Chapter3, a molecular structural approach is applied by introducing various substituent groups (X) to explore the structure-property correlation of TADF mechanism at one hand and develop blue TADF materials on the other hand. Thanks to the simultaneous fine tuning of the energy states, D-A-X emitters show blue region emissions from 446 to 487 nm and exhibit high rate constants of reverse intersystem crossing (k_{rISC}) from $0.76 \times 10^6 \text{ s}^{-1}$ to $2.13 \times 10^6 \text{ s}^{-1}$. Organic light emitting diodes (OLEDs) based D-A-X emitters exhibit efficient external quantum efficiency from 17.2% to 23.9%. Furthermore, the theoretical analysis of spin-flip transitions between states of various nature reveals that the highest rISC rates can be achieved by the increase of charge-transfer (CT) strength and enhancement of direct transition between triplet (3CT) and singlet (1CT) charge transfer states. Rotational tolerance of dihedral

angle, low energy gap and low reorganization energy between the ^3CT and ^1CT states provided fast rISC even when triplet states of different (LE) nature had much higher energy not to enable the three-level interaction. By both experimental and theoretical methods, our investigations reveal that for the design of efficient TADF-OLED emitters, the enhancement of the ^3CT - ^1CT transition is as much important as that of ^3LE - ^1CT one.

In Chapter4, a molecular structural approach is applied by increasing ICT strength to develop deep blue TADF materials. We designed and synthesized the blue TADF material by using CN substituted sulfone acceptor. DPS-CBZ exhibit UV emission and just a single component of fluorescence lifetime. On the other hand, thanks to ideally control of the energy states, CN substituted emitters show blue region emissions from 425 to 447 nm and exhibit delayed lifetime. Organic light emitting diodes (OLEDs) based blue emitters exhibit efficient external quantum efficiency from 17.7% to 22.6%.

In Chapter5, a series of BOCBZ derivatives are designed and synthesized to develop deep blue MR type TADF materials. BOCBZ emitters show blue region emissions from 444 to 455 nm with narrow FWHM. Particularly, compounds with the tetraphenylsilane (-Si) moiety RISC rate faster than that of the BOCBZ compounds, indicating that triplet up-conversion occurs efficiently in the case of the tetraphenylsilane-substituted materials. It could be forming an additional triplet state enhancing SOC between S_1 and T_n state. Additionally, $\langle S_1 | \hat{H}_{\text{SOC}} | T_1 \rangle$ of 1tbuBOCBZ-Si and 3tbuBOCBZ-Si was improved by the heavy-atom effect of Si atoms, similar to S and Se atoms in MR-TADF.

Keywords: OLED, TADF, Multiple resonance, Blue dopant, Photoluminescence

Student Number: 2015-22772

Contents

Abstracts.....	i
List of Schemes.....	vii
List of Tables.....	viii
List of Figures.....	ix
Chapter 1. Introduction.....	1
1.1 OLED.....	1
1.2. Emitters for organic light-emitting diodes.....	2
1.2.1. Fluorescence emitters.....	3
1.2.2 Phosphorescence emitters.....	4
1.2.3 TADF emitters.....	4
1.2.4 Multiple resonance type TADF.....	6
1.3 References.....	8
Chapter 2. Structure–Property Correlation in Luminescent Indolo[3,2-b]indole (IDID) Derivatives : Unraveling the Mechanism of High Efficiency Thermally Activated Delayed Fluorescence (TADF).....	10
2.1 Introduction.....	10
2.2 Experimental Methods.....	12
2.2.1 Synthesis of Materials.....	12
2.2.2 Characterization.....	17
2.2.3 Device fabrication and Measurement.....	18
2.3 Results and Discussion.....	19
2.3.1 Material Design.....	19
2.3.2 Density Functional Theory Calculations.....	19
2.3.3 Photophysical Properties.....	20

2.3.4 Electrochemical properties.....	28
2.3.5 OLED Performances.....	30
2.4 Conclusion.....	32
2.5. References.....	33
Chapter 3. Systematic Substituent Control in Blue Thermally-Activated Delayed Fluorescence (TADF) Emitters: Unraveling the Role of Direct Intersystem Crossing between the Same Charge-Transfer States.....	36
3.1 Introduction.....	36
3.2 Experimental Methods.....	40
3.2.1 Synthesis of Materials.....	40
3.2.2 General methods.....	47
3.2.3 Determination of photophysical parameters.....	48
3.2.4 Theoretical Calculations.....	49
3.2.5 Devices fabrication and characterization.....	50
3.3 Results and Discussion.....	50
3.3.1 Material Design.....	50
3.3.2 Electrochemical Properties.....	51
3.3.3 Photophysical Properties.....	52
3.3.4 Fluorescence decay profiles and their exciton dynamics.....	58
3.3.5 OLED Performances.....	64
3.3.6 Theoretical studies on rISC rates and TADF model.....	70
3.4 Conclusion.....	80
3.5 References.....	82
Chapter 4. Design of deep Blue TADF Materials using CN Substituted sulfone units.....	86
4.1. Introduction.....	86
4.2 Experimental Methods.....	88
4.2.1 Synthesis of Materials.....	88

4.2.2 Characterization.....	88
4.2.3 Device fabrication and Measurement.....	89
4.3 Results and Discussion.....	90
4.3.1 Density Functional Theory Calculations.....	90
4.3.2 Electrochemical Properties.....	93
4.3.3 Photophysical Properties.....	95
4.3.4 OLED Performances.....	101
4.4 Conclusion.....	105
4.5 References.....	106
Chapter 5. Multiple Resonance Thermally Activated Delayed Fluorescence Enhanced by Tetraphenyl Silyl Group.....	108
5.1. Introduction.....	108
5.2 Experimental Methods.....	110
5.2.1 Synthesis of Materials.....	111
5.2.2 Characterization.....	111
5.3 Results and Discussion.....	112
5.3.1 Density Functional Theory Calculations.....	112
5.3.2 Electrochemical Properties.....	118
5.3.3 Photophysical Properties.....	119
5.4 Conclusion.....	126
5.5 Reference.....	127
국 문 초 록 (Korean Abstract).....	129

List of schemes

Scheme 2.1 Synthetic routes of IDID derivatives.

Scheme 2.2. Schematic illustration of emission mechanism of IDID derivatives.

Scheme 3.1 Synthetic routes of D-A-X derivatives and their chemical structures.

Scheme 4.1 Synthetic routes of TADF materials

Scheme 5.1 Synthetic routes of MR TADF materials.

Scheme 5.2 Synthetic routes of MR TADF materials.

List of tables

Table 2.1 Photophysical and Electrical Properties of the IDID derivatives.

Table 2.2 Device performances of the IDID based TADF-OLEDs.

Table 3.1 The summary of physical and photophysical properties of D-A-X derivatives.

Table 3.2 The summary of rate constants of D-A-X derivatives in DPEPO films.

Table 3.3. Device performances of the D-A-X TADF-OLEDs.

Table 3.4 Devices performances of DPS-based TADF emitters and their molecular structures

Table 3.5 Rate constants of triplet-singlet transitions

Table 4.1 DFT calculation of target materials.

Table 4.2 Cyclic voltammetry of target materials.

Table 4.3 The summary of physical and photophysical properties of TADF materials.

Table 4.4 The summary of rate constants of TADF materials in DPEPO films.

Table 4.5 Device performances of the target materials.

Table 5.1 DFT-calculation of target materials.

Table 5.2 Cyclic voltammetry of target materials.

Table 5.3 The summary of physical and photophysical properties.

Table 5.4 The summary of rate constants of BOCBZ derivatives in PMMA films.

List of Figures

Figure 1.1 (a) OLED working principle (b) conventional OLED structure

Figure 1.2 Emission mechanism in first-generation (fluorescent), second-generation (phosphorescent), and third-generation (TADF) emitters

Figure 1.3 Illustration of TADF mechanism

Figure 1.4 Schematic presentation of intramolecular D-A type TADF molecules

Figure 1.5 Multiple resonance type TADF

Figure 2.1 HOMO and LUMO distribution and energy difference (ΔE_{ST}) between the first singlet (S_1) and triplet (T_1) states of IDID derivatives.

Figure 2.2 Photophysical properties of the IDID molecules.

Figure 2.3 Photoluminescence decay traces of IDID derivatives

Figure 2.4 a) The phosphorescence spectra of IDID derivatives in toluene solution at 77 K. b) Fluorescence and phosphorescence spectra in toluene solution of BP-phIDID, c) Tria-phIDID, d) NO₂-phIDID.

Figure 2.5 Cyclic voltammetry (CV) of IDID derivatives. Solution samples were prepared 5 x 10⁻³ M solution in methylene chloride (Inset: CV of ferrocene).

Figure 2.6 Device performance of IDID TADF materials. (a) *J*-*V*-*L* characteristics, (b) external quantum efficiency, (c) EL spectra for OLEDs

Figure 3.1 Structures of D-A-X type derivatives.

Figure 3.2 (a) Cyclic voltammetry of D-A-X materials. (b) Correlation of LUMO energy levels with Hammett constant. (c) HOMO and LUMO energy levels for D-A-X derivatives.

Figure 3.3 Optical properties of D-A-X derivatives. (a) absorption spectra (toluene, $c=1 \times 10^{-5}$ M) (b) normalized photoluminescence (toluene, $c=1 \times 10^{-5}$ M) (c) normalized photoluminescence (10 wt% in DPEPO film) (d) correlation of photoluminescence maximum with Hammett constant (10 wt% in DPEPO film)

Figure 3.4 (a) Temperature-dependent PL decay spectra (10 wt% in DPEPO film) (b) The rate constants of radiative process (10 wt% in DPEPO film)

Figure 3.5 Prompt fluorescence (PF) and phosphorescence (50 ms delay time) spectra of selected emitters **D-A-X**, acceptor **A-X**, and donor (**D-Ph**) molecules in frozen toluene at 78 K.

Figure 3.6 Fluorescence and phosphorescence spectra in 10 wt% DPEPO film

Figure 3.7 Correlations of the logarithm of ISC (a,b) and rISC (c,d) rate constants with the energy gaps

Figure 3.8 The energy-level diagram of the devices and the molecular structure of used materials

Figure 3.9 Device performance of D-A-X TADF materials. (a) EL spectra for OLEDs (b) external quantum efficiency (c) CIE coordinates of OLEDs using D-A-X emitters (d) performance of DPS based OLED

Figure 3.10 IVL characteristics of the devices

Figure 3.11 Probability of rotamers in S_0 -state and dependence of the S_0 -state energy on the dihedral angle θ .

Figure 3.12 Molecular orbitals involved in the key electronic transitions on the example of DMAC-DPS-Pi (left) and diDMAC-DPS (right).

Figure 3.13 The dependences of energies of the lowest excited electronic states (a, b, c), energy gaps (d), sum of reorganization energies (e), and SOCME constants (f) of $^3\text{CT}-^1\text{CT}$ transition on the dihedral angle θ .

Figure 3.14 (a) Comparison of experimental rISC rate constants with the calculated ones of the $^3\text{CT}-^1\text{CT}$ transition and the sum of rate constants of $^3\text{CT}-^1\text{CT}$ and $^3\text{LE}-^1\text{CT}$ transitions multiplied by molar concentration of molecules in respective triplet states. Represent the rISC rate constants in each rotamer via $^3\text{CT}-^1\text{CT}$ (b) and $^3\text{LE}-^1\text{CT}$ (c) mechanism, respectively, depending on the deviation of θ from the optimal value.

Figure 4.1 Structures of DPS-CBZ

Figure 4.2 Optimized molecular geometries and the dihedral angle.

Figure 4.3 Optimized molecular geometries with HOMO and LUMO.

Figure 4.4 Cyclic voltammetry of target materials.

Figure 4.5 Absorption spectra of target molecules. (toluene, $c=1\times 10^{-5}\text{M}$)

Figure 4.6 Normalized photoluminescence spectra of target molecules. (toluene, $c=1\times 10^{-5}\text{M}$)

Figure 4.7 Normalized photoluminescence spectra of target molecules.

(10 wt% in DPEPO film)

Figure 4.8 Temperature-dependent PL decay spectra (10 wt% in PMMA film)

Figure 4.9 Fluorescence and phosphorescence spectra (toluene, $c=1\times 10^{-5}\text{M}$)

Figure 4.10 the energy-level diagram of the devices and the molecular structure

Figure 4.11 External quantum efficiency of OLED devices

Figure 4.12 *J-V-L* characteristics of OLED devices

Figure 4.13 EL spectra for OLED devices

Figure 5.1 Optimized molecular geometries of BOCBZ derivatives.

Figure 5.2 Optimized molecular geometries with HOMO and LUMO.

Figure 5.3 Transition energies for S_1 and T_n states ($n=1,2,3$ and 4) and associated SOC matrix elements.

Figure 5.4 Cyclic voltammetry of target materials.

Figure 5.5 Absorption spectra of target molecules. (toluene, $c=1 \times 10^{-5} \text{ M}$)

Figure 5.6 Normalized photoluminescence spectra of target molecules. (toluene, $c=1 \times 10^{-5} \text{ M}$)

Figure 5.7 Normalized photoluminescence spectra of target molecules.

(1 wt% in PMMA film)

Figure 5.8 Temperature-dependent PL decay spectra (1 wt% in PMMA film).

Figure 5.9 Fluorescence and phosphorescence spectra (toluene, $c=1 \times 10^{-5} \text{ M}$)

Chapter 1. Introduction

1.1 OLED

Organic light-emitting diode (OLED) is a light-emitting diode with the capability to produce light within the organic emissive layers under external voltage. Since the pioneering work of Tang and Van Slyke, OLEDs has received tremendous attention from both academia and industry.^[1] OLED has the advantages of facile preparation, light weight, low driving voltage, high brightness and fast response.^[2] Even more impressive is the flexible characteristics which able to use in foldable, flexible, and rollable displays.^[3] As a next-generation display, OLED has already been commercialized in mobile phones, smart watches and has recently expanded its application area to large TVs, lighting, and automobile displays.

In general, OLED has a multilayered structure as shown **Figure 1.1**, including hole injection layer (HIL), an anode, hole transport layer (HTL), emissive layer (EML), electron transport layer (ETL), electron injection layer (EIL) and cathode.^[4] Since there is about 1 eV of energy barrier between cathode and emitting layer and equally to anode and emitting layer, lowering the energy barrier by introducing multi-layer structure is essential for the device with a high-performance. An external voltage is applied to inject holes from the anode and electrons from the cathode connected to either side of the emitting layer. Holes inject into anode and transfers through HIL, HTL. Additionally, electrons inject into cathode and transfer through EIL, ETL to form exciton in EML. As a result, electroluminescence (EL) occurs when excitons are stabilized to a ground state in the EML layer.

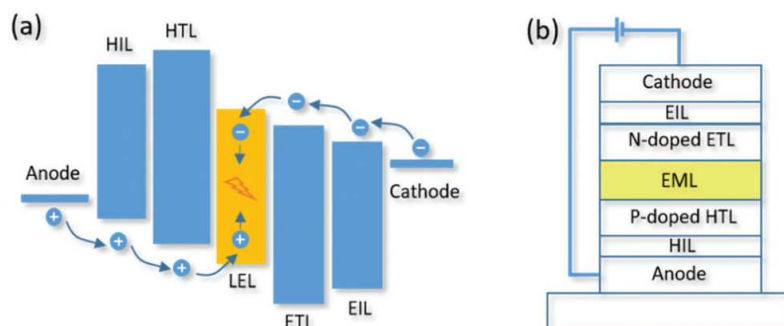


Figure 1.1 (a) OLED working principle (b) conventional OLED structure^[4]

1.2. Emitters for organic light-emitting diodes

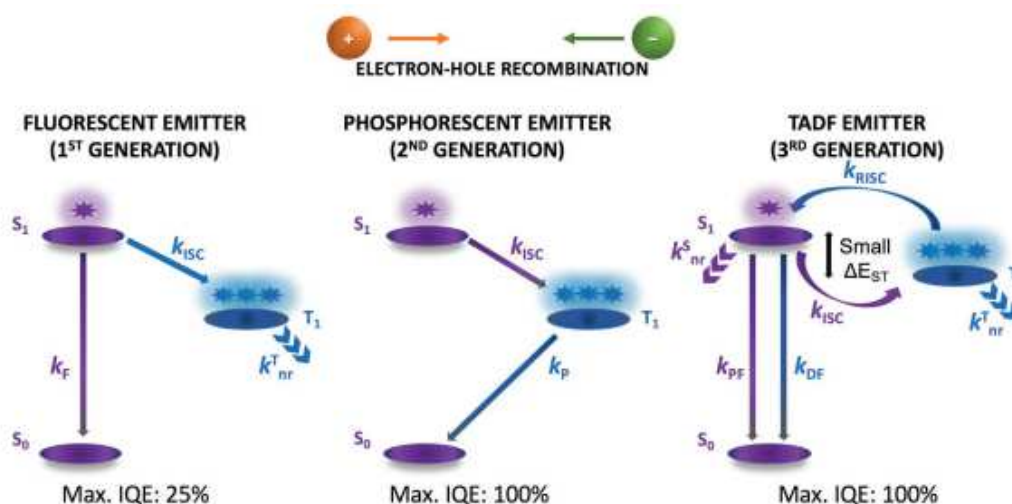


Figure 1.2 Emission mechanism in first-generation (fluorescent), second-generation (phosphorescent), and third-generation (TADF) emitters.^[5]

F = fluorescence; P = phosphorescence; PF = prompt fluorescence; DF = delayed fluorescence; ISC = intersystem crossing; RISC = reverse intersystem crossing; ΔE_{ST} = the energy difference between the first excited singlet and triplet states; nr = nonradiative.

1.2.1. Fluorescence emitters

Recombination of electrons and holes will generate singlet and triplet excitons with a ratio of 1:3 according to spin statistics.^[6] The maximum internal quantum efficiency (IQE) using conventional fluorescent emitters is around 25% due to utilizing only singlet excitons. Therefore, the maximum external quantum efficiency (EQE) can only reach roughly 5%, which can be described by the following equation:

$$EQE_{\max} = \eta_r \times \eta_{ST} \times \phi_{PL} \times \eta_{out} = IQE_{\max} \times \eta_{out}$$

where EQE_{\max} and IQE_{\max} are the maximum external quantum efficiency and the maximum internal quantum efficiency, respectively. η_r is the proportion of electron-hole recombination, which is supposed to be unity in the ideal case. η_{ST} is the fraction of radiative excitons, ϕ_{PL} is the photoluminescence quantum yield (PLQY) of the emitting layer, and η_{OUT} is the light out-coupling efficiency, which is around 20% for normal OLEDs with an ITO-based flat thin-film architecture. Regardless of the efficiency limitation, the fluorescent materials take advantage of long lifetimes, especially for stable blue emitters.

1.2.2 Phosphorescence emitters

Phosphorescence is essentially a slower process, but triplet states make up 75% of electro-generated excited states, so utilization of the triplet state to produce light should be important in achieving high efficiency OLEDs.^[7] The phosphorescent material containing heavy-metal complex uses triplet state excitons by heavy-atom effect, which strong spin-orbit coupling lead to singlet-triplet state mixing and removes the spin-forbidden nature of the radiative relaxation of the triplet state. However, the commonly used phosphorescence dopants including expensive metal, such as Ir or Pt, increase the price of commercial products. thus,

alternative materials or mechanisms are required. [8-10]

1.2.3 TADF emitters

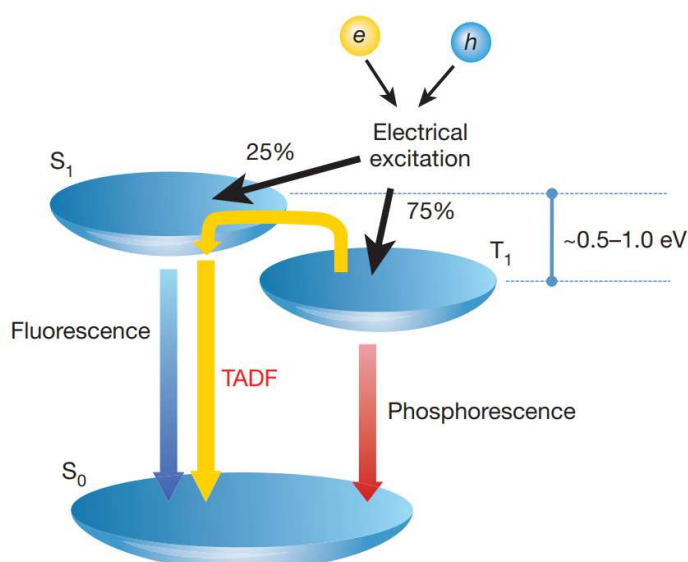


Figure 1.3 Illustration of TADF mechanism [11]

In 2012, Adachi et al proposed thermally activated delayed fluorescence (TADF) emitters. [11] Thermally activated delayed fluorescence (TADF) is drawing tremendous attention in the field of organic light emitting diodes (OLEDs) because it can boost the internal quantum efficiency (IQE) of electroluminescence up to 100% through the reverse intersystem crossing (RISC). [12,13] Theoretically, RISC occurs efficiently when energy difference (ΔE_{ST}) between the first excited singlet (S_1) and triplet (T_1) states is small enough. [14-16] To realize efficient TADF, Adachi et al. embodied molecular design rules of using intramolecular charge transfer (ICT) mechanism with bulky electron donor and/or acceptor units which spatially separate the highest occupied molecular orbital (HOMO) and lowest unoccupied molecular orbital (LUMO) to ensure minimized ΔE_{ST} . [17-21]

The ΔE_{ST} is defined as follows:

$$E_S = E + K + J$$

$$E_T = E + K - J$$

$$\Delta E_{ST} = E_S - E_T = 2J$$

where E is the orbital energy, K is the electron repulsion energy and J is the exchange energy.^[22]

As predicted from quantum theory, J is relative to the overlap of the spatial wave function of the HOMO and LUMO levels in organic molecules. Therefore, ΔE_{ST} can be minimized by spatial separation of the electron densities of the frontier orbitals.

The D-A type TADF molecules have a donor and an acceptor part connected by a suitable bridge. In such molecular systems, the excited states are attained by intramolecular charge transfer, generally resulting in virtually low PL efficiency due to limited frontier orbital overlap. Therefore, the choice of the donor and acceptor components is crucial to get the efficient TADF emitters.

Even though donor-acceptor (D-A) type TADF materials have showed great performance, these CT characteristic emitters have problems of color purity due to broad emission spectra with a wide full width at half- maximum (FWHMs) and hard to realize the deep blue emission with CIE_y < 0.08.

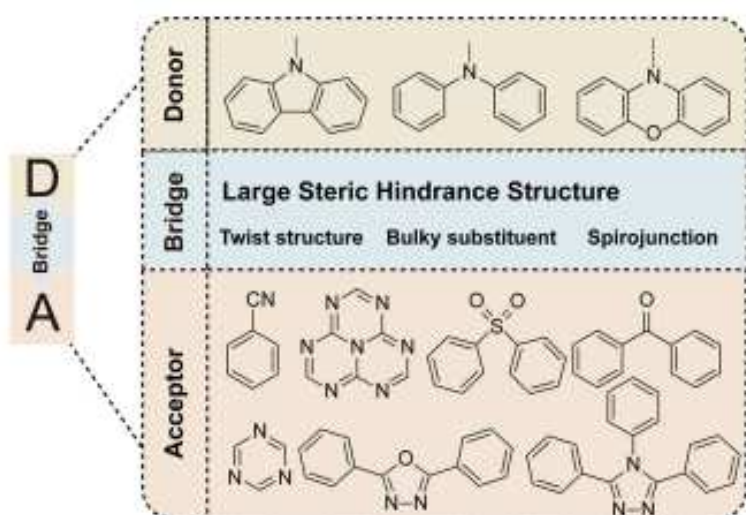


Figure 1.4 Schematic presentation of intramolecular D-A type TADF molecules ^[22]

1.2.4 Multiple resonance type TADF

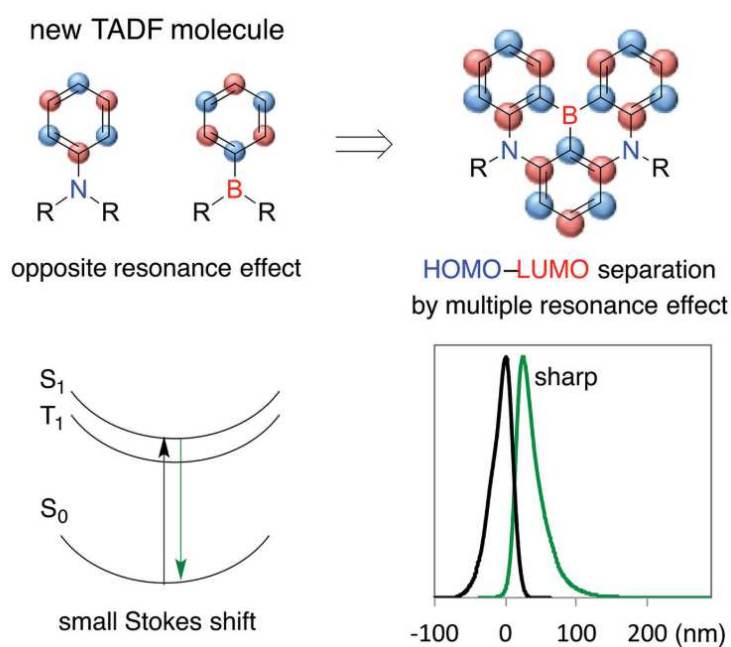


Figure 1.5 Multiple resonance type TADF ^[23]

Hatakeyama et al. demonstrated new type of molecular design strategy by using a multiple resonance (MR) effect. It has rigid π -conjugated structure consisting of an electron-deficient

boron atom and an electron-rich nitrogen atom, exhibiting alternating HOMO and LUMO distributions by the resonance effect.^[23] The rigid backbone structure suppressed vibrational motions and guarantee a small full width at half-maximum (FWHM). The first MR-TADF materials, DABNA-1 and DABNA-2, showed blue emission of 459 and 469 nm for DABNA-1 and DABNA-2, respectively. Also, they exhibited high EQE values of 13.5% and 20.2% with color coordinates of (0.13, 0.09) and (0.12, 0.13). Since then, a number of MR-TADF materials have been developed and ν -DABNA developed by Hatakeyama group. ν -DABNA is a fused form of two boron atoms and six nitrogen atoms and it exhibited a maximum emission wavelength of 469 nm and a half width of 18 nm, so it is known as the state-of-art blue light-emitting material.^[24]

1.3 References

- [1] C. W. Tang, S. A. VanSlyke, *Applied Physics Letters* **1987**, *51*, 913-915.
- [2] T. Tsujimura, W. Zhu, S. Mizukoshi, N. Mori, K. Miwa, S. Ono, Y. Maekawa, K. Kawabe, M. Kohno, SID Symposium Digest of Technical Papers 2007, 38, 84-88.
- [3] S.-M. Lee, J. H. Kwon, S. Kwon and K. C. Choi, *IEEE Transactions on Electron Devices*, 2017, **64**, 1922-1931.
- [4] S.-J. Zou, Y. Shen, F.-M. Xie, J.-D. Chen, Y.-Q. Li and J.-X. Tang, *Materials Chemistry Frontiers*, 2020, **4**, 788-820.
- [5] M. Y. Wong and E. Zysman-Colman, *Adv. Mater.* 2017, *29*, 1605444.
- [6] Z. Xu, B. Z. Tang, Y. Wang and D. Ma, *Journal of Materials Chemistry C*, 2020, **8**, 2614-2642.
- [7] M. A. Baldo, D. F. O'Brien, Y. You, A. Shoustikov, S. Sibley, M. E. Thompson and S. R. Forrest, *Nature*, 1998, **395**, 151-154.
- [8] J. R. L. a. R. Joseph, *Principles of fluorescence spectroscopy*, Springer Science & Business Media 2013.
- [9] F. B. V. Sivasubramaniam, S. Hanning, H. P. Loebl, V. van 24 Elsbergen, H. Boerner, U. Scherf and M. Kreyenschmidt, *J. Fluorine Chem.* 2009, 130.
- [10] A. H. a. B. K. n. S. Schmidbauer, *Adv. Mater.* 2013, 25.
- [11] H. Uoyama, K. Goushi, K. Shizu, H. Nomura and C. Adachi, *Nature*, 2012, **492**, 234-238.
- [12] H. Kaji, H. Suzuki, S. Kubo, T. Komino, C. Adachi, *Nat. Commun.* **2015**, *6*, 8476.
- [13] Q. Zhang, S. Y. Lee, T. Yasuda, C. Adachi, *Adv. Mater.* **2015**, *27*, 2096-2100.

- [14] Berberan-Santos, M. N.; Garcia, J. M., *J. Am. Chem. Soc.* **1996**, *118*, 9391-9394.
- [15] Endo, A.; Ogasawara, M.; Takahashi, A.; Yokoyama, D.; Kato, Y.; Adachi, C. *Adv. Mater.* **2009**, *21*, 4802-4806.
- [16] Endo, A.; Sato, K.; Yoshimura, K.; Kai, T.; Kawada, A.; Miyazaki, H.; Adachi, C. *Appl. Phys. Lett.* **2011**, *98*, 083302.
- [17] Zhang, Q. S.; Kuwabara, H.; Potscavage, W. J.; Huang, S. P.; Hatae, Y.; Shibata, T.; Adachi, C. *J. Am. Chem. Soc.* **2014**, *136*, 18070-18081.
- [18] Hirata, S.; Sakai, Y.; Masui, K.; Tanaka, H.; Lee, S. Y.; Nomura, H.; Nakamura, N.; Yasumatsu, M.; Nakanotani, H.; Zhang, Q. *Nat. Mater.* **2015**, *14*, 330-336.
- [19] Uoyama, H.; Goushi, K.; Shizu, K.; Nomura, H.; Adachi, C. *Nature* **2012**, *492*, 234-238.
- [20] Zhang, Q. S.; Li, B.; Huang, S. P.; Nomura, H.; Tanaka, H.; Adachi, C. *Nat. Photonics* **2014**, *8*, 326-332.
- [21] Kobayashi, T.; Niwa, A.; Takaki, K.; Haseyama, S.; Nagase, T.; Goushi, K.; Adachi, C. *Phys. Rev. Appl.* **2017**, *7*, 034002.
- [22] Y. Tao, K. Yuan, T. Chen, P. Xu, H. Li, R. Chen, C. Zheng, L. Zhang and W. Huang, *Adv. Mater.*, 2014, *26*, 7931–7958.
- [23] T. Hatakeyama, K. Shiren, K. Nakajima, S. Nomura, S. Nakatsuka, K. Kinoshita, J. Ni, Y. Ono and T. Ikuta, *Adv Mater*, 2016, **28**, 2777-2781.
- [24] Y. Kondo, K. Yoshiura, S. Kitera, H. Nishi, S. Oda, H. Gotoh, Y. Sasada, M. Yanai and T. Hatakeyama, *Nature Photonics*, 2019, **13**, 678-682.

Chapter 2. Structure–Property Correlation in Luminescent Indolo[3,2-*b*]indole (IDID) Derivatives : Unraveling the Mechanism of High Efficiency Thermally Activated Delayed Fluorescence (TADF)

2.1 Introduction

Thermally activated delayed fluorescence (TADF) is drawing tremendous attention in the field of organic light emitting diodes (OLEDs) because it can boost the internal quantum efficiency (IQE) of electroluminescence up to 100% through the reverse intersystem crossing (RISC).^[1,2] Theoretically, RISC occurs efficiently when energy difference (ΔE_{ST}) between the first excited singlet (S_1) and triplet (T_1) states is small enough.^[3-5] To realize efficient TADF, Adachi et al. embodied molecular design rules of using intramolecular charge transfer (ICT) mechanism with bulky electron donor and/or acceptor units which spatially separate the highest occupied molecular orbital (HOMO) and lowest unoccupied molecular orbital (LUMO) to ensure minimized ΔE_{ST} .^[6-10]

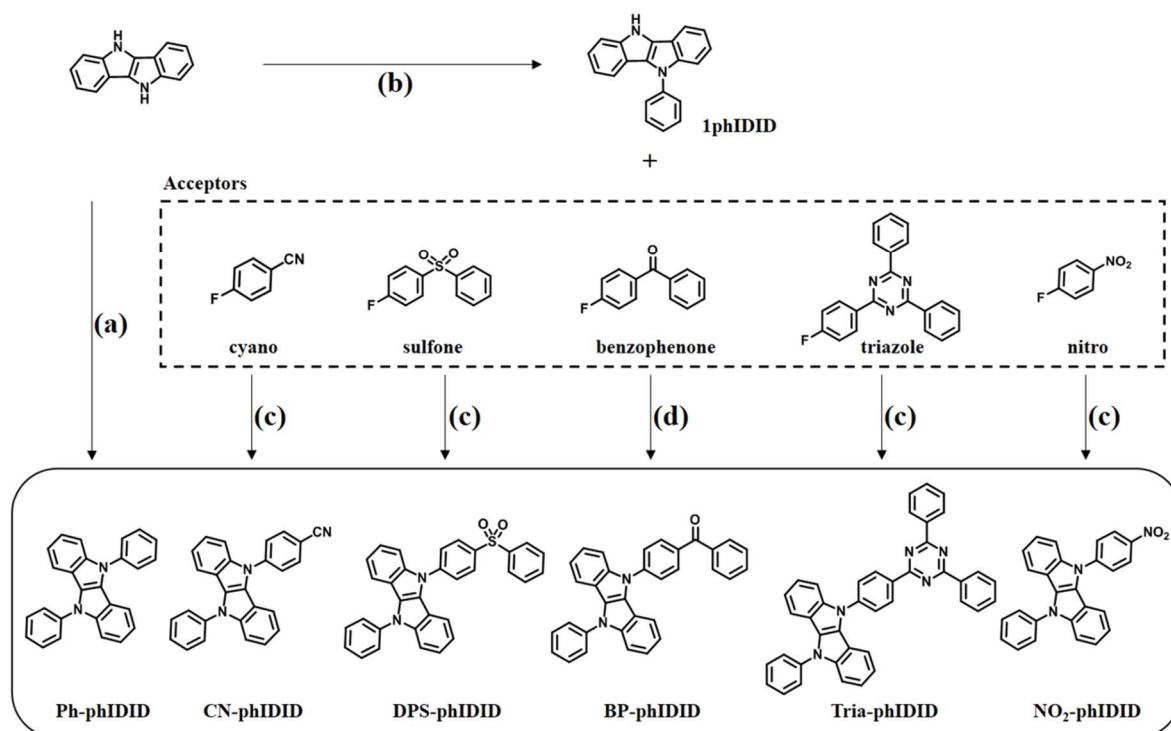
On the other hand, Dias *et al.* proposed that appropriate positioning and mixing of locally excited triplet state (3LE state) relative to the triplet charge transfer (3CT) state is also essential in increasing the RISC rate of TADF materials, because the spin-orbit coupling (SOC) is inefficient between singlet charge transfer (1CT) and 3CT states without mediation of 3LE states in principle.^[11-17] Even though many researchers have verified this proposal through diverse experimental and computational approaches, there has been still a lack of comprehensive

structure-property correlation work to date by systematically controlling the relevant energy levels for a homologous series of a given luminescent chromophore.^[18-21]

In this work, we have designed a series of indolo[3,2-b]indole (IDID) derivatives with different acceptor units to explore the structure-property correlation of TADF mechanism at one hand and to develop a novel TADF materials on the other hand. Recently, some papers reporting structure-property relationship and effects of acceptor strengths on TADF characteristics in terms of energy gap between S_1 and T_1 were published.^[22-25] But, in this paper, we focused on not only ΔE_{ST} but also the RISC mediated by 3LE state of IDID ($^3LE_{ID}$). Different from the conventional TADF donors, IDID molecule features low-lying 3LE state level ($T_1=2.60$ eV) owing to their extended conjugation along the planar rigid backbone (Figure S1). Therefore, it was expected that IDID derivatives should be versatile in engineering the energy level of 3CT state relative to the low-lying 3LE state ($^3LE_{ID}$) by employing different acceptor units, which had not been possible for the conventional high 3LE donor system. Moreover, IDID derivatives were previously reported as a promising organic semiconductor with excellent charge transport properties of ~ 1 cm²/Vs hole mobility.^[26-28] In this regard, it was considered that the IDID unit could make a new electron donor platform for highly efficient TADF molecules. Herein, we have synthesized a series of novel *N,N*-diphenyl IDID (Ph-phIDID) derivatives containing various electron accepting moieties including cyano, sulfone, benzophenone, triazole, and nitro groups. Systematically photophysical studies were carried out to examine the TADF mechanism and also the fabrication and characterization of OLED devices were made to explore their potential in high efficiency OLED application.

2.2 Experimental Methods

2.2.1 Synthesis of Materials



Scheme 2.1 Synthetic routes of IDID derivatives. a) copper powder, 18-Crown-6, potassium carbonate, iodobenzene, dichlorobenzene (DCB), 180 °C; b) copper iodide, potassium phosphate tribasic, iodobenzene, *trans*-1,2-cyclohexanediamine, 1,4-dioxane, 180 °C; c) NaH, anhydrous *N,N*-dimethylformamide (DMF), 55 °C; d) sodium *tert*-butoxide, anhydrous DMF, 110 °C.

All reagents were purchased from Sigma Aldrich, TCI, and Alfa Aesar. All experimental glassware was dried in an oven, and all experimental conditions were conducted in an argon or nitrogen environment. The target IDID material were synthesized through the following **scheme 2.1**.

Synthesis of Ph-phIDID

To a mixture of 5,10-dihydroindolo[3,2-b]indole ^[23] (1.80 g, 8.73 mmol), copper powder (1.67 g, 26.2 mmol), 18-crown-6 (0.46 g, 1.75 mmol) and potassium carbonate (6.03 g, 43.6 mmol) purged with Ar gas, iodobenzene (5.34 g, 26.2 mmol) and dichlorobenzene (DCB, 120 ml) was added. The mixture was gently refluxed at 180 °C with stirring under Ar atmosphere. After 24 h, the resulting product was poured into water (300 mL) and extracted with DCM. The combined organic phase was dried with MgSO₄ and concentrated under reduced pressure. The concentrated crude product was purified by column chromatography (EA/*n*-hexane 1 : 9 v/v) and the resulting solid was washed with methanol to afford Ph-phIDID as a white powder. (3.06 g, 97.8%). ¹H NMR (300 MHz, DMSO-*d*₆, δ): 7.80–7.71 (m, 4H), 7.62–7.52 (m, 2H), 7.46 (d, *J* = 7.8 Hz, 1H), 7.29 (t, *J* = 7.7 Hz, 1H), 7.15 (t, *J* = 7.5 Hz, 1H). ¹³C NMR (125 MHz, DMSO-*d*₆, δ): 140.18, 137.87, 130.03, 129.88, 127.08, 125.42, 123.10, 119.86, 117.98, 114.91, 110.85. HRMS *m/z*: calcd for C₂₆H₁₈N₂, 358.15; found, 358.1470. Elem. Anal. calcd for C₂₆H₁₈N₂: C 87.12, H 5.06, N 7.82; found: C 86.9, H 4.91, N 7.82.

Synthesis of 5-phenyl-5,10-dihydroindolo[3,2-b]indole (1phIDID)

To a mixture of 5,10-dihydroindolo[3,2-b]indole (5.31 g, 25.7 mmol), copper iodide (1.67 g, 26.2 mmol), potassium phosphate tribasic (5.46 g, 25.7 mmol) purged with Ar gas, iodobenzene (5.25 g, 25.7 mmol), *trans*-1,2-cyclohexanediamine (2.94 g, 25.7 mmol) and 1,4-dioxane (20 mL) were added. The mixture was gently refluxed at 180 °C with stirring under Ar atmosphere for 48 h. After cooling to room temperature, the reaction mixture was filtered and washed with chloroform. The filtrate was concentrated under reduced pressure. The concentrated crude product was purified by column chromatography (EA/CHCl₃/*n*-hexane

0.2:4:5 v/v) to afford 1phIDID as a pale yellow powder. (2.06 g, 28.6%). ¹H NMR (300 MHz, THF-*d*₈, δ): 10.42 (s, 1H), 7.80–7.70 (m, 3H), 7.61 (dd, *J* = 13.1, 5.1 Hz, 3H), 7.50–7.36 (m, 3H), 7.23–7.08 (m, 3H), 6.95 (t, *J* = 7.6 Hz, 1H).

Synthesis of CN-phIDID

A round-bottom flask equipped with a magnetic stirrer bar was baked under reduced pressure and Ar backfilled. Then, 5-phenyl-5,10-dihydroindolo[3,2-*b*]indole (0.200 g, 0.70 mmol), anhydrous DMF (15mL), and NaH (0.056 g, 1.4 mmol) were added to the baked flask. After 30 min at room temperature, 4-fluorobenzonitrile (0.102 g, 0.84 mmol) was added to the reaction mixture. After stirring 10 min, the reaction mixture was stirred at 55 °C under Ar atmosphere. After 10 h, the resulting product was poured into water (200 mL) and extracted with DCM. The combined organic phase was dried with MgSO₄ and concentrated under reduced pressure. The concentrated crude product was purified by column chromatography (EA/*n*-hexane 1:2 v/v) and the resulting solid was washed with methanol and recrystallized from chloroform/methanol to afford CN-phIDID as a pale yellow powder (0.175 g, 65.1%). ¹H NMR (300 MHz, DMSO-*d*₆, δ): 8.19 (d, *J* = 8.2 Hz, 2H), 8.03 (d, *J* = 8.3 Hz, 2H), 7.80–7.71 (m, 5H), 7.61–7.52 (m, 3H), 7.44 (d, *J* = 8.1 Hz, 2H), 7.32 (dd, *J* = 14.5, 7.2 Hz, 2H), 7.23–7.17 (m, 2H). ¹³C NMR (125 MHz, DMSO-*d*₆, δ): 141.92, 140.28, 139.81, 137.56, 134.30, 130.07, 127.37, 126.81, 125.63, 125.60, 124.87, 123.70, 123.30, 120.82, 120.11, 118.64, 118.25, 118.16, 115.74, 114.74, 111.07, 110.98, 108.74 HRMS *m/z*: calcd for C₂₆H₁₈N₂, 358.5; found, 358.1470. Elem. Anal. calcd for C₂₆H₁₈N₂: C 84.57, H 4.47, N 10.96; found: C 84.55, H 4.44, N 10.93.

Synthesis of DPS-phIDID

DPS-phIDID was synthesized similarly to CN-phIDID, using 5-phenyl-5,10-dihydroindolo[3,2-b]indole (0.200 g, 0.70 mmol), anhydrous DMF (15mL), NaH (0.056 g, 1.4 mmol) and 4-fluorophenyl phenylsulfone (0.167 g, 0.70 mmol). The product was obtained as a pale yellow powder (0.223 g, 63.2%). ¹H NMR (300 MHz, DMSO-*d*₆, δ): 8.29 (d, *J* = 8.6 Hz, 2H), 8.08 (dd, *J* = 11.9, 7.8 Hz, 4H), 7.79–7.69 (m, 8H), 7.59–7.50(m, 3H), 7.42 (d, *J* = 8.0 Hz, 1H), 7.30 (t, *J* = 7.8 Hz, 2H), 7.19 (t, *J* = 7.6 Hz, 2H). ¹³C NMR (125 MHz, DMSO-*d*₆, δ): 142.34, 141.05, 140.27, 139.82, 138.28, 137.53, 133.93, 130.07, 129.95, 129.54, 127.53, 127.39, 126.88, 125.66, 125.55, 124.77, 123.71, 123.28, 120.86, 120.14, 118.31, 118.13, 115.76, 114.71, 111.17, 110.95. HRMS *m/z*: calcd for C₃₂H₂₂N₂O₂S, 498.1402; found, 498.1393. Elem. Anal. calcd for C₃₂H₂₂N₂O₂S: C 77.09, H 4.45, N 5.62, S 6.43; found: C 77.02, H 4.45, N 5.66, S 6.47.

Synthesis of BP-phIDID

A round-bottom flask equipped with a magnetic stirrer bar was baked under reduced pressure and Ar backfilled. Then, 5-phenyl-5,10-dihydroindolo[3,2-b] indole (0.900 g, 3.17 mmol), anhydrous DMF (20 mL), sodium *tert*-butoxide (0.608 g, 6.33 mmol) and 4-fluorobenzophenone (0.760 g, 3.80 mmol) were added to the baked flask. The reaction mixture was stirred at 110 °C under Ar atmosphere. After 24 h, the resulting product was poured into water (200 mL) and extracted with DCM. The combined organic phase was dried with MgSO₄ and concentrated under reduced pressure. The concentrated crude product was purified by column chromatography (EA/*n*-hexane 1:2 v/v) and the resulting solid was washed with methanol and recrystallized from chloroform/methanol to afford BP-phIDID as a greenish yellow powder (1.084g, 74.1%). ¹H NMR (300 MHz, DMSO-*d*₆, δ): 8.12 (d, *J* = 8.5 Hz, 2H), 8.01 (d, *J* = 8.5 Hz, 2H), 7.90 (d, *J* = 7.0 Hz, 2H), 7.81–7.72 (m, 6H), 7.67–7.55 (m, 5H), 7.46

(d, $J = 8.2$ Hz, 1H), 7.33 (dd, $J = 7.9$ Hz, 2H), 7.20 (t, $J = 7.5$ Hz, 2H). ^{13}C NMR (125 MHz, DMSO- d_6 , δ): 194.76, 141.62, 140.29, 139.94, 137.65, 137.14, 134.59, 132.67, 131.77, 130.05, 129.62, 128.66, 127.29, 126.61, 125.60, 125.11, 124.74, 123.54, 123.24, 120.57, 120.07, 118.37, 118.13, 115.57, 114.85, 111.16, 110.91. HRMS m/z : calcd for $\text{C}_{33}\text{H}_{22}\text{N}_2\text{O}$, 462.17; found, 462.1725. Elem. Anal. calcd for $\text{C}_{33}\text{H}_{22}\text{N}_2\text{O}$: C 85.69, H 4.79, N 6.06, O 3.46; found: C 85.50, H 4.79, N 6.07.

Synthesis of Tria-phIDID

Tria-phIDID was synthesized similarly to CN-phIDID, using 5-phenyl-5,10-dihydroindolo[3,2-b]indole (1.000 g, 3.54 mmol), anhydrous DMF (20 mL), NaH (0.283 g, 7.08 mmol), and 2-(4-fluorophenyl)-4,6-diphenyl-1,3,5-triazine (1.391 g, 4.25 mmol). The product was obtained as a greenish yellow powder (yield = 1.47 g, 70.2%). ^1H NMR (500 MHz, THF- d_8 , δ): 9.23 (d, $J = 8.6$ Hz, 2H), 9.02–8.91 (m, 4H), 8.15 (d, $J = 8.6$ Hz, 2H), 7.91–7.86 (m, 3H), 7.79 (m, 3H), 7.76–7.67 (m, 7H), 7.60 (d, $J = 10.9$ Hz, 2H), 7.34 (d, $J = 19.0$ Hz, 2H), 7.21 (m, 2H). ^{13}C NMR (125 MHz, THF- d_8 , δ): 172.86, 137.37, 133.70, 131.59, 130.81, 129.99, 129.67, 127.99, 126.97, 126.25, 124.11, 123.84, 121.13, 120.76, 119.55, 119.47, 112.03, 111.85. HRMS m/z : calcd for $\text{C}_{41}\text{H}_{27}\text{N}_5$ 589.22; found, 589.2261. Elem. Anal. calcd for $\text{C}_{41}\text{H}_{27}\text{N}_5$: C 83.51, H 4.62, N 11.88; found: C 83.51, H 4.60, N 11.83.

Synthesis of NO₂-phIDID

NO₂-phIDID was synthesized similarly to CN-phIDID, using 5-phenyl-5,10-dihydroindolo[3,2-b]indole (0.150 g, 0.53 mmol), anhydrous DMF (10 mL), NaH (0.042 g, 1.06 mmol), and 1-fluoro-4-nitrobenzene (0.089 g, 0.63 mmol). The product was obtained as a

reddish powder (0.131 g, 61.6%). ^1H NMR (300 MHz, $\text{DMSO-}d_6$, δ): 8.57 (d, $J = 8.7$ Hz, 2H), 8.10 (d, $J = 8.9$ Hz, 2H), 7.81–7.72 (m, 5H), 7.60 (d, $J = 8.6$ Hz, 3H), 7.45 (d, $J = 8.3$ Hz, 1H), 7.38–7.30 (m, 2H), 7.25–7.18 (m, 2H). ^{13}C NMR (125 MHz, $\text{DMSO-}d_6$, δ): 144.88, 143.63, 140.35, 139.87, 137.50, 130.10, 127.47, 127.12, 125.71, 125.70, 125.31, 124.77, 123.89, 123.36, 121.11, 120.19, 118.41, 118.23, 116.01, 114.75, 111.23, 111.02. HRMS m/z : calcd for $\text{C}_{26}\text{H}_{17}\text{N}_3\text{O}_2$, 403.13; found, 403.1317. Elem. Anal. calcd for $\text{C}_{26}\text{H}_{17}\text{N}_3\text{O}_2$: C 77.41, H 4.25, N 10.42; found: C 77.41, H 4.25, N 10.38.

2.2.2 Characterization

Chemical structures were identified by ^1H NMR (Bruker, ADVANCE-300 and ADVANCE-500), ^{13}C NMR (Bruker, Advance-500), high-resolution mass spectrometry (AB SCIEX, Q-TOF 5600), and elemental analysis (Thermo Fisher Scientific, Flash 1112). UV-vis absorption spectra were recorded using a SHIMADZU UV-1650PC. Steady-state photoluminescence (PL) spectra were obtained with a PTI QuantaMaster 40 spectrofluorometer at room temperature and absolute PL quantum yields (PLQY) were recorded using a 3.2 inch integrating sphere. Low temperature photoluminescence spectra were measured using a Jasco FP-6500 at 77 K. Photoluminescence decay traces were obtained through the time correlated single photon counting (TCSPC) techniques by using a PicoQuant, FluoTime 250 instrument (PicoQuant, Germany). A 377 nm pulsed laser was used as an excitation source and temperature dependent studies were made with a cryostat (Oxford Instruments, Optistat DN). Data analyses were performed using exponential fitting models by FluoFit software. Cyclic voltammetry measurements were performed using a 273A (Princeton Applied Research). Each oxidation potential was calibrated using ferrocene as a reference. LUMO levels were evaluated from the HOMO level and the optical band gap which was obtained from the edge of the absorption

spectra. DFT calculations were performed in the gas phase using Gaussian 09 quantum-chemical package. The geometry optimization for ground state of IDID derivatives was carried out using B3LYP functionals with 6-31G (d, p) basis set. TD-DFT calculations were performed using same functional and basis sets that were used.

2.2.3 Device fabrication and Measurement.

The patterned ITO substrates were rinsed with acetone and isopropyl alcohol using sonication for 15 min, followed by 15 min UV-ozone-treatment. Organic layers, MoO₃ and Al were thermally evaporated at a deposition rate of 0.6–1 Å s⁻¹ for organic layers, 0.2 Å s⁻¹ for MoO₃, and 4–5 Å s⁻¹ for Al electrode. The current–voltage–luminance (I–V–L) characteristics of the devices were measured with a Keithley-236 source-measure unit, a Keithley-2000 multimeter unit, and a calibrated Si photodiode (Hamamatsu S5227-1010BQ). The luminance and efficiencies were calculated from the photocurrent measurement data obtained with the Si photodiode. The electroluminescence spectra were obtained by using a spectroradiometer (CS-2000).

2.3 Results and Discussion

2.3.1 Material Design

In designing IDID derivatives for possible TADF application, following three criteria were considered: 1) ICT structure for separating HOMO and LUMO, 2) introducing phenyl linker to address the trade-off between ΔE_{ST} and oscillation strength, 3) acceptor variation for tuning ICT strength. In this regard, Ph-phIDID was designed as a novel structural scaffold to which various electron acceptors including cyano (CN-phIDID), sulfone (DPS-phIDID), benzophenone (BP-phIDID), triazole (Tria-phIDID) and nitro (NO₂-phIDID) groups were systematically introduced in the order of increasing acceptor strength.

2.3.2 Density Functional Theory Calculations

The optimized geometry and electronic properties of IDID derivatives were calculated by density functional theory (DFT) and time-dependent DFT (TD-DFT) using the B3LYP functional and the 6-31G** basis set (**Figure 2.1**). In the optimized ground state geometry, all the IDID derivatives showed twisted conformation with dihedral angle of around 40° between the IDID core and the acceptor substituted phenyl ring. As was expected, HOMO is located on IDID core and *N*-phenyl units, while LUMO is extended from acceptor moieties to pyrrole ring of IDID. Thus, not only the spatial separation of HOMO and LUMO but also the modest orbital overlap could be achieved at the same time successfully addressing the trade-off between ΔE_{ST} and oscillation strength. With increasing acceptor strength, it was calculated that the bandgap (4.06 ~ 2.77 eV) and ΔE_{ST} (0.99 ~ 0.22 eV) were systematically decreased with increasing acceptor strength as shown in **Figure 2.1**.

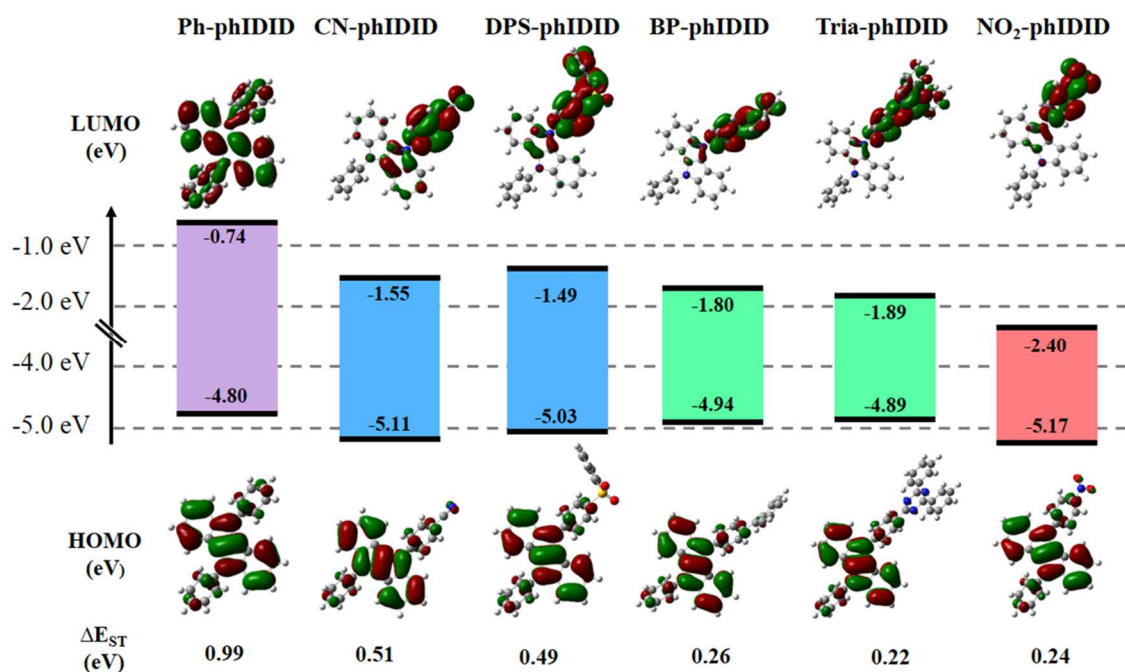


Figure 2.1 HOMO and LUMO distribution and energy difference (ΔE_{ST}) between the first singlet (S_1) and triplet (T_1) states of IDID derivatives.

2.2.3 Photophysical Properties

Photophysical properties of IDID derivatives were evaluated by UV-visible absorption (UV-vis) and photoluminescence emission (PL) spectra. (**Figure 2.2** and **Table 2.1**). It is shown in **Figure 2.2** that Ph-phIDID has the lowest absorption band by the π - π^* transition at 363 nm and the characteristic violet emission with obvious vibrational structure. On the other hand, all the other IDID derivatives with different acceptor groups showed gradually red-shifted absorption band with increasing acceptor strength. Moreover, their PL spectra exhibited a broad and structureless 1CT emission which were also gradually red shifted from blue (460 nm) to red (660 nm) with increasing acceptor strength. Therefore, it was successfully demonstrated that IDID is a novel and viable platform of ICT chromophore covering the entire visible range. While PL quantum yields (PLQYs, Φ_{PL}) of these IDID derivatives are moderate to high as

shown in **Table 2.1**, those are always higher in film than in solution presumably because the solid matrix suppresses the molecular vibrational motions. In the film matrix, the highest PLQY was 69.8% for Tria-IDID and other IDID compounds also exhibited over 40% except for NO₂-phIDID ($\Phi_{\text{PL}}=2\%$). The reason why NO₂-phIDID holds lower Φ_{PL} is attributed to the energy gap law and strong accepting properties of nitro group. ^[29,30]

Fluorescence lifetime measurement was carried out to verify different emission components of the IDID derivatives using Time Correlated Single Photon Counting (TCSPC). Among five ICT emitters CN-phIDID, DPS-phIDID and NO₂-phIDID exhibited just a single component of fluorescence lifetime shorter than 7.3 ns much like the case of Ph-phIDID (**Table 2.1** and **Figure 2.3**). On the other hand, decay profiles of BP-phIDID and Tria-phIDID consisted not only the prompt fluorescence but also the delayed fluorescence. Moreover, the latter was unambiguously verified as TADF because the proportion of the delayed components were significantly reduced with decreasing temperature (**Figure 2.2c** and **Figure 2.2d**). It was thus clearly demonstrated that the Ph-phIDID unit act as TADF platform but only when they are substituted with appropriate strength acceptors, which should give a valuable clue to the mechanism of the TADF process.

To explore the emission mechanism of this series of IDID derivatives, low temperature PL was measured in toluene at 77 K (**Figure 2.4a**). Interestingly, ICT type emitters from CN-phIDID to Tria-phIDID regardless of acceptor moieties exhibited identical phosphorescent spectra with well-defined vibrational structuring, which coincided with that of Ph-phIDID as well. Therefore, it was best speculated that the T₁ state of these compounds are characterized by the locally excited triplet state of IDID (³LE_{ID}) which is stabilized based on the extended π electron delocalization in the planer IDID skeleton. Because IDID derivatives hold such a constant and low-lying ³LE state, it constitutes the T₁ with high-lying ³CT state, till the ICT strength becomes strong enough to locate ³CT below the ³LE (sole case of NO₂-phIDID, *vide*

infra). Therefore, we have a systematic control between the pinned ^3LE state and varying CT states (^1CT & ^3CT) through acceptor tuning as depicted in **Scheme 2.2**.

CN-phIDID and DPS-phIDID, which employs relatively weak acceptors, have so high S_1 level (^1CT) that RISC from T_1 to S_1 is ineffective due to the large ΔE_{ST} (**Scheme 2.2, caseI**). On the other hand, BP-phIDID and Tria-phIDID with enhanced ICT strength showed that the CT (^1CT & ^3CT) states are located close to the fixed ^3LE to facilitate the mixing of the $^3\text{CT}/^3\text{LE}$ states. This situation is actually evidenced by the overlapped fluorescence and phosphorescence spectra as shown in the **Figure 2.4b** and **Figure 2.4c**. In this case, triplet up-conversion occurs efficiently owing to small ΔE_{ST} mediated by ^3LE state (**Scheme 2.2, caseII**).

In contrast, NO_2 -phIDID does not show any delayed fluorescence component despite its small enough ΔE_{ST} . NO_2 -phIDID showed broad and structureless CT spectrum in the low temperature PL spectrum. Thus, it is rationalized that the T_1 state is changed from $^3\text{LE}_{\text{ID}}$ state to ^3CT in accordance with the more stabilized CT states (^1CT & ^3CT). As a result, the CT states is separated far away from the fixed $^3\text{LE}_{\text{ID}}$ state and thus the spin orbit coupling would be forbidden between ^1CT and ^3CT state without the aid of ^3LE state (**Scheme 2.2, case III**).^[31] In addition, NO_2 -phIDID have considerably large non-radiative rate constant (see **Table 2.1**), implying that the excited molecules quickly decay to the ground state through the non-radiative pathways. As a result, RISC of the triplet exciton could not occur efficiently and consequently NO_2 -phIDID exhibits no TADF emission.

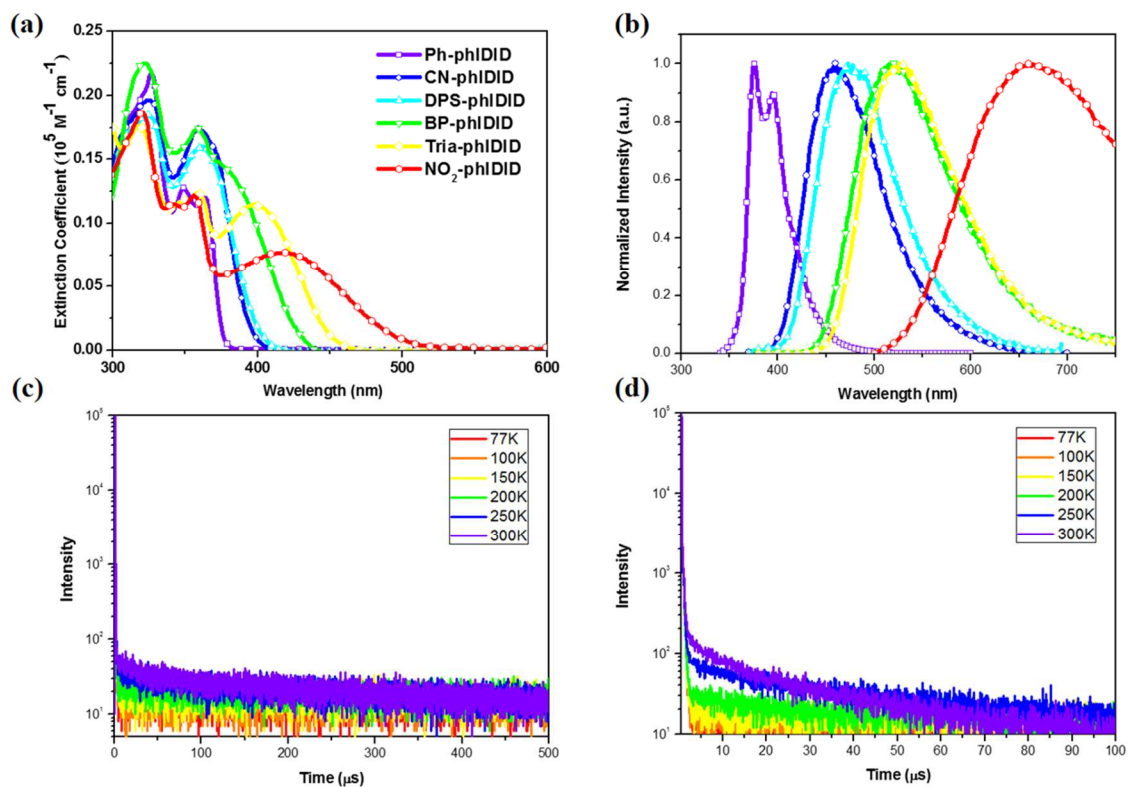
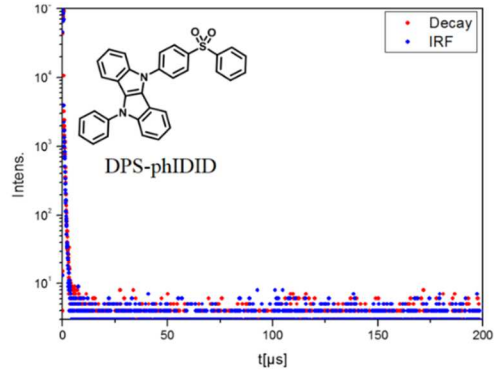
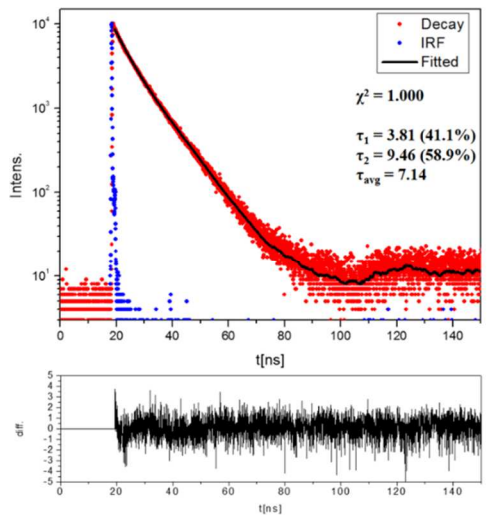
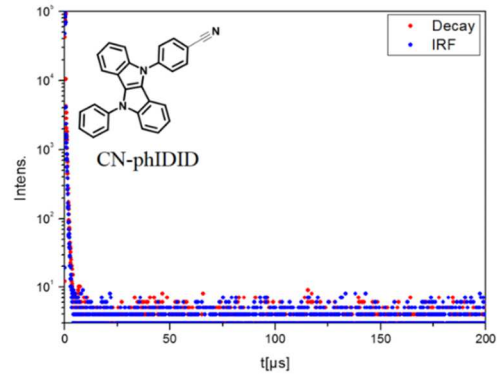
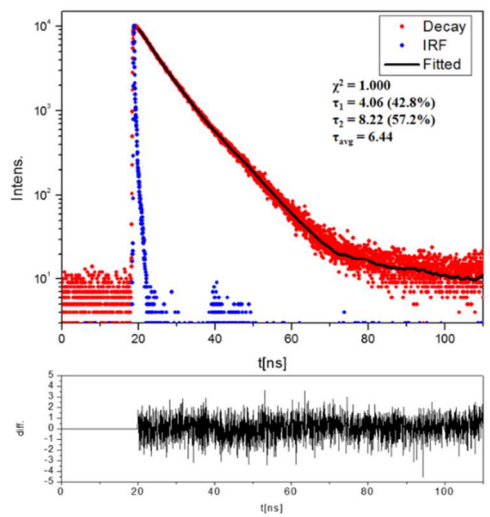
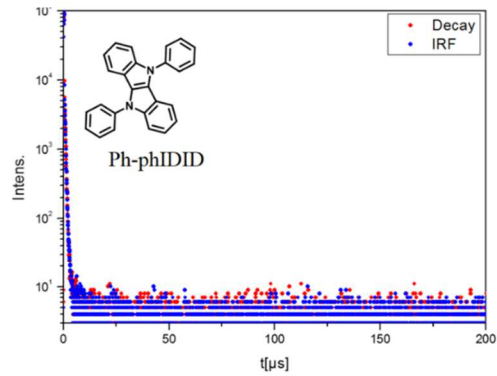
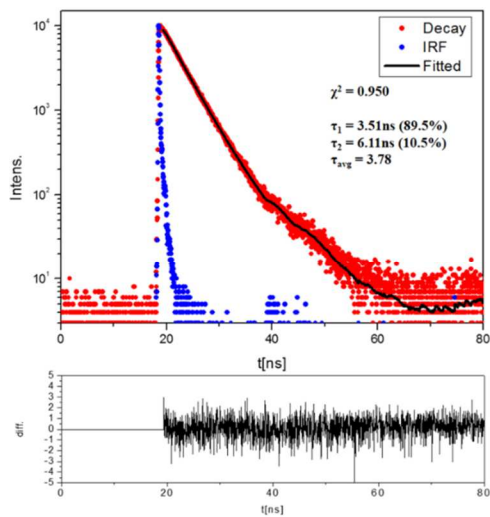


Figure 2.2 Photophysical properties of the IDID molecules. (a) UV-vis absorption spectra (toluene, $c=1 \times 10^{-5} \text{ M}$) (b) normalized photoluminescence spectra (in toluene, $c=1 \times 10^{-5} \text{ M}$) (c) Temperature-dependent PL decay spectra of 8 wt% BP-phIDID in CBP film and (d) 8 wt% Tria-phIDID in CBP film.



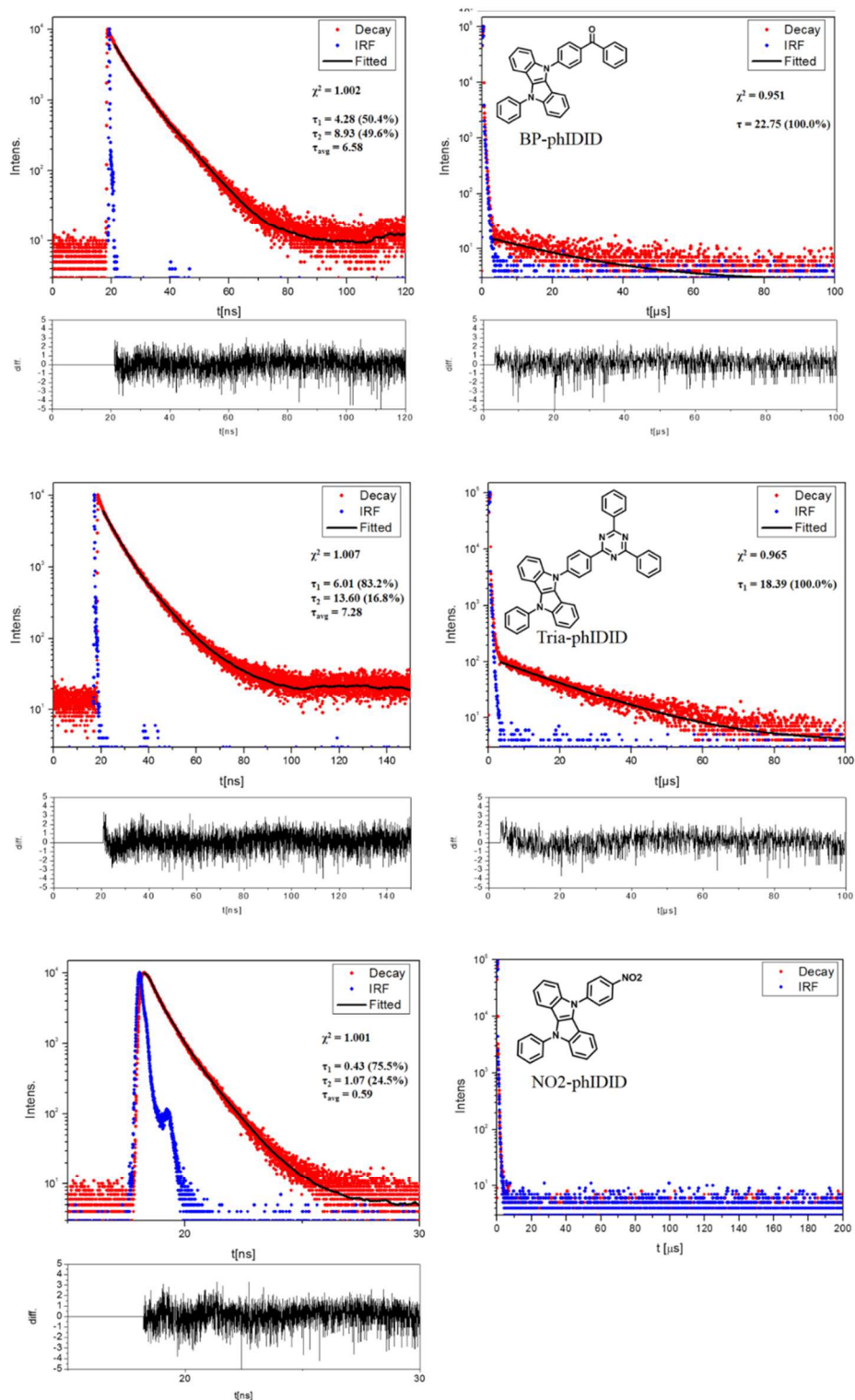


Figure 2.3 Photoluminescence decay traces of IDID derivatives of 6 wt% in a PMMA film using pulsed laser excitation at 377 nm. Red dots are lifetime decay profiles, blue dots are the instrumental response functions (IRF) and black solid lines are fitted lines; lower black lines are the residuals.

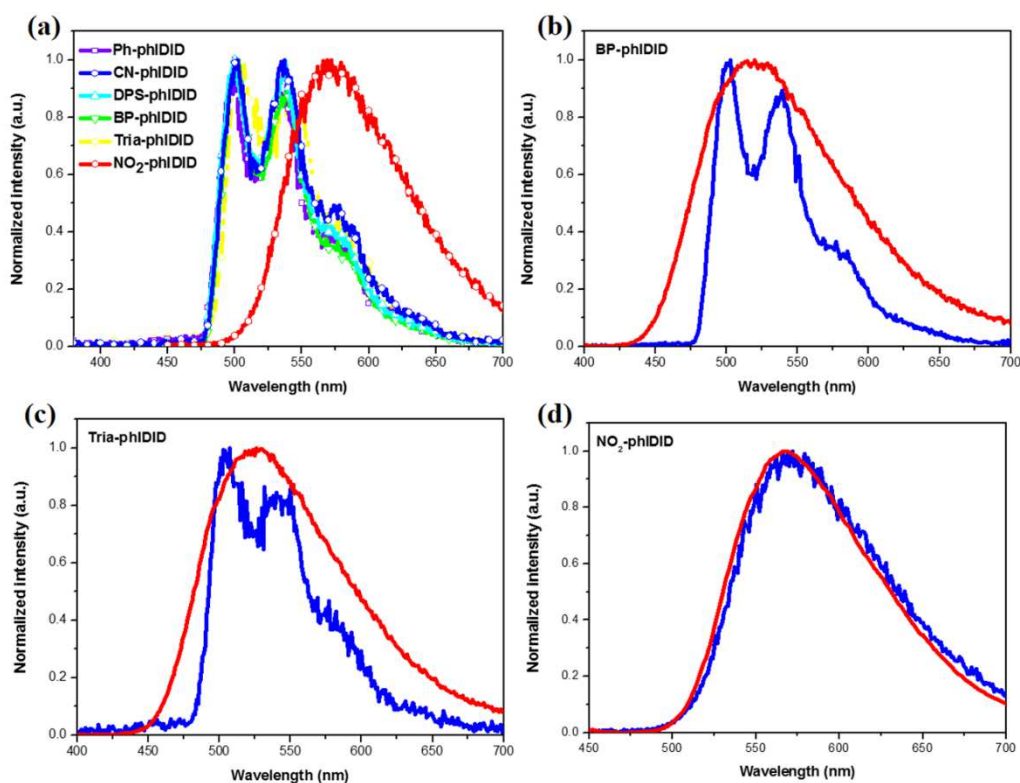


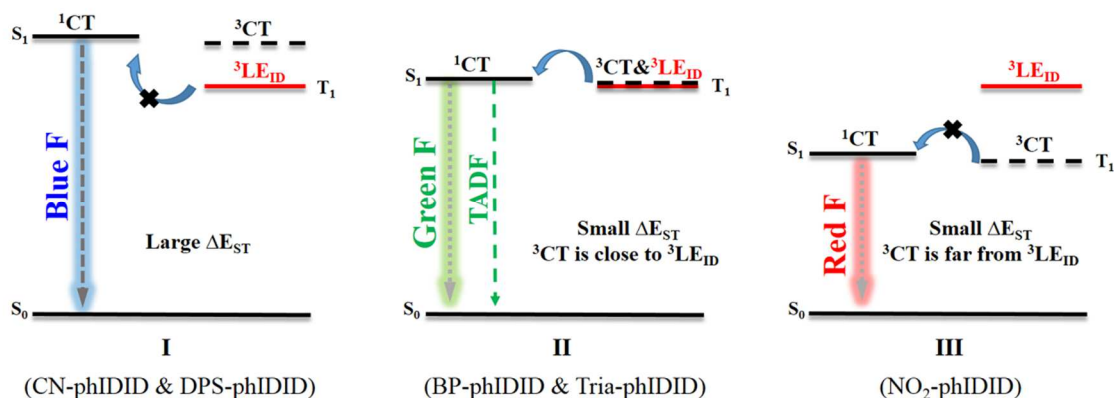
Figure 2.4 a) The phosphorescence spectra of IDID derivatives in toluene solution at 77 K. b) Fluorescence and phosphorescence spectra in toluene solution of BP-phIDID, c) Tria-phIDID, d) NO₂-phIDID.

Table 2.1 Photophysical and Electrical Properties of the IDID derivatives.

compound	$\lambda_{\text{abs,max}}^a$ [nm]	$\lambda_{\text{PL,max}}^a$ [nm]	$\Phi_{\text{PL,sol}}^b$ [%]	$\Phi_{\text{PL,film}}^b$ (PMMA/CBP) [%]	$^1\text{CT}^c$ [eV]	$^3\text{LE}^d$ [eV]	ΔE_{ST}^e [eV]	τ_p^f [ns]	τ_d^f [μs]	k_f^g [$\times 10^8 \text{ s}^{-1}$]	k_{nr}^h [$\times 10^8 \text{ s}^{-1}$]	HOMO ⁱ [eV]	LUMO ⁱ [eV]
Ph-phIDID	363	376	40.4	44.2/30.0	3.51	2.60	0.91	3.7	-	1.19	1.51	-5.12	-1.82
CN-phIDID	359	460	14.3	45.1/40.2	3.10	2.60	0.50	6.4	-	0.70	0.86	-5.12	-1.96
DPS-phIDID	360	473	19.5	53.6/46.4	3.03	2.60	0.43	7.1	-	0.75	0.65	-5.22	-2.12
BP-phIDID	358	520	22.6	54.4/56.9	2.80	2.60	0.20	6.6	22.8	0.82	0.69	-5.19	-2.30

Tria-phIDID	357,398	526	44.5	59.3/69.8	2.72	2.60	0.12	7.3	18.4	0.81	0.56	-5.14	-2.39
NO₂-phIDID	356, 418	660	2.0	3.1/2.0	2.35	-	0.03	0.6	-	0.51	16.15	-5.23	-2.80

^a UV-vis absorption and PL spectra measured in 1×10^{-5} M toluene solution. ^b Absolute PL quantum yields recorded in degassed 1×10^{-5} M toluene solution and 6 wt% PMMA/ 8 wt% CBP doping films using an integrating sphere. ^c ^1CT energy level estimated from onsets of the fluorescence spectra in 1×10^{-5} M toluene solution. ^d ^3LE energy level estimated from onsets of the phosphorescence spectra in 1×10^{-5} M toluene solution. ^e Energy gap between S_1 and T_1 estimated from the fluorescence and the phosphorescence spectra in 1×10^{-5} M toluene solution. ^f Lifetimes calculated from the prompt and delayed fluorescence decay in PMMA 6 wt% doping film. ^g Radiative decay rate $k_r = \Phi_{\text{PL}}/\tau$. ^h Nonradiative decay rate $k_{\text{nr}} = \tau^{-1} - k_r$. ⁱ HOMO level was determined by cyclic voltammetry in 5×10^{-3} M methylene chloride solution using ferrocene as a reference. ^j LUMO levels were evaluated with the HOMO level and the optical band gap obtained from the edge of the absorption spectra.



Scheme 2.2. Schematic illustration of emission mechanism of IDID derivatives.

2.3.4 Electrochemical properties

In order to evaluate the energy level of these compounds, cyclic voltammetry (CV) was carried out in methylene chloride solution using ferrocene as a reference (**Figure 2.5**). Ph-phIDID, CN-phIDID, DPS-phIDID, BP-phIDID, Tria-phIDID and NO₂-phIDID exhibited HOMO levels of -5.12, -5.12, -5.22, -5.19, -5.14 and -5.23 eV, respectively. The LUMO level of a material was obtained by adding the optical bandgap to the HOMO level, and were calculated as -1.82, -1.96, -2.12, -2.30, -2.39 and -2.80 eV, respectively. The band gaps are 3.3, 3.16, 3.10, 2.89, 2.75 and 2.43 eV, respectively.

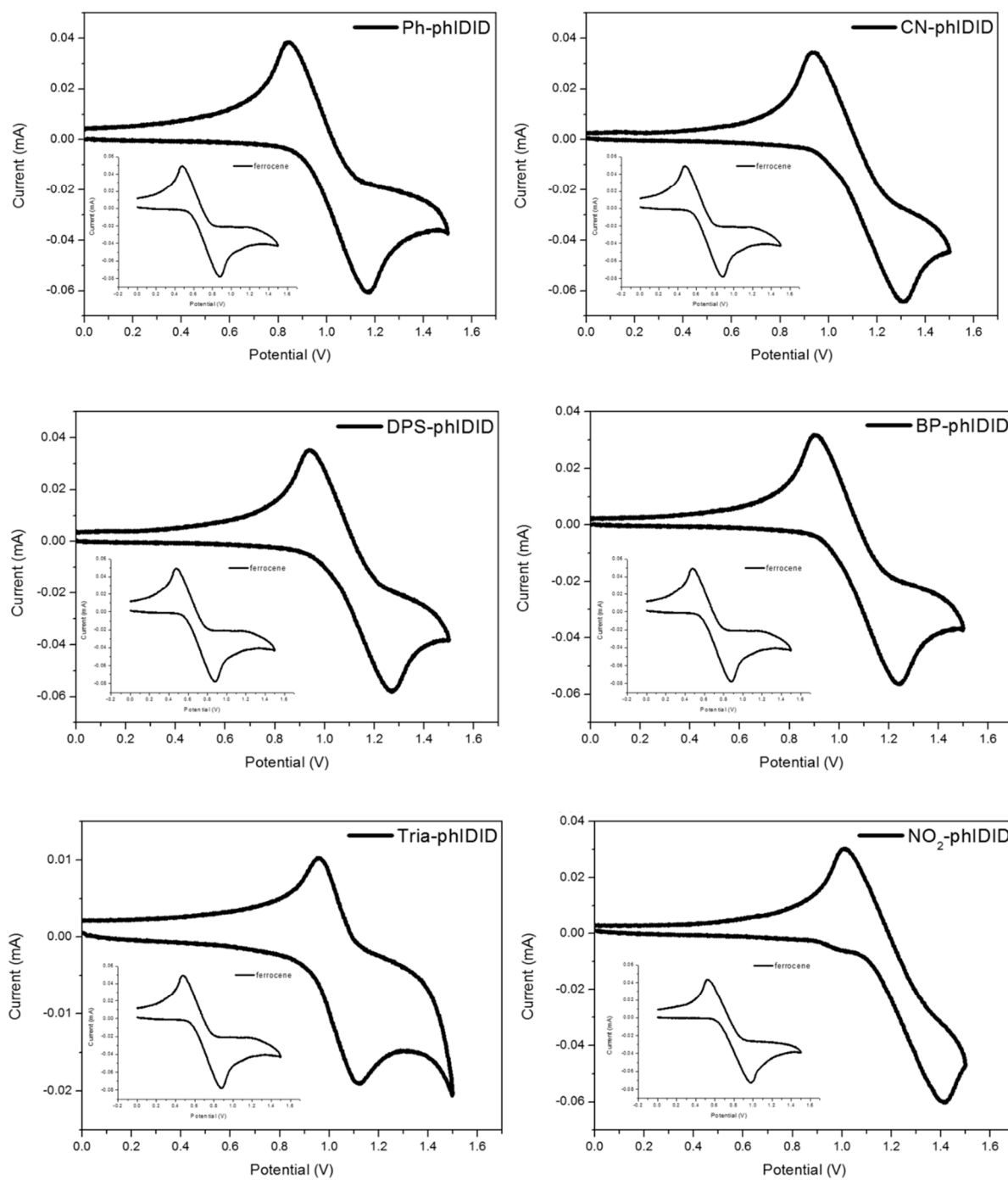


Figure 2.5 Cyclic voltammetry (CV) of IDID derivatives. Solution samples were prepared 5 x 10⁻³ M solution in methylene chloride (Inset: CV of ferrocene).

2.3.5 OLED Performances

To examine the possible OLEDs application of novel IDID based TADF emitters, BP-phIDID and Tria-phIDID were selected due to their high PLQY and TADF characteristics. Multi-layered OLED devices were fabricated comprising glass substrate/ITO (indium thin oxide) anode/MoO₃ (10 nm)/TAPC (50 nm)/EML (20 nm)/TmPyPb (40 nm)/LiF (1 nm)/Al (100 nm). ITO, MoO₃, LiF, and Al were used as the anode, hole-injection layer, electron-injection layer and the cathode, respectively. Di-[4-(*N,N*-ditolyl-amino)-phenyl]-cyclohexane (TAPC) and 1,3,5-tri(*m*-pyrid-3-yl-phenyl) benzene (TmPyPB) were used as hole-transport layer (HTL) and electron-transport layer (ETL), respectively. Emitting layers (EML) incorporating 8%-IDID derivatives in 4,4'-bis(carbazol-9-yl) biphenyl (CBP) host were vacuum evaporated. The current density–voltage–luminance (*J*–*V*–*L*) curve and the EQE versus luminance characteristics of the devices are shown in **Figure 2.6**, from which the detailed device parameters are extracted and summarized in **Table 2.2**. The OLED devices of Tria-phIDID and BP-phIDID were shown to turn on at 3.4 and 3.7 V to give green emission (EL_{max} at 504 and 497 nm), with CIE coordinates of (0.28,0.49) and (0.25,0.43), respectively. As shown in **Table 2.2**, the maximum luminance efficiency, power efficiency, and external quantum efficiency values for Tria-phIDID were 56.41 cd A⁻¹, 50.63 lm W⁻¹ and 20.8%, respectively and those for BP-phIDID were 34.16 cd A⁻¹, 28.34 lm W⁻¹, 13.9%, respectively. It indicates that triplet excitons are effectively utilized through the TADF mechanism in the device of Tria-phIDID and BP-phIDID. But, EQE values of Tria-phIDID and BP-phIDID devices decreased to 10.7% and 6.1% at a luminance of 100 cd m⁻². It is likely due to that triplet excitons were quenched by triplet–triplet annihilation (TTA) and singlet–triplet annihilation (STA) at high current density.^[32,33]

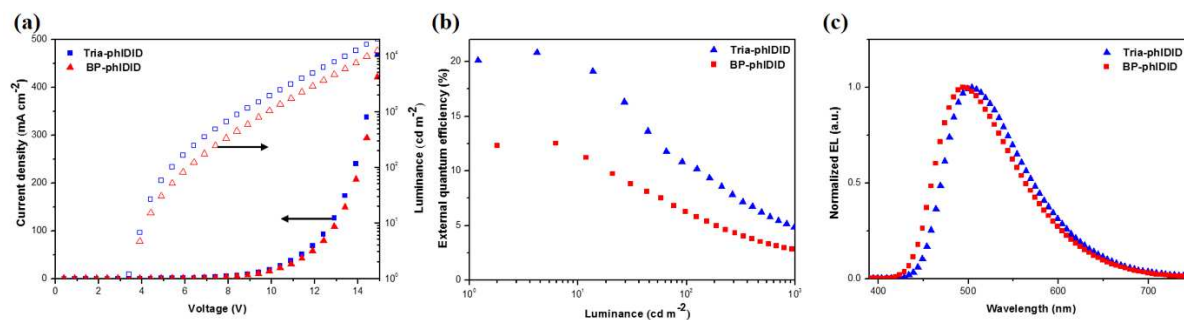


Figure 2.6 Device performance of IDID TADF materials. (a) J - V - L characteristics, (b) external quantum efficiency, (c) EL spectra for OLEDs

Table 2.2 Device performances of the IDID based TADF-OLEDs.

compound	V_{on}^a [V]	λ_{max}^b [nm]	CIE ^c (x,y)	CE_{max}^d [cd A ⁻¹]	PE_{max}^e [lm W ⁻¹]	EQE_{max}^f [%]	At 100 cd m ⁻²		
							CE [cd A ⁻¹]	PE [lm W ⁻¹]	EQE [%]
BP-phIDID	3.7	497	(0.25,0.43)	34.2	28.3	13.9	15.0	7.6	6.1
Tria-phIDID	3.4	504	(0.28,0.49)	56.4	50.6	20.8	28.9	16.8	10.7

^a turn-on voltage at 1 cd m⁻². ^b EL maximum wavelength. ^c measured at 0.1 mA cm⁻². ^d current efficiency. ^e power efficiency. ^f external quantum efficiency.

2.4 Conclusion

A new series of IDID derivatives with systematically controlled singlet (^1CT) and triplet (^3CT , ^3LE) energy levels were designed and synthesized to examine the fundamental mechanism of delayed fluorescence and also to develop a high efficiency TADF material. While the energy level of ^3LE state was virtually pinned at 2.60 eV, those of ^1CT and ^3CT were effectively varied with increasing acceptor strength of the IDID derivatives. It was clearly demonstrated in this work that TADF occurs only when the requirements of both the small ΔE_{ST} and $^3\text{LE}/^3\text{CT}$ mixing are satisfied. Particularly, Tria-phIDID and BP-phIDID, with medium and appropriate $^1\text{CT}/^3\text{CT}$ level, exhibited high photoluminescence and delayed fluorescence by facilitated RISC based on the appropriate positioning and mixing of $\text{CT}\&^3\text{LE}_{\text{ID}}$ state. The OLEDs based on these IDID TADF molecules offered high maximum EQEs of 20.8% and 13.9%, respectively.

2.5. References

- [1] Kaji, H.; Suzuki, H.; Fukushima, T.; Shizu, K.; Suzuki, K.; Kubo, S.; Komino, T.; Oiwa, H.; Suzuki, F.; Wakamiya, A.; Murata, Y.; Adachi, C, *Nat. Commun.***2015**, *6*, 8476.
- [2] Zhang, Q. S.; Tsang, D.; Kuwabara, H.; Hatae, Y.; Li, B.; Takahashi, T.; Lee, S. Y.; Yasuda, T.; Adachi, C, *Adv. Mater.***2015**, *27*, 2096-2100.
- [3] Berberan-Santos, M. N.; Garcia, J. M, *J. Am. Chem. Soc.* **1996**, *118*, 9391-9394.
- [4] Endo, A.; Ogasawara, M.; Takahashi, A.; Yokoyama, D.; Kato, Y.; Adachi, C, *Adv. Mater.***2009**, *21*, 4802-4806.
- [5] Endo, A.; Sato, K.; Yoshimura, K.; Kai, T.; Kawada, A.; Miyazaki, H.; Adachi, C, *Appl. Phys. Lett.* **2011**, *98*, 083302.
- [6] Zhang, Q. S.; Kuwabara, H.; Potscavage, W. J.; Huang, S. P.; Hatae, Y.; Shibata, T.; Adachi, C, *J. Am. Chem. Soc.* **2014**, *136*, 18070-18081.
- [7] Hirata, S.; Sakai, Y.; Masui, K.; Tanaka, H.; Lee, S. Y.; Nomura, H.; Nakamura, N.; Yasumatsu, M.; Nakanotani, H.; Zhang, Q, *Nat. Mater.* **2015**, *14*, 330-336.
- [8] Uoyama, H.; Goushi, K.; Shizu, K.; Nomura, H.; Adachi, C, *Nature* **2012**, *492*, 234-238.
- [9] Zhang, Q. S.; Li, B.; Huang, S. P.; Nomura, H.; Tanaka, H.; Adachi, C, *Nat. Photonics* **2014**, *8*, 326-332.
- [10] Kobayashi, T.; Niwa, A.; Takaki, K.; Haseyama, S.; Nagase, T.; Goushi, K.; Adachi, C, *Phys. Rev. Appl.* **2017**, *7*, 034002.
- [11] Dias, F. B.; Bourdakos, K. N.; Jankus, V.; Moss, K. C.; Kamtekar, K. T.; Bhalla, V.; Santos, J.; Bryce, M. R.; Monkman, *Adv. Mater.***2013**, *25*, 3707-3714.
- [12] Dias, F. B.; Santos, J.; Graves, D. R.; Data, P.; Nobuyasu, R. S.; Fox, M. A.; Batsanov, A. S.; Palmeira, T.; Berberan-Santos, M. N.; Bryce, M. R.; Monkman, *Adv. Sci.* **2016**, *3*, 160080.

- [13] Nobuyasu, R. S.; Ren, Z. J.; Griffiths, G. C.; Batsanov, A. S.; Data, P.; Yan, S. K.; Monkman, A. P.; Bryce, M. R.; Dias, F. B, *Adv. Opt. Mater.* **2016**, *4*, 653-653.
- [14] Santos, P. L.; Ward, J. S.; Data, P.; Batsanov, A. S.; Bryce, M. R.; Dias, F. B.; Monkman, A. P, *J. Mater. Chem. C* **2016**, *4*, 3815-3824.
- [15] Gibson, J.; Monkman, A. P.; Penfold, T. J, *Chemphyschem* **2016**, *17*, 2956-2961.
- [16] Dias, F. B.; Penfold, T. J.; Monkman, A. P, *Methods Appl. Fluoresc.* **2017**, *5*, 012001.
- [17] Etherington, M. K.; Gibson, J.; Higginbotham, H. F.; Penfold, T. J.; Monkman, A. P, *Nat. Commun.* **2016**, *7*, 13680.
- [18] Data, P.; Pander, P.; Okazaki, M.; Takeda, Y.; Minakata, S.; Monkman, A. P, *Angew. Chem., Int. Ed.* **2016**, *55*, 5739-5744.
- [19] Samanta, P. K.; Kim, D.; Coropceanu, V.; Brédas, J.-L, *J. Am. Chem. Soc.* **2017**, *139*, 4042-4051.
- [20] Olivier, Y.; Moral, M.; Muccioli, L.; Sancho-García, J.-C, *J. Mater. Chem. C* **2017**, *5*, 5718-5729.
- [21] Hosokai, T.; Matsuzaki, H.; Nakanotani, H.; Tokumaru, K.; Tsutsui, T.; Furube, A.; Nasu, K.; Nomura, H.; Yahiro, M.; Adachi, C, *Sci. Adv.* **2017**, *3*, e1603282.
- [22] Lee, J.; Shizu, K.; Tanaka, H.; Nakanotani, H.; Yasuda, T.; Kaji, H.; Adachi, C, *J. Mater. Chem. C* **2015**, *3*, 2175-2181.
- [23] Cai, X. Y.; Gao, B.; Li, X. L.; Cao, Y.; Su, S. J, *Adv. Funct. Mater.* **2016**, *26*, 8042-8052.
- [24] Pan, K. C.; Li, S. W.; Ho, Y. Y.; Shiu, Y. J.; Tsai, W. L.; Jiao, M.; Lee, W. K.; Wu, C. C.; Chung, C. L.; Chatterjee, T.; Li, Y. S.; Wong, K. T.; Hu, H. C.; Chen, C. C.; Lee, M. T, *Adv. Funct. Mater.* **2016**, *26*, 7560-7571.
- [25] Sun, J. W.; Baek, J. Y.; Kim, K. H.; Huh, J. S.; Kwon, S. K.; Kim, Y. H.; Kim, J. J, *J. Mater. Chem. C* **2017**, *5*, 1027-1032.

- [26] Cho, I.; Park, S. K.; Kang, B.; Chung, J. W.; Kim, J. H.; Cho, K.; Park, S. Y, *Adv. Funct. Mater.* **2016**, *26*, 2966-2973.
- [27] Cho, I.; Jeon, N. J.; Kwon, O. K.; Kim, D. W.; Jung, E. H.; Noh, J. H.; Seo, J.; Seok, S. I.; Park, S. Y, *Chem. Sci.* **2017**, *8*, 734-741.
- [28] Cho, I.; Park, S. K.; Kang, B.; Chung, J. W.; Kim, J. H.; Yoon, W. S.; Cho, K.; Park, S. Y, *J. Mater. Chem. C* **2016**, *4*, 9460-9468.
- [29] Caspar, J. V.; Kober, E. M.; Sullivan, B. P.; Meyer, T. J, *J. Am. Chem. Soc.* **1982**, *104*, 630-632.
- [30] Ueno, T.; Urano, Y.; Kojima, H.; Nagano, T, *J. Am. Chem. Soc.* **2006**, *128*, 10640-10641.
- [31] Lim, B. T.; Okajima, S.; Chandra, A.; Lim, E, *Chem. Phys. Lett.* **1981**, *79*, 22-27.
- [32] Masui, K.; Nakanotani, H.; Adachi, C, *Org. Electron.* **2013**, *14*, 2721-2726.
- [33] Zhang, Y.; Forrest, S. R, *Phys. Rev. Lett.* **2012**, *108*, 267404.

Chapter 3. Systematic Substituent Control in Blue Thermally-Activated Delayed Fluorescence (TADF) Emitters: Unraveling the Role of Direct Intersystem Crossing between the Same Charge-Transfer States

3.1 Introduction

Thermally activated delayed fluorescence (TADF) has attracted great attention from the field of organic light emitting diodes (OLEDs) because it can achieve 100% internal quantum efficiency (IQE) of electroluminescence through the reverse intersystem crossing (rISC) process in pure organic molecules.^[1-3] To realize efficient rISC, Adachi *et al.* first embodied a molecular design strategy by using intramolecular charge transfer (ICT) mechanism between bulky electron donor (D) and acceptor (A) units which spatially separate the highest occupied molecular orbital (HOMO) and lowest unoccupied molecular orbital (LUMO) to ensure minimized ΔE_{ST} .^[4-8] Subsequently, Monkman *et al.* proposed a three-level model which could explain the increased rISC rate in TADF materials; the locally excited triplet state (³LE) should be located sufficiently close to the triplet charge transfer (³CT) state and/or be partially mixed with the ³CT, since the spin-orbit coupling (SOC) is forbidden between singlet charge transfer (¹CT) and ³CT states according to the spectroscopic selection rules.^[9-13]

On the other hand, a number of recent electroluminescent and photophysical investigations indicate that CT strength and thus the energetic proximity of ¹CT and ³CT states have decisive role for achievement of high rISC rates. Among the emitters with highly twisted structure of various TADF colors, those bearing stronger donors fragments with

electron-releasing substituents, and/or acceptor fragments with electron-withdrawing groups as well as other structural modifications providing stabilization of the CT states, exhibit generally faster rISC, shorter TADF lifetimes and/or higher EQE values.^[14-19] Such investigations question the key role of ³LE-state in achieving efficient rISC as they evidence that TADF can occur via direct two-state spin-flip mechanism either. In this context, to understand the reasons of rISC enhancement under finely controlled energy separation of ¹CT and ³LE states, we have recently developed a rotationally- and vibronically-assisted SOC model which explains TADF in a DMAC-TRZ emitter and its derivatives as a result of direct ³CT–¹CT two-state model.^[20,21]

Since TADF materials exhibit emission through the ICT mechanism, the emission wavelength could be systematically tuned through control of ICT state by different combination of D and A units.^[22,23] The design of most demanded fast-rISC deep-blue emitters is highly challenging, because the molecular systems with such higher energies of CT states exhibit slower rISC and worse OLED performance. Obviously, the ambiguity of TADF mechanism is a serious problem for further progress in this field. The question is thus whether molecular design of fast-rISC materials with a given TADF color should focus on the optimization of (i) the ³CT–¹CT transition parameters like the $\Delta E_{\text{ICT-3CT}}$ energy gap as two-state model predicts or (ii) on the ³LE–^{1,3}CT interactions, adjustment of the ³LE-state energy and minimization of the $\Delta E_{\text{ICT-3LE}}$ energy gap.

It should be noted that direct ³CT–¹CT transition itself is poorly investigated, especially in the fast-rISC emitters with orthogonal donor-acceptor units.^[24] The lack of experimental data on structural and electronic parameters affecting ³CT–¹CT transition as well as computational protocol for modeling of its rates in solid films is another serious barrier for further progress in the blue-emitters design.

In the present work, we have explored a structure-property relationship for fine tuning emission wavelength with maintaining TADF characteristics through substituent engineering. Even though improved TADF molecules have also been reported by introducing substituents occasionally, they are usually focused on developing high efficiency devices.^[25-30] As such, there has been still a lack of comprehensive structure-property correlation work regarding the systematic control of the energy states and important TADF characteristics like rISC rate.^[31] DMAC-DPS, a high-efficiency symmetric blue TADF material (467 nm), was selected in this work to demonstrate the substituent engineering for fine tuning of blue TADF materials.^[32] We first designed a donor-acceptor (D-A-H) structure by removing one donor part in the symmetric TADF emitters (D-A-D) to closely examine the electronic interactions between donor and acceptor part. Then a substituent unit (X) was introduced on the *para*-H position of D-A-H to modulate the electronic effects while keeping the steric situation between the D and A unchanged (**Figure 3.1**). Designing such introduction of X into A unit is based on the observation that the ³LE state is localized in the D unit according to the literature.^[32] Our intention was thus to keep ³LE energy invariant while varying the ^{1,3}CT states by different ICT strength in this D-A-X series, to test if rISC is directly dependent on the ³LE-¹CT transition as the three-level model suggests. Six different substituents (X) in this D-A-X series were chosen by Hammett parameters from electron donating groups (EDGs) to electron withdrawing groups (EWGs).^[33,34] Comprehensive photophysical studies were carried out to demonstrate the systematic control over the energy states and kinetic parameters, and OLED devices were fabricated and characterized to explore their potential in high efficiency blue OLED application.

Thanks to the simultaneous fine tuning of the $\Delta E_{1CT-3CT}$ and $\Delta E_{1CT-3LE}$ values, these investigations shed light on TADF mechanism in more general sense. Experimental photophysical data explained by a computational model based on Marcus theory revealed that

within the emitters of D-A structure, the rISC rate via $^3\text{LE}-^1\text{CT}$ transition is limited due to high reorganization energy to throw doubt on the three-level model. On the other hand, the $^3\text{CT}-^1\text{CT}$ transition promoted by molecular rotations and vibrations can provide much higher rISC rates. It was evidenced in this work that the optimization of parameters of the $^3\text{CT}-^1\text{CT}$ direct spin-flip together with tuning of the emission color should be a fruitful direction in the molecular design of efficient TADF emitters including the deep-blue ones.

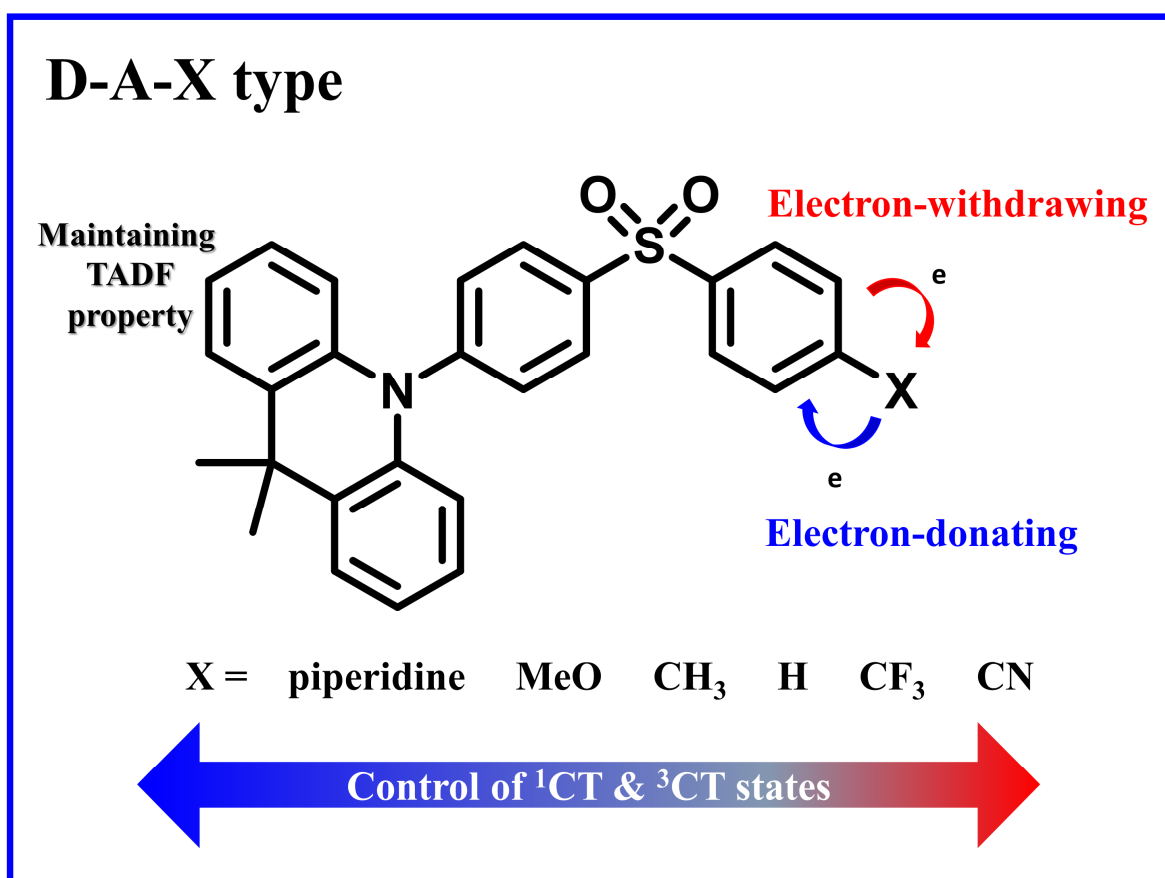
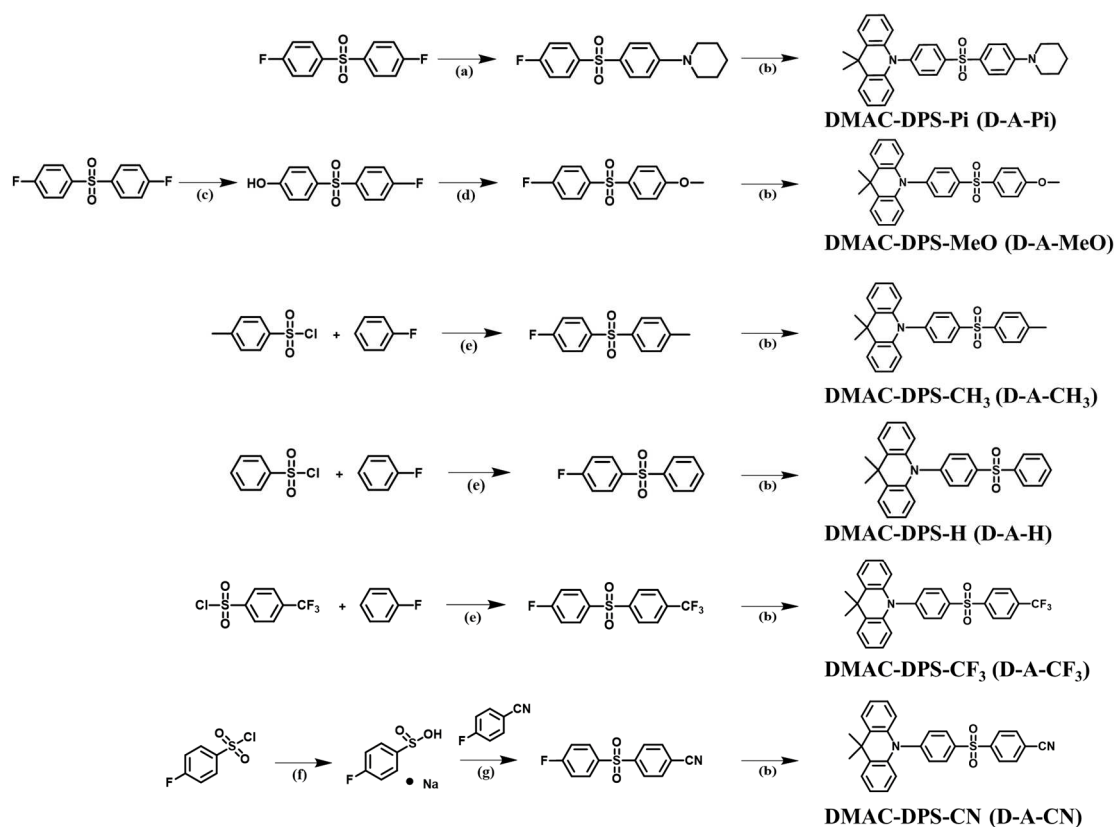


Figure 3.1 Structures of D-A-X type derivatives.

3.2 Experimental Methods

3.2.1 Synthesis of Materials



Scheme 3.1 Synthetic routes of D-A-X derivatives and their chemical structures. (a) piperidine, K₂CO₃, anhydrous DMF, 55 °C (b) DMAC, NaH, anhydrous DMF, 55 °C (c) KOH, DMSO, 75 °C (d) CH₃I, K₂CO₃, DMF, 75 °C (e) FeCl₃, 40 °C (f) NaSO₃, NaHCO₃, H₂O, 80 °C (g) DMSO, 120 °C

All reagents were purchased from Sigma Aldrich, TCI, and Alfa Aesar. All experimental glassware was dried in an oven, and all experimental conditions were conducted in an argon or nitrogen environment. The target D-A-X material were synthesized through the following **scheme 3.1**.

Synthesis of 1-(4-((4-fluorophenyl)sulfonyl)phenyl)piperidine

Bis(4-fluorophenyl) sulfone (3.10 g, 12.2 mmol), potassium carbonate (1.69 g, 12.2 mmol) and piperidine (1.04 g, 12.2 mmol) were dissolved in 50 mL DMF. The mixture was stirred at 55 °C under Ar atmosphere. After 12 h, the resulting product was poured into water (300 mL) and extracted with DCM. The combined organic phase was dried with MgSO₄ and concentrated under reduced pressure. The concentrated crude product was purified by column chromatography to afford 1-(4-((4-fluorophenyl)sulfonyl)phenyl)piperidine as a white powder (2.04 g, 52.5 %). ¹H NMR (300 MHz, CDCl₃, δ): 8.00 – 7.85 (m, 2H), 7.72 (d, *J* = 8.8 Hz, 2H), 7.13 (t, *J* = 8.1 Hz, 2H), 6.85 (d, *J* = 7.9 Hz, 2H), 3.33 (s, 4H), 1.64 (s, 6H).

Synthesis of DMAC-DPS-Pi (D-A-Pi)

A round-bottom flask equipped with a magnetic stirrer bar was baked under reduced pressure and Ar backfilled. Then, dimethylacridine (1.97 g, 9.39 mmol), NaH (0.28 g, 10.33 mmol), anhydrous DMF (20 mL) were added to the baked flask. After 30 min at room temperature, 1-(4-((4-fluorophenyl)sulfonyl)phenyl)piperidine (3 g, 9.39 mmol) in anhydrous DMF (10 mL) was added to the reaction mixture. After stirring 10 min, the reaction mixture was stirred at 55 °C under Ar atmosphere. After 4 h, the resulting product was poured into water (400 mL) and extracted with DCM. The combined organic phase was dried with MgSO₄ and concentrated under reduced pressure. The concentrated crude product was purified by column chromatography and the resulting solid was washed with methanol and recrystallized from chloroform/methanol to afford DMAC-DPS-Pi as a white powder (3.41 g, 71.4%). ¹H NMR (300 MHz, CDCl₃, δ): 8.13 (d, *J* = 8.2 Hz, 1H), 7.84 (d, *J* = 9.0 Hz, 1H), 7.44 (d, *J* = 6.6 Hz, 2H), 6.93 (d, *J* = 8.2 Hz, 3H), 6.21 (s, 1H), 3.38 (s, 2H), 1.66 (s, 6H). ¹³C NMR (126 MHz,

CDCl₃, δ): 145.59, 142.84, 140.46, 131.73, 130.91, 130.04, 129.94, 126.60, 125.53, 114.56, 113.97, 48.66, 36.23, 31.23, 25.47, 24.39. HRMS m/z : calcd for C₃₂H₃₂N₂O₂S, 508.22; found, 509.2263.

Synthesis of 4-((4-fluorophenyl)sulfonyl)phenol

A round bottom flask containing a magnetic stirrer was charged with bis(4-fluorophenyl) sulfone (5 g, 19.66 mmol) and aqueous KOH (7 M, 5.618 mL, 39.33 mmol). To this mixture was added 10 mL of DMSO and the resulting solution was stirred at 70 °C under Ar atmosphere. After 20 h, the resulting product was poured into water (100 mL) and washed with toluene. The aqueous phase was recovered and acidified with HCl. The solution was stirred for 10 minutes and then filtered to afford 4-((4-fluorophenyl)sulfonyl)phenol as a white powder (3.97 g, 80.1 %). ¹H-NMR (300 MHz, DMSO-*d*₆, δ): 10.65 (s, 1H), 7.93 (d, J =8.85 Hz, 2H), 7.75 (d, J = 8.85 Hz, 2H), 7.40 (d, J = 8.85 Hz, 2H), 6.90 (d, J =8.85 Hz, 2H)

Synthesis of 1-fluoro-4-((4-methoxyphenyl)sulfonyl)benzene

4-((4-fluorophenyl)sulfonyl)phenol (3 g, 11.89 mmol), CH₃I (1.69 g, 11.89 mmol) and potassium carbonate (1.97 g, 14.27 mmol) were dissolved in 20 mL DMF. The mixture was stirred at 75 °C under Ar atmosphere. After 24 h, the resulting product was poured into water (200 mL) and extracted with DCM. The combined organic phase was dried with MgSO₄ and concentrated under reduced pressure. The concentrated crude product was purified by column chromatography to afford 1-fluoro-4-((4-methoxyphenyl)sulfonyl)benzene as a white powder (2.80 g, 88.5 %). ¹H NMR (300 MHz, CDCl₃, δ): 7.93 (dd, J = 8.8, 5.1 Hz, 2H), 7.86 (d, J = 8.9 Hz, 2H), 7.16 (t, J = 8.6 Hz, 2H), 6.97 (d, J = 8.9 Hz, 2H), 3.85 (s, 3H).

Synthesis of DMAC-DPS-MeO (D-A-MeO)

D-A-MeO was synthesized similarly to D-A-Pi, using 1-fluoro-4-((4-methoxyphenyl)sulfonyl)benzene (2.5 g, 9.39 mmol), dimethylacridine (1.97 g, 9.39 mmol), NaH (0.25 g, 10.33 mmol) and anhydrous DMF (20 mL). The product was obtained as a white powder (3.21 g, 75.5 %). ¹H NMR (300 MHz, CDCl₃, δ): 8.14 (d, *J* = 8.4 Hz, 2H), 7.98 (d, *J* = 8.9 Hz, 2H), 7.46 (dd, *J* = 8.9, 4.6 Hz, 4H), 7.05 (d, *J* = 8.8 Hz, 2H), 7.00 – 6.89 (m, 4H), 6.28 – 6.13 (m, 2H), 3.89 (s, 3H), 1.66 (s, 6H). ¹³C NMR (126 MHz, CDCl₃, δ): 146.17, 141.79, 140.40, 132.83, 131.52, 131.26, 130.36, 130.19, 126.60, 125.55, 121.61, 114.91, 114.76, 55.90, 36.29, 31.13. HRMS *m/z*: calcd for C₂₈H₂₅NO₃S, 455.16; found, 456.1653.

Synthesis of 1-fluoro-4-tosylbenzene

A round-bottom flask equipped with a magnetic stirrer bar was baked under reduced pressure and Ar backfilled. Then, 4-methylbenzenesulfonyl chloride (5 g, 26.27 mmol) and fluorobenzene (7.56 g, 78.68 mmol) were added to the baked flask. To this mixture was added FeCl₃ (5.32 g, 32.78 mmol) and the resulting solution was stirred at 40 °C under Ar atmosphere. After 2 h, DCM (50 mL) was added to the flask, dilute hydrochloric acid was slowly added, and stirring was continued until no precipitation was observed. Then, the resulting product was poured into water (300 mL) and extracted with DCM. The combined organic phase was dried with MgSO₄ and concentrated under reduced pressure. The concentrated crude product was purified by column chromatography to afford 1-fluoro-4-tosylbenzene as a white powder (4.49 g, 68.4 %). ¹H NMR (300 MHz, CDCl₃, δ): 7.94 (dd, *J* = 8.7, 5.1 Hz, 2H), 7.81 (d, *J* = 8.2 Hz, 2H), 7.30 (d, *J* = 8.1 Hz, 2H), 7.16 (t, *J* = 8.5 Hz, 2H), 2.40 (s, 3H).

Synthesis of DMAC-DPS-CH₃ (D-A- CH₃)

D-A-CH₃ was synthesized similarly to D-A-Pi, using 1-fluoro-4-tosylbenzene (2g, 7.99 mmol), dimethylacridine (1.67 g, 7.99 mmol), NaH (0.21 g, 8.79 mmol) and anhydrous DMF(20 mL). The product was obtained as a white powder (2.47 g, 70.2 %). ¹H NMR (300 MHz, CDCl₃, δ): 8.15 (d, *J* = 8.6 Hz, 2H), 7.94 (d, *J* = 8.3 Hz, 2H), 7.54 – 7.42 (m, 4H), 7.38 (d, *J* = 8.1 Hz, 2H). ¹³C NMR (126 MHz, CDCl₃, δ): 146.34, 144.74, 141.30, 140.38, 138.43, 131.38, 130.36, 130.31, 128.16, 126.59, 125.53, 121.66, 114.84, 36.29, 31.07, 21.85. HRMS *m/z*: calcd for C₂₈H₂₅NO₂S, 439.16; found, 440.1684.

Synthesis of 1-fluoro-4-(phenylsulfonyl)benzene

1-fluoro-4-(phenylsulfonyl)benzene was synthesized similarly to 1-fluoro-4-tosylbenzene, using benzenesulfonyl chloride (5 g, 28.31 mmol), fluorobenzene (8.16 g, 84.93 mmol) and FeCl₃ (5.74 g, 35.39 mmol). The product was obtained as a white powder (4.98 g, 74.5 %). ¹H NMR (300 MHz, CDCl₃, δ): 8.01 – 7.87 (m, 4H), 7.63–7.47 (m, 3H), 7.18 (t, *J* = 8.6 Hz, 2H).

Synthesis of DMAC-DPS-H (D-A- H)

D-A-H was synthesized similarly to D-A-Pi, using 1-fluoro-4-(phenylsulfonyl)benzene (2.5 g, 10.58 mmol), dimethylacridine (2.21 g, 10.58 mmol), NaH (0.28 g, 11.64 mmol) and anhydrous DMF(20 mL). The product was obtained as a white powder (3.17 g, 70.5 %). ¹H NMR (300 MHz, CDCl₃, δ): 8.22 (d, *J* = 8.5 Hz, 2H), 8.07 (d, *J* = 8.0 Hz, 2H), 7.80-7.65 (m, 3H), 7.63 (d, *J* = 8.3 Hz, 2H), 7.50 (d, *J* = 7.3 Hz, 2H), 7.03-6.90 (m, 4H), 6.18 (d, *J* = 7.47 Hz,

2H), 1.59 (s, 6H). ^{13}C NMR (126 MHz, CDCl_3 , δ): 146.62, 141.44, 140.78, 140.38, 133.70, 131.59, 131.21, 130.52, 129.68, 128.11, 126.61, 125.55, 121.77, 115.00, 36.33, 31.02. HRMS m/z : calcd for $\text{C}_{27}\text{H}_{23}\text{NO}_2\text{S}$, 425.14; found, 426.1528.

Synthesis of 1-fluoro-4-((4-(trifluoromethyl)phenyl)sulfonyl)benzene

1-fluoro-4-((4-(trifluoromethyl)phenyl)sulfonyl)benzene was synthesized similarly to 1-fluoro-4-tosylbenzene, using 4-(trifluoromethyl)benzenesulfonyl chloride (7 g, 28.62 mmol), fluorobenzene (8.25 g, 85.85 mmol) and FeCl_3 (5.80 g, 35.77 mmol). The product was obtained as a white powder (2.63 g, 30.2 %). ^1H NMR (300 MHz, CDCl_3 , δ): 8.06 (d, $J = 8.2$ Hz, 1H), 7.98 (dd, $J = 8.8, 5.0$ Hz, 1H), 7.78 (d, $J = 8.3$ Hz, 1H), 7.22 (t, $J = 8.5$ Hz, 1H).

Synthesis of DMAC-DPS- CF_3 (D-A- CF_3)

D-A- CF_3 was synthesized similarly to D-A-Pi, using 1-fluoro-4-((4-(trifluoromethyl)phenyl)sulfonyl)benzene (2.5 g, 8.22 mmol), dimethylacridine (1.72 g, 8.22 mmol), NaH (0.27 g, 9.04 mmol) and anhydrous DMF (20 mL). The product was obtained as a white powder (2.65 g, 65.3 %). ^1H NMR (300 MHz, $\text{DMSO}-d_6$, δ): 8.28 (dd, $J = 12.2, 8.5$ Hz, 2H), 8.08 (d, $J = 8.2$ Hz, 1H), 7.65 (d, $J = 8.5$ Hz, 1H), 7.51 (d, $J = 7.2$ Hz, 1H), 7.08 – 6.88 (m, 2H), 6.26 (d, $J = 7.9$ Hz, 1H), 1.59 (s, 3H). ^{13}C NMR (126 MHz, CDCl_3 , δ): 147.49, 145.19, 140.32, 138.98, 135.41, 132.56, 130.73, 130.25, 128.6, 126.86, 126.60, 125.56, 122.19, 115.71, 36.50, 30.75. HRMS m/z : calcd for $\text{C}_{28}\text{H}_{22}\text{F}_3\text{NO}_2\text{S}$, 493.13; found, 494.1402.

Synthesis of sodium 4-fluorobenzenesulfinate

Sodium sulfite (2.59 g, 20.55 mmol), sodium bicarbonate (1.73g, 20.55 mmol) and 4-fluorobenzenesulfonyl chloride (2 g, 10.28 mmol) were dissolved in 10 mL H₂O. The mixture was stirred at 80 °C under Ar atmosphere. After 4 h, H₂O was removed in vacuo and ethanol was added to this white residue and the resulting solution was filtered. The filtrate was concentrated under reduced pressure to afford 4-fluorobenzenesulfinate as a white powder (1.39 g, 74.0 %). ¹H NMR (300 MHz, D₂O, δ): 7.74 – 7.61 (m, 1H), 7.27 (t, J = 8.9 Hz, 1H).

Synthesis of 4-((4-fluorophenyl)sulfonyl)benzonitrile

To a solution of 4-fluorobenzonitrile (6 g, 49.54 mmol) in 20 mL of DMSO at 120 °C was added dropwise of sodium 4-fluorobenzenesulfinate (3.01g, 16.51 mmol) in 20 mL of DMSO. The mixture was stirred at 120 °C under Ar atmosphere. After 24 h, the resulting product was poured into water (400 mL) and extracted with DCM. The combined organic phase was dried with MgSO₄ and concentrated under reduced pressure. The concentrated crude product was purified by column chromatography to afford 4-((4-fluorophenyl)sulfonyl)benzonitrile as a white powder (1.29 g, 29.5 %). ¹H NMR (300 MHz, DMSO-*d*₆, δ): 8.23-8.05 (m, 3H), 7.50 (t, J = 8.8 Hz, 1H).

Synthesis of DMAC-DPS-CN (D-A-CN)

D-A-CN was synthesized similarly to D-A-Pi, using 4-((4-fluorophenyl)sulfonyl)benzonitrile (2.5 g, 9.57 mmol), dimethylacridine (2.00 g, 9.57 mmol), NaH (0.25 g, 10.53 mmol) and anhydrous DMF (20 mL). The product was obtained as a white powder (2.79 g, 64.8 %). ¹H NMR (300 MHz, DMSO-*d*₆, δ): 8.25 (d, J = 6.9 Hz, 4H), 8.17 (d, J = 8.5 Hz, 2H), 7.65 (d, J = 8.6 Hz, 2H), 7.51 (d, J = 8.8 Hz, 2H), 6.99 (t, J = 7.0 Hz, 4H), 6.26 (d, J = 7.7 Hz, 2H), 1.59

(s, 6H). ^{13}C NMR (126 MHz, CDCl_3 , δ): 147.81, 145.90, 140.28, 138.09, 133.49, 133.13, 130.78, 129.58, 128.62, 126.59, 125.56, 122.43, 117.36, 116.13, 36.58, 30.57. HRMS m/z : calcd for $\text{C}_{28}\text{H}_{22}\text{N}_2\text{O}_2\text{S}$, 450.14; found, 451.1480.

3.2.2 General methods

Chemical structures were identified by ^1H NMR (Bruker, ADVANCE-300 and ADVANCE-500), ^{13}C NMR (Bruker, Advance-500), high-resolution mass spectrometry (AB SCIEX, Q-TOF 5600), and elemental analysis (Thermo Fisher Scientific, Flash 1112). UV-vis absorption spectra were recorded using a SHIMADZU UV-1650PC. Steady-state photoluminescence (PL) spectra were obtained with a PTI QuantaMaster 40 spectrofluorometer at room temperature and absolute PL quantum yields (PLQY) were recorded using a 3.2 inch integrating sphere. Low temperature photoluminescence spectra were measured using a Jasco FP-6500 at 78 K. Photoluminescence decay traces were obtained through the time correlated single photon counting (TCSPC) techniques by using a PicoQuant, FluoTime 250 instrument (PicoQuant, Germany). A 377 nm pulsed laser was used as an excitation source and temperature dependent studies were made with a cryostat (Oxford Instruments, Optistat DN). Data analyses were performed using exponential fitting models by FluoFit software. Cyclic voltammetry measurements were performed using a 273A (Princeton Applied Research). Each oxidation potential was calibrated using ferrocene as a reference. LUMO levels were evaluated from the HOMO level and the optical band gap which was obtained from the edge of the absorption spectra.

3.2.3 Determination of photophysical parameters

The rates and yields of the photophysical processes were calculated using equations described in the literature.^{S1} Briefly, fitting the photoluminescence decay curves using the exponential functions gave the lifetimes (τ_i) and pre-exponential factors (A_i) of the emissive components:

$$I(t) = i_0 + \sum_{i=1}^n A_i e^{-\frac{t}{\tau_i}}, \quad (1)$$

where I is the emission intensity, i_0 is the maximum intensity and t is the time.

Intensity weighted mean lifetime values were used for polyexponential decays of prompt (PF) or delayed (DF) fluorescence. The ratio of DF and PF quantum yields (ϕ_{DF}/ϕ_{PF}) was determined as following:

$$\frac{\phi_{DF}}{\phi_{PF}} = \frac{A_{DF}\tau_{DF}}{A_{PF}\tau_{PF}}, \quad (2)$$

where A_{DF} and A_{PF} are pre-exponential factors of prompt and delayed fluorescence lifetimes, respectively; τ_{PF} and τ_{DF} are lifetimes of prompt and delayed fluorescence, respectively. Rate constants of radiative (k_r) and nonradiative (k_{nr}) decay, and intersystem crossing (k_{ISC}) were given by equations:

$$k_r = \frac{\phi_{PF}}{\tau_{PF}}, \quad (3)$$

$$k_{ISC} = \frac{\phi_{DF}}{\tau_{PF}\phi}, \quad (4)$$

$$k_{nr} = \frac{1}{\tau_{PF}} - (k_r + k_{ISC}), \quad (5)$$

where ϕ is PLQY ($\phi_{DF} + \phi_{PF}$).

Further, the quantum yields of ISC and rISC were calculated as

$$\phi_{ISC} = k_{ISC}\tau_{PF}, \quad (6)$$

$$\phi_{rISC} = \frac{1-\phi_{PF}/\phi}{\phi_{ISC}} \quad , \quad (7)$$

And finally, rate constant of rISC (k_{rISC}) was calculated as

$$k_{rISC} = \frac{\phi_{rISC}}{\tau_{DF}} (\phi/\phi_{PF}), \quad (8)$$

k_{rISC}/k_{ISC} ratio was calculated as

$$k_{rISC}/k_{ISC} \text{ ratio} = \frac{k_{rISC}}{k_{ISC}}, \quad (9)$$

Respective errors were calculated using the exact differential method

$$y = f(x_1, x_2, \dots, x_n)$$

$$\Delta y = \left| \frac{\partial f}{\partial x_1} \right| \cdot \Delta x_1 + \left| \frac{\partial f}{\partial x_2} \right| \cdot \Delta x_2 + \dots + \left| \frac{\partial f}{\partial x_n} \right| \cdot \Delta x_n$$

Where y and Δy are function and error of function, respectively. x_n and Δx are variable and error of respective values, respectively.

In this case, the function are k_{ISC} , k_{rISC} and k_{rISC}/k_{ISC} ratio.

The variables are ϕ , ϕ_{PF} , ϕ_{DF} , τ_{PF} and τ_{DF} .

3.2.4 Theoretical Calculations

Quantum chemical calculations were conducted at the DFT/TD-DFT level of theory using Gaussian 16 program package. The B3LYP functional was used with the cc-pVDZ basis set. The unconstrained geometry optimizations were performed for the ground (S_0), excited singlet (S_1) and excited triplet electronic states (T_1 , T_2 , T_3). Convergence of all geometry optimizations was verified by the vibrational analysis: no negative frequencies were observed, therefore calculated minima correspond to “true” stationary points. The nature of electronic excited states was determined by the analysis of molecular orbitals. Spin-orbit coupling constants were computed using ORCA 4.2 software package with B3LYP functional, and DEF2-TZVP basis

set with included relativistic zero-order regular approximation (ZORA). Detailed procedures for calculation of energy gaps, reorganization energies, and rISC rate constants for each rotamer are described below in the respective sections.

3.2.5 Devices fabrication and characterization

The patterned ITO substrates were rinsed with acetone and isopropyl alcohol using sonication for 15 min, followed by 15 min UV-ozone-treatment. Organic layers, MoO₃ and Al were thermally evaporated at a deposition rate of 0.6–1 Å s⁻¹ for organic layers, 0.2 Å s⁻¹ for MoO₃, and 4–5 Å s⁻¹ for Al electrode. The current–voltage–luminance (I–V–L) characteristics of the devices were measured with a Keithley-236 source-measure unit, a Keithley-2000 multimeter unit, and a calibrated Si photodiode (Hamamatsu S5227-1010BQ). The luminance and efficiencies were calculated from the photocurrent measurement data obtained with the Si photodiode. The electroluminescence spectra were obtained by using a spectroradiometer (CS-2000).

3.3 Results and Discussion

3.3.1 Material Design

For the demonstration of systematic control of the energy states, six target molecules were designed and synthesized. DMAC-DPS was selected as a reference molecule because it is one of the highly efficient blue TADF emitters.^[32] We first designed an asymmetric donor-acceptor molecule (D-A-H) with dimethylacridine donor as the donor moiety (D) and diphenyl sulfone (DPS) as the acceptor units (A) to form a structural platform for substituent engineering aiming at the ICT energy control. Importantly, six small substituents (X) were introduced in

the opposite side of acceptor side phenyl ring for fine tuning of the electronic states involved in the emission while minimizing the effect of dihedral angle between D-A and also of lowest triplet states localized on D and/or A fragments (^3LE). The substituent units cover a broad range of Hammett parameters. We utilized piperidine (D-A-Pi), methoxy (D-A-MeO), and methyl (D-A-CH₃) as electron-donating groups (EDGs). On the other hand, trifluoromethyl (D-A-CF₃) and cyano (D-A-CN) were adopted as the electron-withdrawing groups (EWGs).

3.3.2 Electrochemical Properties

In order to evaluate the energy level of these compounds, cyclic voltammetry (CV) was carried out in acetonitrile solution (**Figure 3.2**). All materials showed similar oxidation potential values and HOMO levels (-5.40 eV), which should originate from the same acridine donor. On the other hand, the reduction potentials and LUMO level were affected by substituent units. The reduction potentials shift to higher potentials from -1.96 eV (D-A-Pi) to -1.34 eV (D-A-CN) and the LUMO energy level of the compounds were calculated to be -2.37, -2.41, -2.44, -2.48, 2.51, -2.79 and -2.99 eV for D-A-Pi, D-A-MeO, D-A-CH₃, D-A-H, D-A-D, D-A-CF₃ and D-A-CN, respectively. The LUMO levels became shallower by introducing EDGs (-Pi, -MeO, -CH₃) while the presence of the EWGs (-CF₃, -CN) resulted in the deeper LUMO levels. Hence, the substitution at *para* position of the phenyl group (X position) with EDGs/EWGs effectively tuned the LUMO energy level. As a result, the magnitude of band gap followed the order of D-A-Pi>D-A-MeO>D-A-CH₃>D-A-H>D-A-D>D-A-CF₃>D-A-CN. We then correlated the electrochemical properties with the Hammett constants (**Figure 3.2b**). The LUMO levels showed a linear relationship with push-pull Hammett constant of the substituents.

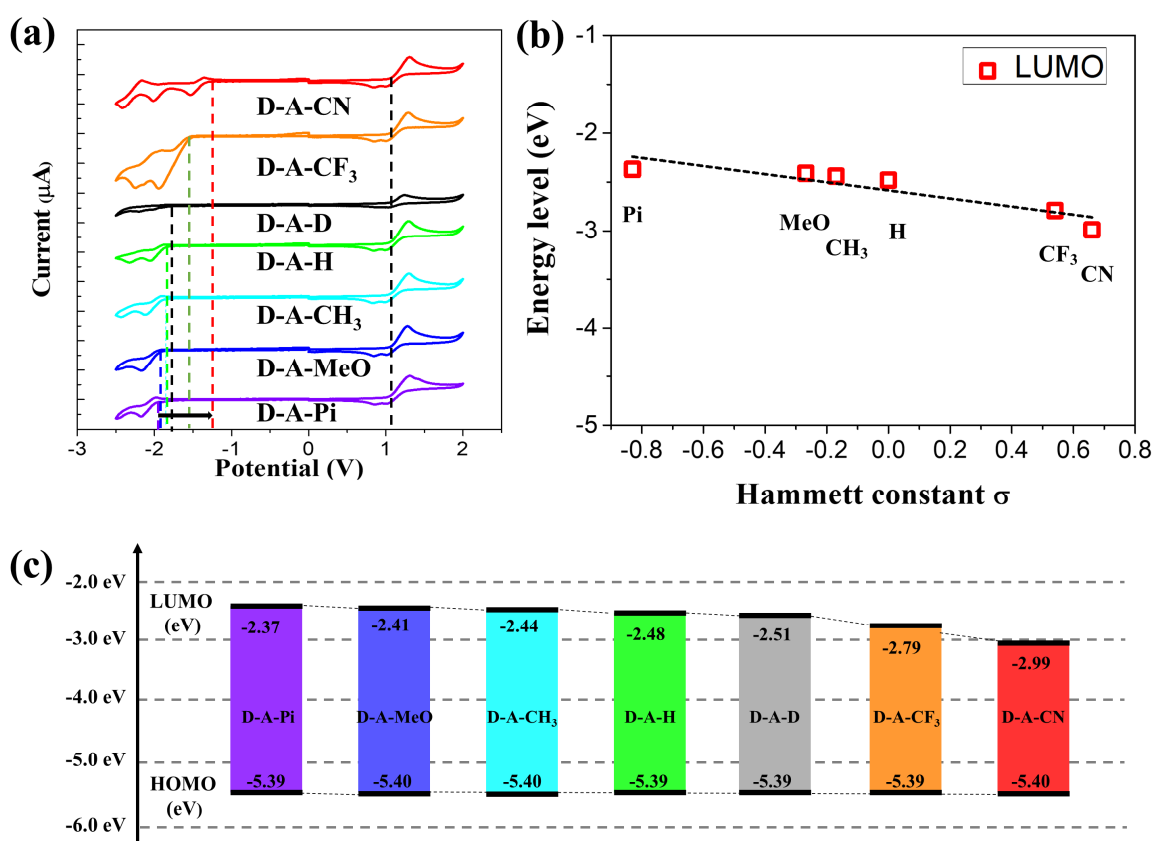


Figure 3.2 (a) Cyclic voltammetry of D-A-X materials. (b) Correlation of LUMO energy levels with Hammett constant. (c) HOMO and LUMO energy levels for D-A-X derivatives.

3.3.3 Photophysical Properties

Photophysical properties of D-A-X derivatives were evaluated by steady-state UV-visible absorption (UV-vis) and photoluminescence emission (PL) spectra. (**Figure 3.3** and **Table 3.1**). All D-A-X compound showed the intense absorption band in UV-light region at around 300 nm - 350 nm, which could be attributed to the π - π^* transition of the respective donor or acceptor moieties. Moreover, D-A-X derivatives exhibited weak and broad absorption band in the region of 330 nm - 440 nm, which could be assigned as the ICT transition from the dimethylacridine donor (D) to substituted diphenyl sulfone acceptor units (A-X). DMAC-DPS

(D-A-D) exhibits a CT absorption band centered at 370 nm with absorption coefficient (ϵ) of $2100 \text{ M}^{-1}\text{cm}^{-1}$. On the other hand, D-A-H showed a 4 nm blue-shift of CT absorption band ($\lambda_{\text{abs,max}}=366 \text{ nm}$) and ϵ value ($1100 \text{ M}^{-1}\text{cm}^{-1}$) decreased by half compared to that of D-A-D. Depending on the electronic push/pull capability of the substituents (X), the CT absorption band maximum ($\lambda_{\text{abs,max}}$) was hypsochromically/bathochromically shifted ranging over 356 nm to 388 nm. The introduction of electron-releasing substituents on the X position caused hypsochromic shift of CT absorption band compared to D-A-H (356, 363 and 365 nm for D-A-Pi, D-A-MeO and D-A-CH₃, respectively). On the other hand, the introduction of electron-withdrawing substituents on the X position caused bathochromic shift of CT absorption band compared to D-A-H (379 and 388 nm for D-A-CF₃ and D-A-CN, respectively).

In toluene solutions, the PL spectra of D-A-X compounds showed broad ICT emission with a maximum ranging from 446 nm (deep blue) to 487 nm (sky blue) (**Figures 3.3b**). D-A-H exhibited blue ($\lambda_{\text{PL,max}}=456 \text{ nm}$) fluorescence emission, which was blue-shifted (8 nm) as compared to that of D-A-D ($\lambda_{\text{PL,max}}=464 \text{ nm}$). The electron-releasing substituents at the X position caused hypsochromic shift of photoluminescence compared to D-A-H ($\lambda_{\text{PL,max}} = 446 \text{ nm}$ for D-A-Pi, 449 nm for D-A-MeO, and 454 nm for D-A-CH₃). Such a behavior was caused by the decreased electron-accepting power of the diphenylsulfone (DPS), resulting in a decreased ICT strength and thus the increase in the ¹CT-state energy. On the other hand, the electron-withdrawing substituents caused bathochromic shift of PL compared to D-A-H ($\lambda_{\text{PL,max}} = 477 \text{ nm}$ for D-A-CF₃, and 487 nm for D-A-CN) due to electron-withdrawing units enhancing the accepting power of DPS.

The emission spectra of these compounds in 10 wt% DPEPO film also showed fine tuning of their emission wavelength like in solution state (**Figure 3.3c**, DPEPO is a host material for OLED device, *vide infra*). The values of PL quantum yields (PLQYs, Φ_{PL}) of D-

A-X derivatives are moderate to high as shown in **Table 3.1**, and those are always higher in film than in solution.

The nonradiative rate constant (k_{nr}) in solution is considerably larger than that in film (**Table 3.2**), implying that the excited molecules in solutions deactivate to the ground state faster through the nonradiative pathways than in films because solid matrix should suppress some of molecular vibrational motions. In the film matrix, the PLQYs of D-A-Pi, D-A-MeO, D-A-CH₃, D-A-H, D-A-CF₃ and D-A-CN were measured to be 0.62, 0.82, 0.81, 0.82, 0.95 and 0.96, respectively. The emission maximum exhibited a linear relationship with Hammett constant of the substituents (**Figure 3.3d**). It is thus obvious that the absorption and emission properties can be effectively modulated by push/pull substituents.

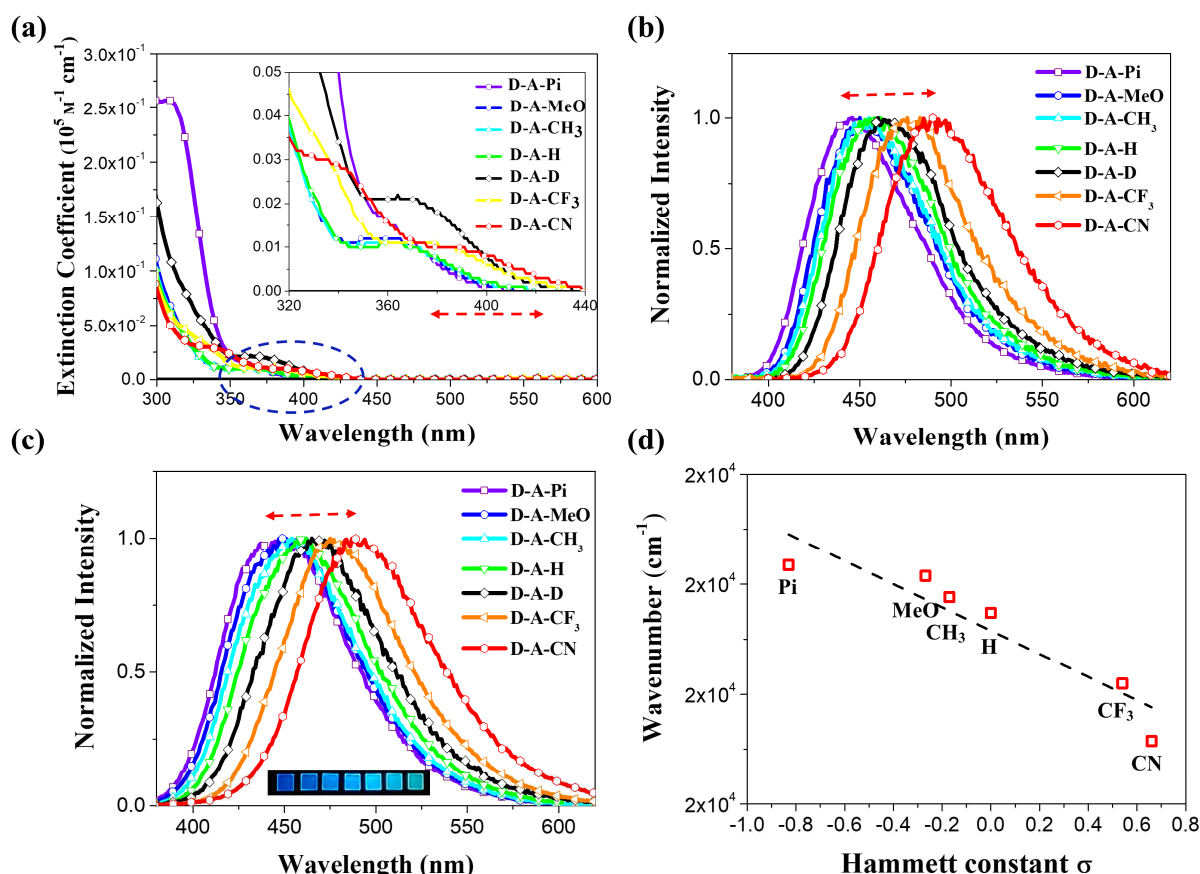


Figure 3.3 Optical properties of D-A-X derivatives. (a) absorption spectra (toluene, $c=1 \times 10^{-5} \text{ M}$) (b) normalized photoluminescence (toluene, $c=1 \times 10^{-5} \text{ M}$) (c) normalized

photoluminescence (10 wt% in DPEPO film) (d) correlation of photoluminescence maximum with Hammett constant (10 wt% in DPEPO film)

Table 3.1 The summary of physical and photophysical properties of D-A-X derivatives.

	$\lambda_{\text{abs,max}}^{\text{a)}$	$\epsilon^{\text{a)}$	$\lambda_{\text{PL,max}}^{\text{b,c)}$	$\Phi_{\text{ab}}^{\text{d,e)}$	$E_{1\text{CT}}^{\text{f)}$	$E_{3\text{LE}}^{\text{g)}$	$E_{3\text{CT}}^{\text{h)}$	$\Delta E_{1\text{CT-3CT}}^{\text{i)}$	$\Delta E_{1\text{CT-3LE}}^{\text{j)}$	HOMO ^{k)}	LUMO ^{k)}
	[nm]	[M ⁻¹ cm ⁻¹]	[nm]	[%]	[eV]	[eV]	[eV]	[meV]	[meV]	[eV]	[eV]
D-A-Pi	356	1700	446/448	50/62	3.22	3.12 (A)	3.123	97	100	-5.39	-2.37
D-A-MeO	363	1200	449/450	66/82	3.17	3.19 (D)	3.095	75	-20	-5.40	-2.41
D-A-CH ₃	365	1100	454/457	65/81	3.14	3.19 (D)	3.085	55	-50	-5.40	-2.44
D-A-H	366	1100	456/460	67/82	3.09	3.19 (D)	3.049	41	-100	-5.39	-2.48
DMAC-DPS	370	2100	464/466	74/82	3.04	3.19 (D)	3.007	33	-150	-5.39	-2.51
D-A-CF ₃	379	1100	477/478	85/95	2.96	3.19 (D)	2.954	6	-230	-5.39	-2.79
D-A-CN	388	1000	487/488	89/96	2.91	3.19 (D)	2.907	3.1 ^{l)}	-280	-5.40	-2.99

^{a)}UV-vis absorption measured in 1x10⁻⁵ M toluene solution; ^{b)}PL spectra measured in 1x10⁻⁵ M toluene solution; ^{c)}PL spectra measured in 10 wt% DPEPO doping films; ^{d)}Absolute PL quantum yields (PLQY) recorded in 1x10⁻⁵ M toluene solutions saturated with Ar; ^{e)}Absolute PL quantum yields (PLQY) recorded in 10 wt% DPEPO doping films using an integrating

sphere; ^f)the ¹CT energy estimated from onsets of the fluorescence spectra in 10 wt% DPEPO doping films; ^g)the ³LE energy estimated from the phosphorescence onsets of free donor or acceptor in toluene solutions at 78 K, D and A denotes the lowest excited triplet state localized on the donor and acceptor fragment, respectively; ^h)the ³CT energy in the DPEPO films calculated as: $E_{3CT} = E_{1CT} - \Delta E_{1CT-3CT}$; ⁱ)the difference of fluorescence and phosphorescence onsets in toluene solutions of D-A emitters at 78 K; ^j)difference of the E_{1CT} of D-A emitters in the DPEPO films and E_{3LE} of free donor or acceptor, negative value means that ³LE state has higher energy than the ¹CT one; ^k)HOMO and LUMO levels determined by cyclic voltammetry in 5×10^{-3} M acetonitrile solutions using ferrocene as a reference; ^l)computed value.

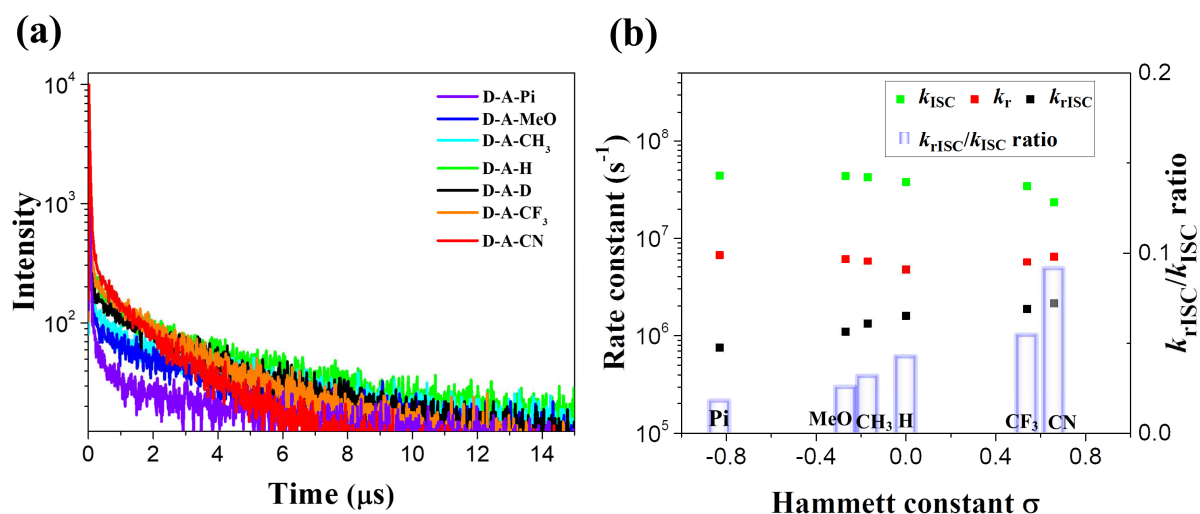


Figure 3.4 (a) Temperature-dependent PL decay spectra (10 wt% in DPEPO film) (b) The rate constants of radiative process (10 wt% in DPEPO film)

Table 3.2 The summary of rate constants of D-A-X derivatives in DPEPO films.

	$\tau_{PF}^{a)}$	$\tau_{DF}^{a)}$	$\Phi_{PF}^{b)}$	$\Phi_{DF}^{b)}$	k_r	k_{nr}	k_{ISC}	k_{rISC}	k_{rISC}/k_{ISC}
	[ns]	[μ s]	[%]	[%]	[10^6 s^{-1}]	[10^6 s^{-1}]	[10^6 s^{-1}]	[10^6 s^{-1}]	ratio
D-A-Pi	18.2	6.6	12.3	49.7	6.74	4.13	44 \pm 6	0.76	0.017
	± 1.5	± 0.3	± 0.3	± 1.2				± 0.07	± 0.004
D-A-MeO	19.6	6.2	12.0	70.0	6.12	1.34	43 \pm 6	1.10	0.025
	± 1.7	± 0.3	± 0.3	± 1.7				± 0.11	± 0.006
D-A-CH ₃	20.2	5.2	11.7	69.3	5.82	1.36	42 \pm 6	1.33	0.031
	± 1.8	± 0.2	± 0.3	± 1.7				± 0.13	± 0.008
D-A-H	23.0	4.75	10.8	71.2	4.71	1.03	38 \pm 5	1.60	0.042
	± 1.9	± 0.19	± 0.3	± 1.8				± 0.14	± 0.010
DMAC-DPS	22.8	5.0	11.5	70.5	5.03	1.10	37 \pm 5	1.44	0.038
	± 1.8	± 0.2	± 0.3	± 1.8				± 0.14	± 0.009
D-A-CF ₃	24.7	3.62	14.1	80.9	5.69	0.30	34 \pm 4	1.9	0.054
	± 1.8	± 0.16	± 0.4	± 2.0				± 0.2	± 0.012
D-A-CN	33	2.10	21.5	74.5	6.49	0.27	23 \pm 3	2.1	0.091
	± 2	± 0.08	± 0.5	± 1.9				± 0.2	± 0.019

^{a)}Lifetime calculated from the prompt (τ_{PF}) and delayed (τ_{DF}) fluorescence decay in DPEPO

10 wt% doping films; ^{b)} Φ_{PF} (the prompt PLQY) and Φ_{DF} (the delayed PLQY) were obtained from the prompt and delayed proportions in transient decay curves of 10 wt% DPEPO doping films; k_r , k_{nr} – the rate constant of radiative and nonradiative decay of singlet excited state; k_{ISC} , k_{rISC} – rate constant of intersystem crossing and reverse intersystem crossing.

3.3.4 Fluorescence decay profiles and their exciton dynamics

The transient decay lifetime measurement was carried out to explore different emission components of the D-A-X derivatives using the Time Correlated Single Photon Counting (TCSPC) technique in 10 wt% DPEPO film (**Figure 3.4a**). Notably, decay profiles of all D-A-X compound consisted not only of the prompt fluorescence (PF) but also of the delayed fluorescence (DF) regardless of substituents. The delayed fluorescence lifetime (τ_{DF}) of D-A-Pi, D-A-MeO, D-A-CH₃, D-A-H, D-A-D, D-A-CF₃ and D-A-CN were measured to be 6.67, 6.20, 5.18, 4.75, 4.96, 3.62 and 2.10 μ s, respectively (**Table 3.2**).

We further analyzed the exciton dynamics of the S₁ and T₁ states on the basis of their photophysical transition rates. The radiative rate constant (k_r) was obtained from PLQY and PF lifetime data (**Table 3.2**); in 10 wt% DPEPO, its values are in the 5-7 $\times 10^6$ s⁻¹ range. Interestingly, most of D-A-X compounds (except for D-A-Pi) exhibited relatively high k_{rISC} values (>10⁶ s⁻¹) compared with reported blue-region TADF materials. Such relatively high k_{rISC} as well as k_{ISC} values suggest strong interaction of the ¹CT, ³CT and/or ³LE states and efficient up-conversion of triplet excitons.

Relative energy and nature of the lowest triplet states play important roles in the photophysics of TADF materials. To analyze the features of triplet states and estimate the energy difference with the S₁-state, low temperature phosphorescence measurements were performed. (**Figure 3.5** and **Figure 3.6**). Both in films and frozen toluene at 78 K and 50 ms delay time, all the emitters showed a broad and structureless phosphorescence spectrum. Similar to the ¹CT fluorescence, its maximum and onset energy decreased with the introduction of electron-withdrawing substituents and increased with the electron-releasing ones. For these reasons, this phosphorescence was attributed to the emission from the ³CT-state (T₁), as was also supported by the calculated molecular orbitals involved in electronic transitions. To estimate the energy of higher triplet state (T₂) of ³LE nature, the phosphorescence spectra of

donor (*N*-phenyl-DMAC) and acceptor (substituted DPS) fragments were measured separately. By comparison, in all the cases except for the piperidine DPS acceptor, it turned out that the higher lying triplet state (T_2) of D-A-X are attributed to the ^3LE states localized on the donor unit (see $E_{3\text{LE}}$ column in **Table 3.1**: exception is D-A-Pi with ^3LE localized on acceptor unit) with unique vibronic structure. Thus, obtained energies of various states afforded energy gaps $\Delta E_{1\text{CT-3CT}}$ and $\Delta E_{1\text{CT-3LE}}$ listed in **Table 3.1**, and enabled further analysis of the mechanism of spin-flip transitions.

D-A-H showed $\Delta E_{1\text{CT-3CT}}$ (41 meV), $\Delta E_{1\text{CT-3LE}}$ (-100 meV), and DF lifetime ($\tau_{\text{DF}}=4.75$ μs) similar to that of D-A-D ($\Delta E_{1\text{CT-3CT}}=33$ meV, $\Delta E_{1\text{CT-3LE}}$ (-150 meV), and $\tau_{\text{DF}}=4.95$ μs). Their rate constants of reverse intersystem crossing (k_{rISC}) were thus also similar: 1.60×10^6 and 1.44×10^6 s^{-1} , respectively. In the compounds D-A- CF_3 and D-A-CN, where electron-withdrawing substituents were introduced into DPS, $\Delta E_{1\text{CT-3CT}}$ decreased sharply down to 6 and 3 meV, respectively, whilst $\Delta E_{1\text{CT-3LE}}$ increased up to -230 meV and -280 meV, respectively (**Table 3.1**). Therefore, due to the increase of acceptor strength, the ICT interaction increased, providing stabilization of the ^1CT and ^3CT states and simultaneously the decrease of energy gap between them. This led to the decrease of DF lifetime compared to D-A-H ($\tau_{\text{DF}}=3.62$ μs for D-A- CF_3 and 2.10 μs for D-A-CN), and thus k_{rISC} increased up to 2.1×10^6 s^{-1} . It should be noted here that the k_{rISC} value does not correlate with the $\Delta E_{1\text{CT-3LE}}$ different from the three-level model prediction.

On the other hand, in the case of D-A- CH_3 , D-A-MeO, and D-A-Pi with electron-releasing substituents, the $\Delta E_{1\text{CT-3CT}}$ values increased up to 55, 75 and 100 meV (**Table 3.1**), respectively. The energy distance between S_1 and donor $^3\text{LE(D)}$ -state ($\Delta E_{1\text{CT-3LE(D)}}$) changed from slightly negative to almost isoenergetic value: -50, -20 meV to 30 meV, respectively. Moreover, in D-A-Pi exceptionally, the $^3\text{LE(A)}$ -state localized on acceptor became the lowest excited state and its energy should be very close to the ^3CT one. Within the context of three-

level model, one can expect that such a strong interaction of ^1CT and two virtually isoenergetic $^3\text{LE}/^3\text{CT}$ states in D-A-Pi would afford the most efficient rISC. Surprisingly, this is not the case at all as shown in **Table 3.1** and **Table 3.2**. D-A-CH₃ and D-A-MeO exhibited the k_{rISC} values of 1.33×10^6 and $1.10 \times 10^6 \text{ s}^{-1}$, respectively, whilst value for D-A-Pi was the lowest among the D-A-X materials. At this point we suggest that this is due to large value of $\Delta E_{1\text{CT}-3\text{CT}}$, $\Delta E_{1\text{CT}-3\text{LE(A)}}$ or both. Consequently, in D-A-CH₃, D-A-MeO, and D-A-Pi, the DF lifetime increased significantly compared with D-A-H: $\tau_{\text{DF}} = 5.18 \text{ }\mu\text{s}$, $6.20 \text{ }\mu\text{s}$, and $6.67 \text{ }\mu\text{s}$, respectively.

We then turned into exploring most likely mechanisms of spin-flip transitions. Namely, the correlations of energy gap reduction with the increase of $\ln(k_{\text{ISC}})$ and $\ln(k_{\text{rISC}})$ were analyzed. Such an inverse relationship was found between the $^3\text{LE(D)}-^1\text{CT}$ energy gap and ISC rate (**Figure 3.7a**). Interestingly, D-A-CN falls out of the latter dependence, probably due to the largest $\Delta E_{3\text{LE(D)}-1\text{CT}}$ value of 280 meV, which evidently exceeds thermal activation limit at room temperature. ISC rate does not correlate with the $\Delta E_{1\text{CT}-3\text{CT}}$ value (**Figure 3.7b**): emitters D-A-Pi, D-A-MeO, and D-A-Me with large differences in energy gaps show similar k_{ISC} , whilst D-A-CF₃ and D-A-CN with close $\Delta E_{1\text{CT}-3\text{CT}}$ have different k_{ISC} .

The rISC rate constant increases exponentially with the decrease of the $^1\text{CT}-^3\text{CT}$ energy gap (**Figure 3.7c**). Such observations indicate the key role of the $^3\text{CT}-^1\text{CT}$ transition for rISC and thus triplet harvesting in the investigated emitters. This evidences the dominating direct $^3\text{CT}-^1\text{CT}$ two-state mechanism for rISC in contrast to the $^1\text{CT}-^3\text{LE(D)}$ one for ISC, similarly to those found previously for *s*-triazine emitters.^[21] One can also observe an illusory correlation between the $^1\text{CT}-^3\text{LE(D)}$ energy gap and rISC rate (**Figure 3.7d**). In fact, this relationship has no physical sense, as it includes emitters with $\Delta E_{1\text{CT}-3\text{LE(D)}}$ close to or substantially above the thermal activation limit (D-A-D and D-A-CF₃, D-A-CN). As the $^3\text{LE(D)}$ energy was determined as a relatively constant value, such a dependence thus reflects the rise of rISC rate

with the stabilization of ^1CT and hence the decrease of $\Delta E_{3\text{CT}-1\text{CT}}$ as was reported previously.
[20]

From the point of view of the excited-states alignment, one can conclude that the described push-pull substituent approach enables fine gradual conversion of the lowest excited states from dominating ^3LE role with strong interaction of ^1CT and ^3LE states to strong CT character with negligible ^3LE role with increasing Hammett constant σ . As evidenced by the experimental results, ISC rate correlates with $\Delta E_{3\text{LE(D)}-1\text{CT}}$ while rISC rate correlates with $\Delta E_{1\text{CT}-3\text{CT}}$. Therefore, the rISC in TADF is better explained by the two-state model than the three-state model. Eventually, exciton dynamics could be rearranged and improved with the increasing $k_{\text{rISC}}/k_{\text{ISC}}$ ratio which is the key factor for shortening τ_{DF} (**Figure 3.4b**).

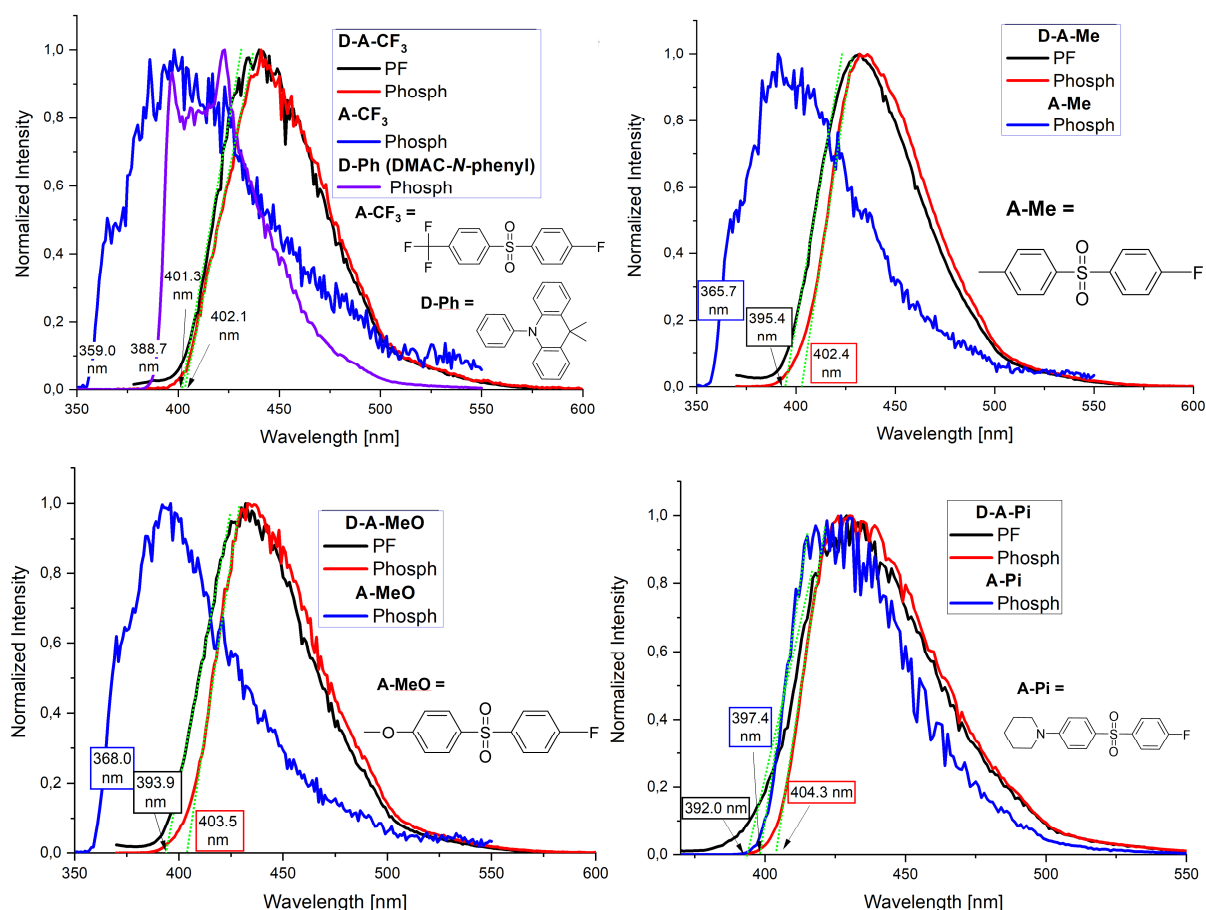


Figure 3.5 Prompt fluorescence (PF) and phosphorescence (50 ms delay time) spectra of selected emitters **D-A-X**, acceptor **A-X**, and donor (**D-Ph**) molecules in frozen toluene at 78 K.

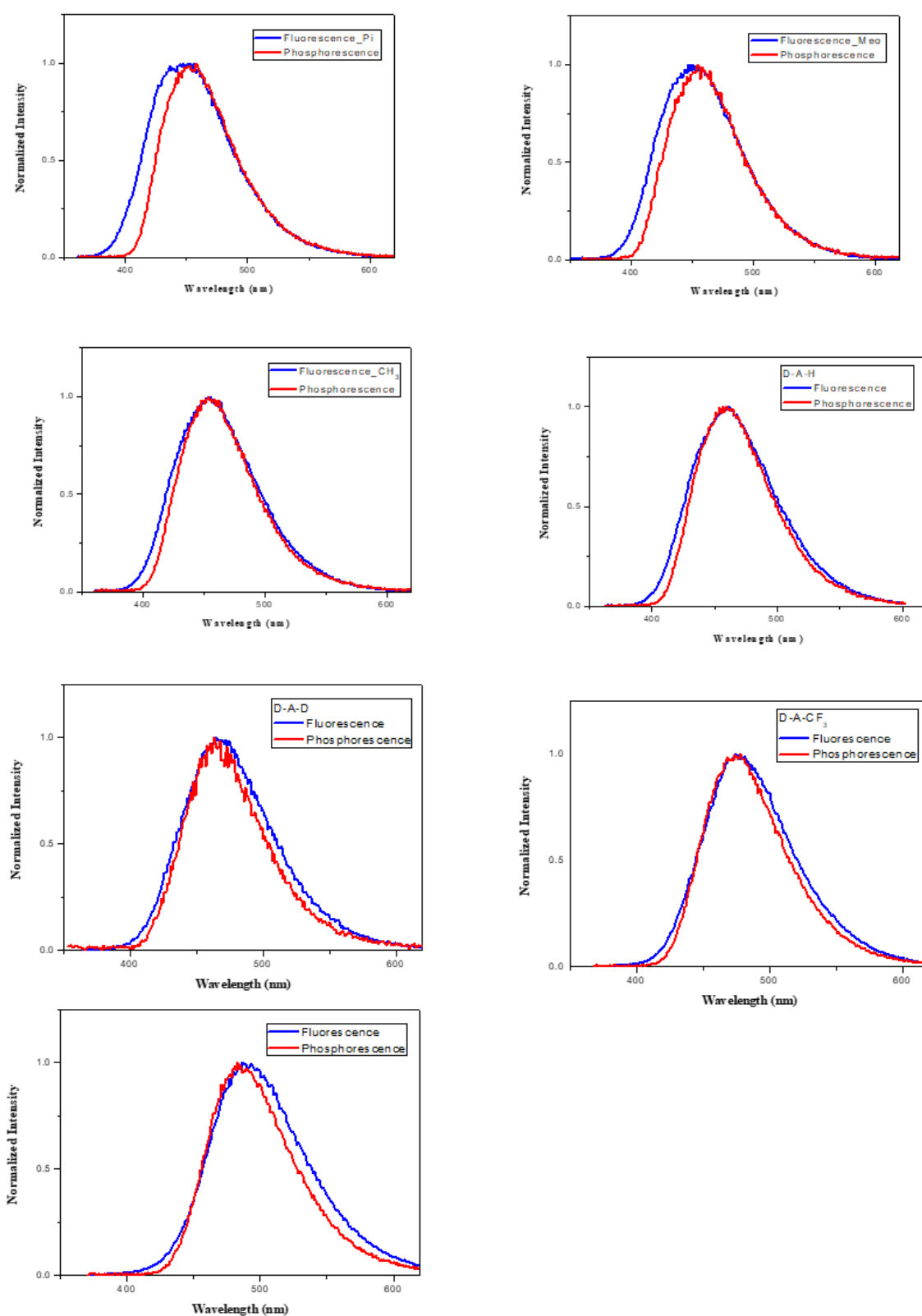


Figure 3.6 Fluorescence and phosphorescence spectra in 10 wt% DPEPO film

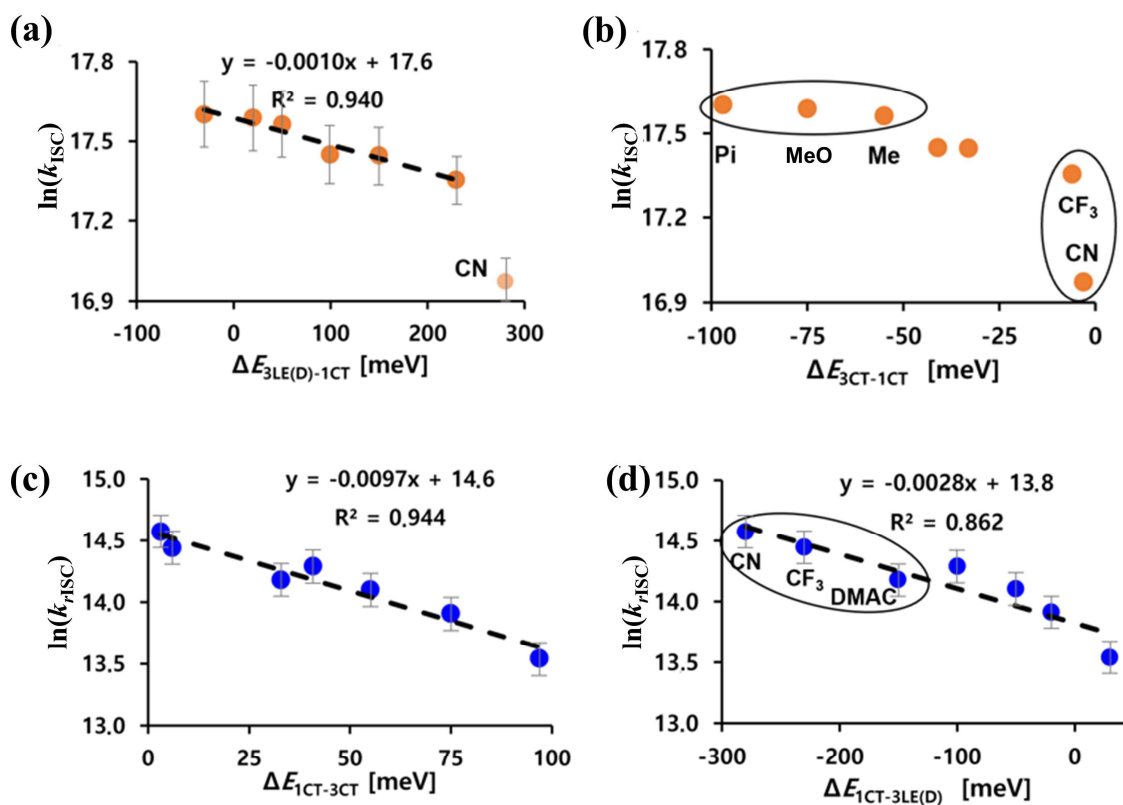


Figure 3.7 Correlations of the logarithm of ISC (a,b) and rISC (c,d) rate constants with the energy gaps

3.3.5 OLED Performances

To showcase possible OLEDs application of D-A-X TADF emitters, multi-layered OLED devices were fabricated comprising glass substrate/ITO (indium tin oxide) anode/MoO₃ (10 nm)/TCTA (30 nm)/mCP (10nm)/EML (20 nm)/DPEPO (10 nm)/TmPyPb (30 nm)/LiF (1 nm)/Al (100 nm). ITO, MoO₃, LiF, and Al were used as the anode, hole-injection layer, electron-injection layer and the cathode, respectively. Di-[4-(*N,N*-ditolyl-amino)-phenyl]-cyclohexane (TAPC) and 1,3,5-tri(*m*-pyrid-3-yl-phenyl) benzene (TmPyPB) were used as hole-transport layer (HTL) and electron-transport layer (ETL), respectively. Emitting layers (EML) incorporating 10%-D-A-X derivatives in 4,4'-*bis*(carbazol-9-yl) biphenyl (DPEPO) host were vacuum evaporated. The energy-level diagram of the devices and the molecular structure are shown in **Figure 3.8**.

The EQE versus luminance characteristics of the devices are shown in **Figure 3.9** and **Figure 3.10**, from which the detailed device parameters are extracted and summarized in **Table 3.3**. The devices were shown to have turn-on voltage of 3.8-4.2 V. Similar with the PL profiles, D-A-X devices present the structureless EL spectra ranging from deep blue (446 nm) to sky-blue (476 nm) emission, which demonstrates that the EL emissions are mainly generated from the emitter itself. The CIE color space exhibited (0.15, 0.11), (0.16, 0.14), (0.16, 0.15), (0.16,0.16), (0.16,0.19), (0.17,0.27) and (0.21,0.37) for the D-A-Pi, D-A-MeO, D-A-CH₃, D-A-H, D-A-D, D-A-CF₃ and D-A-CN based devices, respectively. Compared to the device of D-A-D, the device based on D-A-H exhibited blue-shift of the CIE color space from (0.16, 0.19) to (0.16, 0.16) due to hypsochromic shift of EL spectra and narrowed full width half maximum (FWHM). The introducing of electron-donating substituents on the X position caused hypsochromic shift of EL compared to D-A-H (λ_{\max} = 447 nm for D-A-Pi, 451 nm for D-A-MeO, and 456 nm for D-A-CH₃). On the other hand, the introducing of electron-

withdrawing substituents on the X position caused bathochromic shift of EL compared to D-A-H ($\lambda_{\text{max}} = 478$ nm for D-A-CF₃, and 489 nm for D-A-CN).

The maximum external quantum efficiency (EQE_{max}) values exhibited 17.2, 21.3, 21.2, 21.5, 22.6, 23.4 and 23.9% for the D-A-Pi, D-A-MeO, D-A-CH₃, D-A-H, D-A-D, D-A-CF₃ and D-A-CN, respectively. It suggests that triplet excitons are effectively utilized through the TADF mechanism in the device of D-A-X. Among the investigated blue emitters, D-A-CF₃ and D-A-CN devices showed relatively stable device performance. The external quantum efficiency was reduced by 9.0% (EQE_{max}=23.4% and EQE=21.3% at a luminance of 100 cd m⁻²) in D-A-CF₃ device, and it was reduced by 14.2% (EQE_{max}=23.9% and EQE=20.5% at a luminance of 100 cd m⁻²) in D-A-CN device. Because D-A-CF₃ and D-A-CN had increased $k_{\text{rISC}}/k_{\text{ISC}}$ ratio and short τ_{DF} , the triplet excitons could be effectively utilized compared to other devices. However, similar to many other reported blue TADF devices, EQE values of D-A-X devices decreased at luminance of 1000 cd m⁻² because triplet excitons were quenched by triplet–triplet annihilation (TTA) and singlet–triplet annihilation (STA) at high current density. [36,37] Compared with the reported DPS based TADF, we achieved superior device performance and improved color purity as shown in **Figure 3.9d** and **Table 3.4**.

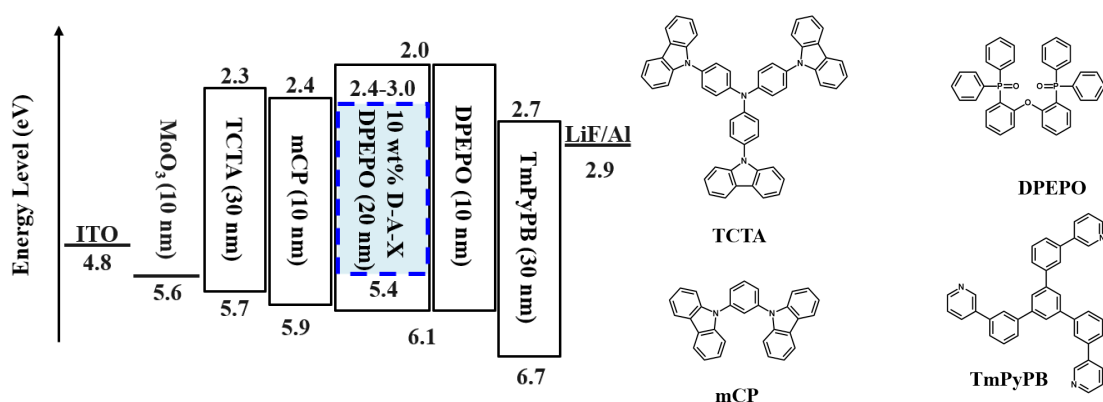


Figure 3.8 The energy-level diagram of the devices and the molecular structure of used materials

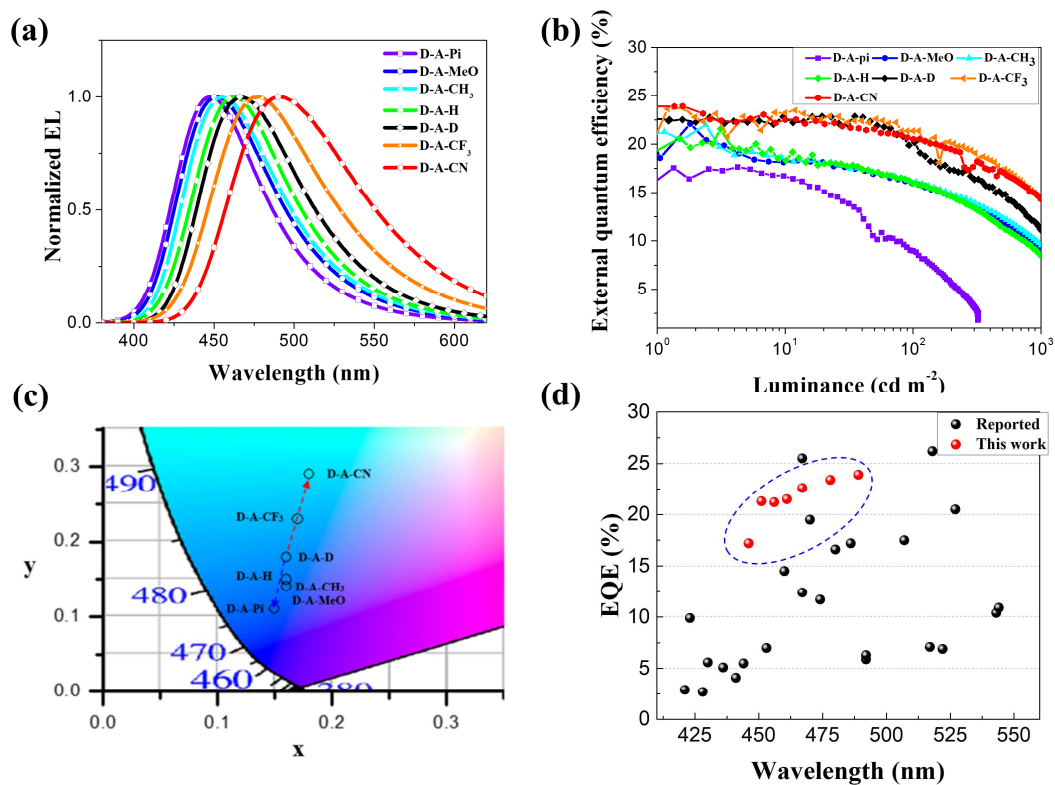


Figure 3.9 Device performance of D-A-X TADF materials. (a) EL spectra for OLEDs (b) external quantum efficiency (c) CIE coordinates of OLEDs using D-A-X emitters (d) performance of DPS based OLED

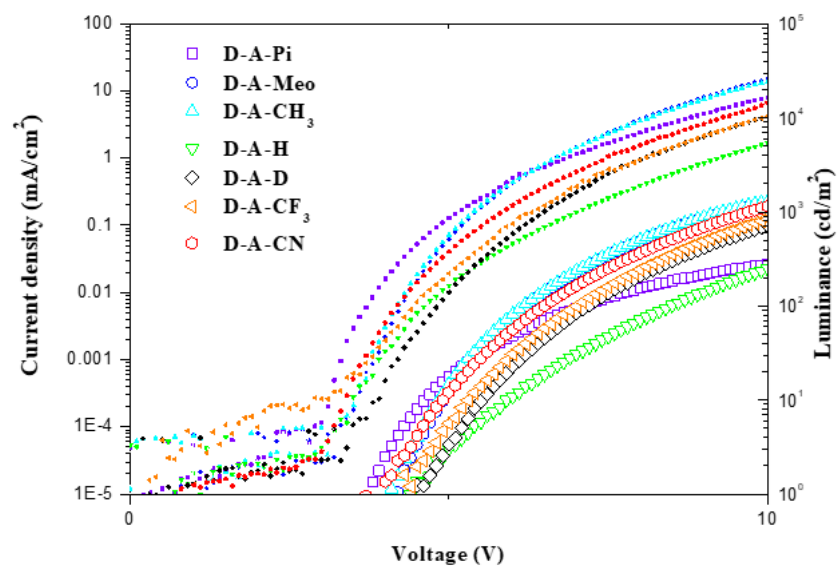


Figure 3.10 IVL characteristics of the devices

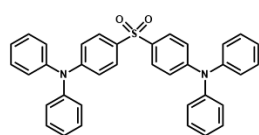
Table 3.3. Device performances of the D-A-X TADF-OLEDs.

	V_{on} ^{a)}	λ_{max} ^{b)}	FWHM	CIE ^{c)}	CE _{max} ^{d)}	PE _{max} ^{e)}	EQE ^{f)}	EQE _{100/1000} ^{g)}
	[V]	[nm]	[nm]	(x,y)	[cd A ⁻¹]	[lm W ⁻¹]	[%]	[%]
D-A-Pi	4.1	447	64	(0.15,0.11)	15.6	12.0	17.2	8.9/-
D-A-MeO	4.2	451	69	(0.16,0.14)	24.1	17.6	21.3	15.9/9.1
D-A-CH ₃	4.1	456	70	(0.16,0.15)	24.2	18.6	21.2	16.1/9.8
D-A-H	3.9	461	67	(0.16,0.16)	25.5	18.2	21.5	16.0/8.6
DMAC-DPS	4.0	467	75	(0.16,0.19)	29.1	14.3	22.6	20.2/11.2
D-A-CF ₃	3.8	478	80	(0.17,0.27)	30.6	23.8	23.4	21.3/14.4
D-A-CN	4.0	489	83	(0.18,0.37)	31.7	24.3	23.9	20.5/14.4

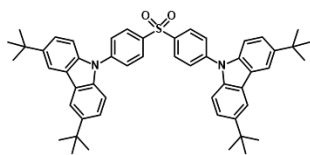
^{a)}turn-on voltage at 1 cd m⁻²; ^{b)}EL maximum wavelength; ^{c)}measured at 0.1 mA cm⁻²; ^{d)}maximum current efficiency; ^{e)}maximum power efficiency; ^{f)}maximum external quantum efficiency; ^{g)}external quantum efficiency at 100 and 1000 cd m⁻².

Table 3.4 Devices performances of DPS-based TADF emitters and their molecular structures

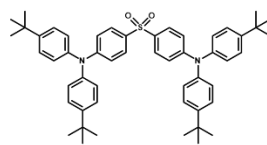
No.	Compounds	λ_{max} (nm)	EQE_{max}	CIE (x,y)	Ref
1	1	421	2.9	-	<i>J. Am. Chem. Soc.</i> 2012, 134, 14706–14709
2	3, DTC-DPS	423	9.9	(0.15,0.07)	<i>J. Am. Chem. Soc.</i> 2012, 134, 14706–14709
3	pDTCz-DPS	428	2.7	(0.15,0.08)	<i>J. Mater. Chem. C</i> , 2019, 7, 6664-6671
4	2	430	5.6	-	<i>J. Am. Chem. Soc.</i> 2012, 134, 14706–14709
5	D2-DPS	436	5.1	(0.15,0.07)	<i>Journal of Nanoscience and Nanotechnology</i> , 2019, 19, 4583
6	D1-DPS	441	4.1	(0.15,0.06)	<i>Journal of Nanoscience and Nanotechnology</i> , 2019, 19, 4583
7	DTC-mBPSB	444	5.5	0.15,0.08	<i>Chem. Commun.</i> , 2015,51, 16353-16356
8	pDTCz-3DPyS	453	7	(0.15,0.12)	<i>J. Mater. Chem. C</i> , 2019, 7, 6664-6671
9	DMOC-DPS	460	14.5	(0.16,0.16)	<i>J. Mater. Chem. C</i> , 2014, 2, 421-424
10	pDTCz-2DPyS	467	12.4	(0.15,0.19)	<i>J. Mater. Chem. C</i> , 2019, 7, 6664-6671
11	SBA-2DPS	467	25.5	(0.15,0.20)	<i>J. Mater. Chem. C</i> , 2019, 7, 10851-10859
12	DMAC-DPS	470	19.5	(0.16,0.20)	<i>Nature Photonics</i> , 2014, 8, 326
13	DTC-pDPSB	474	11.7	0.18,0.19	<i>Chem. Commun.</i> , 2015,51, 16353-16356
14	mSOAD	480	16.6	(0.18,0.30)	<i>Adv. Optical Mater.</i> 2018, 6, 1701256
15	m-ACSO2	486	17.2	(0.21,0.34)	<i>J. Phys. Chem. Lett.</i> 2018, 9, 1547–1553
16	o-ACSO2	492	5.9	(0.23,0.40)	<i>J. Phys. Chem. Lett.</i> 2018, 9, 1547–1553
17	4	492	6.3	(0.18,0.32)	<i>Journal of Luminescence</i> , 2019, 206, 250
18	PXZ-DPS	507	17.5	-	<i>Nature Photonics</i> , 2014, 8, 326
19	TPA-BPSP	517	7.1	(0.28,0.49)	<i>Adv. Optical Mater.</i> 2020, 8, 1901021
20	4,4-CzSPz	518	26.2	-	<i>J. Phys. Chem. C</i> 2019, 123, 1015–1020
21	3	522	6.9	(0.28,0.52)	<i>Journal of Luminescence</i> , 2019, 206, 250
22	MTPA-BPSP	527	20.5	(0.30,0.50)	<i>Adv. Optical Mater.</i> 2020, 8, 1901021
23	DMAc-BPSP	543	10.4	(0.27,0.47)	<i>Adv. Optical Mater.</i> 2020, 8, 1901021
24	MDMAc-BPSP	544	10.9	(0.25,0.44)	<i>Adv. Optical Mater.</i> 2020, 8, 1901021
25	PPZ-DPS	577	-	-	<i>Nature Photonics</i> , 2014, 8, 326



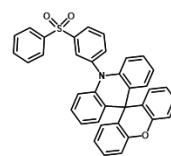
1 (1)



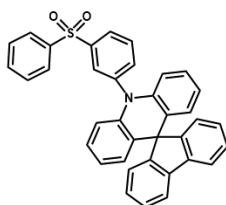
3 (2)
pDTCz-DPS (3)



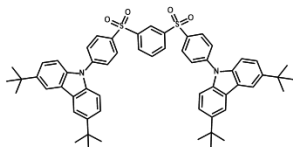
2 (4)



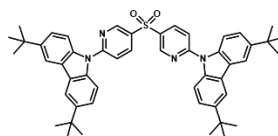
D2-DPS (5)



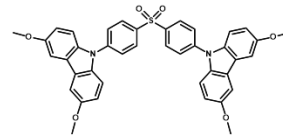
D1-DPS (6)



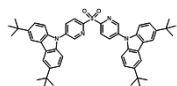
DTC-mBPSB (7)



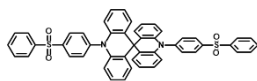
pDTCz-3DPyS (8)



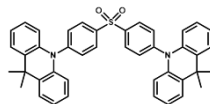
DMOC-DPS (9)



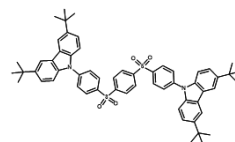
pDTCz-2DPyS (10)



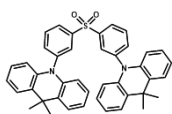
SBA-2DPS (11)



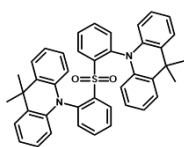
DMAC-DPS (12)



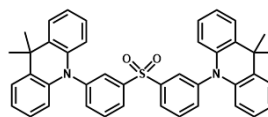
DTC-pDPSB (13)



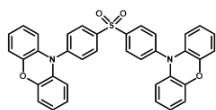
mSOAD (14)



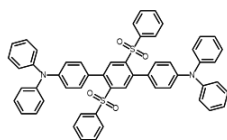
o-ACSO2 (16)



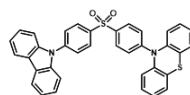
4 (17)



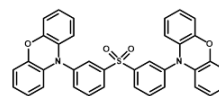
PXZ-DPS (18)



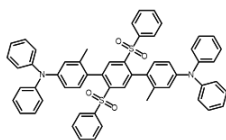
TPA-BPSP (19)



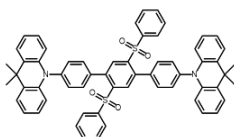
4,4-CzSPz (20)



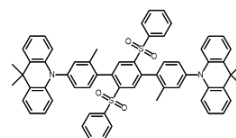
3 (21)



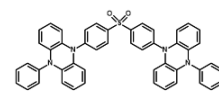
MTPA-BPSP (22)



DMAc-BPSP (23)



MDMAc-BPSP (24)



PPZ-DPS (25)

3.3.6 Theoretical studies on rISC rates and TADF model

The above discussed experimental data evidences that the investigated group of TADF emitters disobey the three-state model relying on the energetic closeness of ^3LE and $^1,^3\text{CT}$ states for achieving the highest rISC rates. In fact, gradual separation of the ^1CT and ^3LE states in the series of D-A-Pi, D-A-MeO, D-A-CH₃, D-A-H, D-A-DMAC, D-A-CF₃, D-A-CN rather results in the increase of k_{rISC} and $k_{\text{rISC}}/k_{\text{ISC}}$ values (**Figure 3.4b**). On the other hand, it is clearly noted that the energy gap between singlet and triplet CT states decreases in this row (**Figure 3.7c**), indicating that the energetic proximity of the $\Delta E_{1\text{CT}-3\text{CT}}$ is the key factor for rISC.

Recently, we have developed a two-state photophysical model which excellently explained TADF in a DMAC-TRZ emitter in various polarities thanks to the efficient direct $^1\text{CT} \leftrightarrow ^3\text{CT}$ interaction.^[20] We extend such a two-state model to explain the TADF peculiarities of D-A-X in DPEPO films. Physical background of this model is as follows:

1) Due to molecular motions, a macroscopic system (film or solution) should be represented as an ensemble of molecules in various geometries. The latter can be described as thermodynamically allowed deviations from the energy minimum at given temperature.

2) In solid films, rotations of large molecular fragments are rather restricted. When film is prepared by solution processed methods or evaporation, however, dihedral angles between such large fragments should immediately get fixed with their own thermal distribution resulting in the dispersion of fixed rotational angles. This means that each rotamer should be regarded as individual emitting species with its own electronic and photophysical properties. Particularly in our TADF emitters, the dihedral angle between the donor and acceptor fragments (θ) plays the key role and within the developed model remains the same as in the ground state. This provides a distribution of rotameric isomers of TADF emitter in doped film. The amount of each rotamer (p_θ) is defined by the Boltzmann distribution. Here, to simplify the model and necessary calculations, only rotamers with different θ values are considered.

3) During the structural relaxation after excitation, bond lengths and angles change to adjust to the excited electronic structure, whilst dihedral angles between large structural fragments remain the same as in the S_0 -state. The distribution of rotamers thus also remains the same as in the ground state. Within the excited rotamers with the same θ value, triplet-singlet transition is an adiabatic process and therefore can be described within the Born-Oppenheimer approximation. Its rate constant can be thus calculated using the Marcus-Hush equation. The developed approach thus explains the imaginary deviation of a macroscopic ensemble of emitter species from Born-Oppenheimer approximation focusing on the key molecular rotations which are responsible for the $^3\text{CT} \leftrightarrow ^1\text{CT}$ SOC enhancement. As the spin-flip rate is calculated after changes in the molecular structure occurred, the Born-Oppenheimer approximation remains valid even though it is not applicable for the emitter “frozen” in its optimal geometry.

4) The experimentally estimated values of excited-state energies and energy gaps are thus statistical sums of respective values for different rotamers. In the similar manner, contribution of each rotamer is added in the experimental rISC rate constant: $k_{\text{rISC}}(\text{exp}) = \chi_{3\text{CT}} \sum p_{\theta} k_{3\text{CT}-1\text{CT}}(\theta) + \chi_{3\text{LE}} \sum p_{\theta} k_{3\text{LE}-1\text{CT}}(\theta)$, where $\chi_{3\text{CT}}$ and $\chi_{3\text{LE}}$ are molar fractions of molecules in the ^3CT and ^3LE states, respectively, at 298 K calculated using Boltzmann distribution.

Following these considerations, **Figure 3.11** show the calculated distribution of rotamers with the same θ deviation: ± 5 stands for rotamers with the θ value of 85° and 95° , ± 10 means 80° and 100° rotamers and so on. It can be noticed that the amount of rotamers decreases with the increase of θ deviation, whilst the predicted probability for the optimal-geometry rotamer is less than 4%. Rotamer distribution is almost identical for all investigated emitters.

As for the alignment of excited states, DFT calculations support the conclusions made from experimental data discussed above (**Figure 3.12**). In all the emitters except for D-A-Pi,

within the computationally predicted three types of the lowest excited states, the closest ones to the ^1CT -state are the charge transfer ^3CT state (T_1) and the one localized on the donor fragment $^3\text{LE(D)}$ (T_2). In D-A-Pi, calculations predict that the second triplet state of close energy to the ^3CT is localized on the acceptor fragment ($^3\text{LE(A)}$), whilst $^3\text{LE(D)}$ is the third triplet state.

The dependences of energies of the key excited electronic states on the dihedral angle θ are depicted on the **Figure 3.13 a, b, c**. It can be noticed that such a θ -coordinate potential energy surfaces (θ -PES) of the ^1CT -state and LE triplet states localized on donor ($^3\text{LE(D)}$) and acceptor ($^3\text{LE(A)}$) states are very similar in all compounds, and exhibit symmetrical parabolic shape with one minimum at near $\theta = 90^\circ$. On the other hand, the shape of respective curve for the ^3CT state is dependent on the substituent (**Figure 3.13b**). In the D-A-Pi derivative bearing the weakest acceptor, there are two energy minima at the θ values of 71° and 111° in optimal geometry of the ^3CT state. This corresponds to a 29° deviation from orthogonal geometry. The stronger the acceptor fragment, the narrower the shape of θ -PES of ^3CT state. In D-A-MeO, the double-well θ -PES is still observed, but, in optimal geometry, the deviation from orthogonal geometry decreases to 22° . In D-A-CH₃, D-A-H, and D-A-DMAC, the energy minima of θ -PES of ^3CT state shift to $\theta = 90^\circ$, however their shape is still broader than that of the ^1CT one. In the strongest D-A systems, D-A-CF₃ and especially D-A-CN, the shapes of θ -PES of ^3CT and ^1CT states are almost identical.

Such a substituent-dependent difference in the CT states of different multiplicity has following important consequences for the ^3CT - ^1CT transition. In the ^3CT -state optimal geometry of emitters with weaker acceptors, the deviation from donor-acceptor orthogonality enables partial conjugation of donor and acceptor fragments and partial overlap of HOMO and LUMO. The ^3CT state is thus more stabilized than the ^1CT one, whose optimal geometry is orthogonal. In the result, with the decrease of acceptor strengths in the row D-A-CN, D-A-CF₃,

D-A-H, D-A-DMAC, D-A-MeO, D-A-Pi, the dependency of energy gap on the dihedral angle $\Delta E_{1CT-3CT}(\theta)$ becomes sharper (**Figure 3.13d**). The reorganization energy $\lambda_{1CT-3CT}$ also increases (**Figure 3.13e**). In the view of inhomogeneity of emitters in films, this means that with the decrease of acceptor strength, the probability of $^3CT-^1CT$ transition should decrease sharply for the rotamers with high deviation from orthogonal geometry. For a certain extent, this negative influence of the weaker acceptor strengths is compensated by the increase of SOC (**Figure 3.13f**): the maximal accessible $V_{1CT-3CT}$ value in D-A-CN of 0.11 cm^{-1} rises up to 0.29 cm^{-1} in D-A-Pi at $\theta = 60^\circ$. To analyze the quantitative impact of these factors on the spin-flip rate, the rISC rate constants were calculated using Marcus-Hush equation.

Figure 3.14a summarize the results of the developed theoretical model. The statistical sum of rate constants of $^3CT-^1CT$ transition and $^3LE-^1CT$ taking into account molar concentration of molecules in respective triplet states constants correlate well with the experimental rISC rate constants, which evidences the correctness of the developed model. According to the $k_{3CT-1CT}$ values, the rate of $^3CT-^1CT$ transition increases gradually with the increasing acceptor strengths. This has a key influence on the spin-flip dynamics in the case of emitters with fast rISC (D-A-CN, D-A-CF₃, D-A-H, and D-A-DMAC), where the population of the 3CT state is absolutely dominant. It should be emphasized, that according to the electronic features of rotamers with different θ value, similar θ -PES of 3CT and 1CT states providing low energy gap and reorganization energy are the reasons of high rISC rates. No less important is the existence of rotamers itself, because it provides non-zero SOC for the $^3CT-^1CT$ transition at deviation from $\theta = 90^\circ$.

Within the developed model, lower rISC rates of emitters with weakened acceptors are explained by a significant decrease of $^3CT-^1CT$ transition rate in spite of the growing role of the $^3LE-^1CT$ transitions which are supposed to improve TADF efficiency within the classic photophysical model (**Figure 3.14a**). In D-A-CH₃ and D-A-MeO, the statistical sums of both

$k_{3CT-1CT}(\theta)$ and $k_{3LE-1CT}(\theta)$ are almost equal, even though the portion of excited molecules in the 3LE -state does not exceed 1.6% and 2.5%, respectively (**Table 3.5**). In D-A-Pi, the population of excited molecules in three lowest triplet states of charge-transfer nature (3CT), localized on the acceptor ($^3LE(A)$), and donor ($^3LE(D)$) fragments is estimated as 45.5%, 51.1%, and 3.4%, respectively. The lowest value of $k_{3CT-1CT}$ among the investigated emitters is the result of the largest $^3CT-^1CT$ energy gap. In spite of high $^3LE(A)$ population and SOCME values of ca. 0.75 cm^{-1} , the $k_{3LE(A)-1CT}$ value does not exceed $1.4 \times 10^5\text{ s}^{-1}$. This is due to large reorganization energies $\lambda_{3LE(A)-1CT}$ exceeding 0.45 eV. On the other hand, the reorganization energy for the $^3LE(D)-^1CT$ transition is 0.1 eV lower. Together with low $\Delta E_{1CT-3LE(D)}$ energy gap this results in almost equal contributions of the $^3LE(D)-^1CT$ and $^3LE(A)-^1CT$, $^3CT-^1CT$ transitions to the rISC process in spite of much lower $^3LE(D)$ -state population.

The developed model enables analysis of the importance of various rotamers from the point of view of rISC efficiency. **Figures 3.14b** and **3.14c** represent the rISC rate constants in each rotamer via $^3CT-^1CT$ and $^3LE-^1CT$ mechanism, respectively, depending on the deviation of θ from the optimal value. Generally, in contrast to $k_{3LE-1CT}$, the $k_{3CT-1CT}$ values are strongly dependent on the dihedral angle θ because deviation from the optimal geometry leads to the increase of energy gap and reorganization energy of the $^3CT-^1CT$ transition. Exceptionally, in almost all rotamers of D-A-CN and D-A-CF₃, the rate of $^3CT-^1CT$ transition exceeds $1 \times 10^6\text{ s}^{-1}$, what makes it the only pathway of triplet-singlet conversion. In rotamers of D-A-DMAC and D-A-H with θ -deviation below 15° , rISC also occurs mainly via $^3CT-^1CT$ transition. In the rotamers with higher θ -deviation above 20° , the $k_{3CT-1CT}$ value decreases sharply due to growing $\Delta E_{1CT-3CT}$, and thus rISC can occur mainly via slow $^3LE-^1CT$ transition. Similar situation is observed in D-A-CH₃ and D-A-MeO, however in spite of high reorganization energy, the $^3LE-^1CT$ transition competes with the $^3CT-^1CT$ one even in the case of low θ -deviation within $\pm 4^\circ - \pm 15^\circ$.

In D-A-Pi, the ^3CT - ^1CT transition is realized only by the rotamers with the θ deviation close to $\pm 6^\circ$. The rest of rotamers deactivate via ^3LE - ^1CT transitions with large reorganization energies. Similar to other emitters, the rate of $^3\text{LE}(\text{D})$ - ^1CT transition in D-A-Pi is approximately constant for various rotamers due to weak dependence of $\lambda_{3\text{LE}(\text{D})-1\text{CT}}$ and SOCME values on θ . The distinguishing feature of D-A-Pi is low energy of $^3\text{LE}(\text{A})$ state and thus high population of excited molecules in this state. The rate of $^3\text{LE}(\text{A})$ - ^1CT transition however decreases sharply with the increase of θ -deviation, similarly to the ^3CT - ^1CT one. This means that dominant ^3CT and $^3\text{LE}(\text{A})$ triplet states of rotamers with the θ values of $<70^\circ$ and $>110^\circ$ have elongated lifetimes and nonradiative processes can effectively compete with rISC.

The above described feature of D-A-Pi is especially important when a large number of molecules are excited at the conditions of high density of excitation, or high current densities in an OLED device. In our opinion, accumulation of excited rotamers with high θ -deviation and low rISC rates is one of the main reasons of sharp efficiency roll-off under increase of current density observed for the OLED devices containing D-A-Pi (**Figure 3.9b**). On the other hand, high rate of ^3CT - ^1CT transition in all rotamers of D-A-CN and D-A-CF₃ is beneficial to short lifetime of triplet state independent of the rotamer conformation resulting in remarkably small efficiency roll-off (**Figure 3.9b**). Similar performance of the OLED containing D-A-DMAC with lower rISC rate indicates the importance of other factors, most probably individual electrochemical stability of emitter.

The investigations described above represent another successful implementation of the rotamer two-state TADF model. In general, the described approach emphasizes and explains the key importance of direct spin flip between ^1CT and ^3CT states for DA emitters including partly conjugated ones.^[38-40] It seems to be specifically important for the emitters with orthogonal DA structure in energetic minima like DMAC-DPS derivatives described here as well as systems bearing different or modified donor and acceptor fragments, because

the $^3\text{CT}-^1\text{CT}$ transition is usually neglected due to the El-Sayed rules.^[20,38] It should be noted that due to high sensitivity to the θ -rotation and taking into account the contribution of rotamers, the statistically weighted $^3\text{CT}-^1\text{CT}$ SOC is not zero. This is explained by the changes in the orbital momentum caused by increasing partial overlap of HOMO and LUMO due to deviations from the optimal θ -value. As was discussed in detail previously, the rotationally or vibronically activated $^3\text{CT}-^1\text{CT}$ mechanism of rISC can explain numerous deviations from the three-state model reported before.^[20] We thus should remember that the El-Sayed rules have limitations, especially in inhomogeneous media, and carefully analyze all possible spin-flip transitions to explain TADF in various molecular systems.

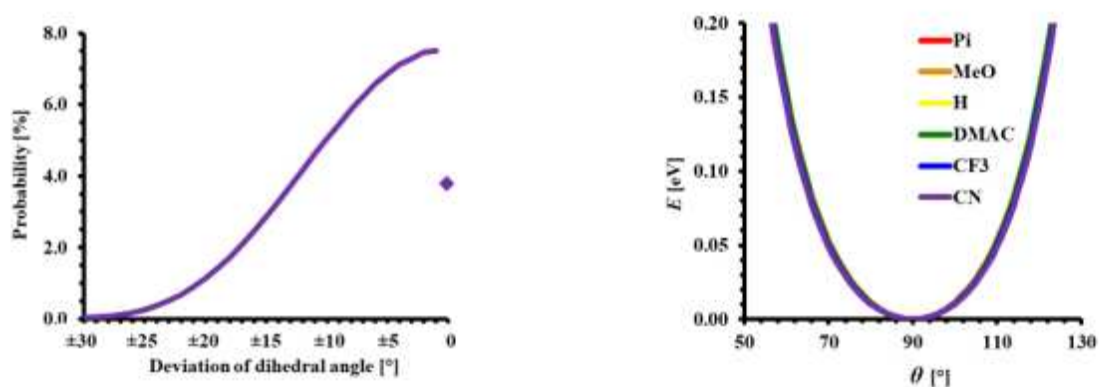


Figure 3.11 Probability of rotamers in S_0 -state and dependence of the S_0 -state energy on the dihedral angle θ .

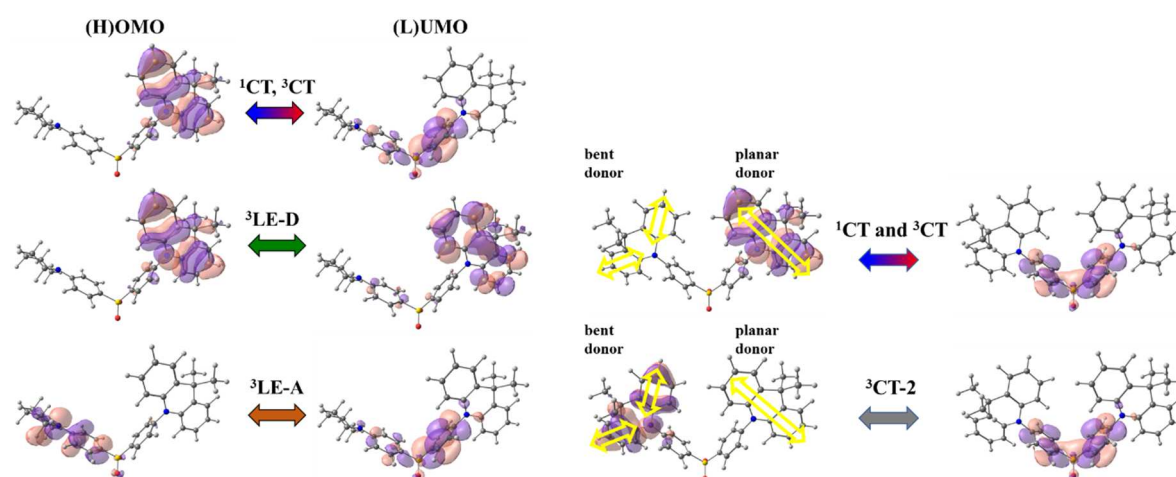


Figure 3.12 Molecular orbitals involved in the key electronic transitions on the example of DMAC-DPS-Pi (left) and diDMAC-DPS (right).

As D-A-DMAC has two donors, a second type of CT state (CT-2) was observed. In optimal geometries of all investigated states, the second DMAC fragment has bent structure and triplet $^3\text{CT-2}$ state has 0.215 eV higher energy compared to the ^3CT one.

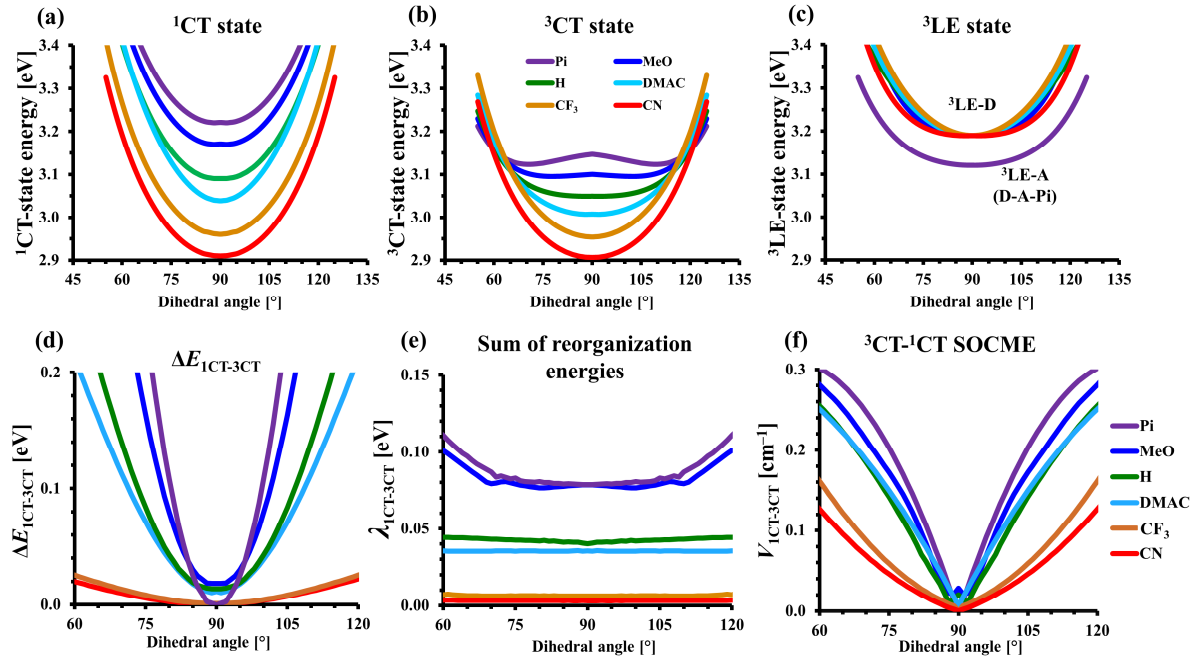


Figure 3.13 The dependences of energies of the lowest ex-cited electronic states (a, b, c), energy gaps (d), sum of reorganization energies (e), and SOCME constants (f) of $^3\text{CT}^1\text{CT}$ transition on the dihedral angle θ .

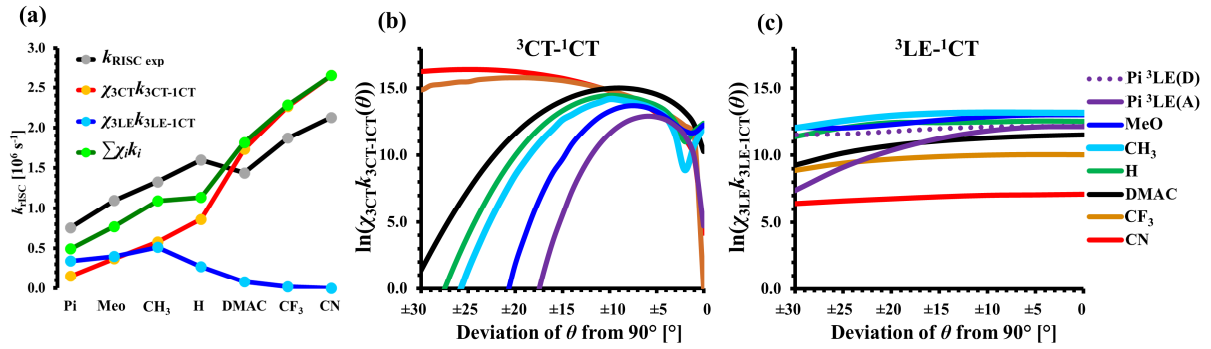


Figure 3.14 (a) Comparison of experimental rISC rate constants with the calculated ones of the $^3\text{CT}^1\text{CT}$ transition and the sum of rate constants of $^3\text{CT}^1\text{CT}$ and $^3\text{LE}^1\text{CT}$ transitions multiplied by molar concentration of molecules in respective triplet states. Represent the rISC rate constants in each rotamer via $^3\text{CT}^1\text{CT}$ (b) and $^3\text{LE}^1\text{CT}$ (c) mechanism, respectively, depending on the deviation of θ from the optimal value.

Table 3.5 Rate constants of triplet-singlet transitions

Cmpd	χ_{3CT} [%]	χ_{3LE} [%]	$\chi_{3CT}k_{3CT-1CT}$ [10^6 s^{-1}]	$\chi_{3LE}k_{3LE-1CT}$ [10^6 s^{-1}]	$\sum \chi_i k_i$ [10^6 s^{-1}]
D-A-Pi	45.5	51.1($^3\text{LE(A)}$) 3.4($^3\text{LE(D)}$)	0.15	0.14($^3\text{LE(A)}$) 0.18($^3\text{LE(D)}$)	0.47
D-A-MeO	97.6	2.4	0.37	0.40	0.77
D-A-CH₃	98.4	1.6	0.58	0.51	1.09
D-A-H	99.6	0.41	0.87	0.27	1.14
D-A-DMAC	99.9	0.081	1.73	0.08	1.81
D-A-CF₃	100.0	0.011	2.27	0.02	2.29
D-A-CN	100.0	0.002	2.65	0.00	2.65

* χ_{3CT} and χ_{3LE} – molar fraction of molecules in the ^3CT and ^3LE states, respectively, at 298K given by Boltzmann distribution using triplet energy values from Table 3.1.

3.4 Conclusion

A new series of D-A-X derivatives were designed and synthesized to explore a structure-property relationship for fine tuning energy states of TADF. Various substituents (X) modulated the electronic states associated with photophysical and electrochemical properties. Through such a controlled strength of ICT between D-A, the energies of ^1CT and ^3CT states were adjusted. On the other hand, the ^3LE state was less affected by substituents. As a result, D-A-X compounds showed emission with ranging of 446 nm (deep blue) to 487 nm (sky blue) with high PLQY. Particularly, it was confirmed that all materials showed short delayed fluorescence lifetimes below 7 μs and their k_{rISC} values were relatively high as compared to the blue-region TADF materials reported previously. The OLEDs based on these D-A-X TADF molecules offered high maximum EQEs of 17.2% – 23.9%. Particularly, D-A- CF_3 and D-A-CN devices showed relatively stable device performance among other D-A-X devices due to increased $k_{\text{rISC}}/k_{\text{ISC}}$ ratio and short τ_{DF} , which afforded suppression of STA and TTA by lowering the density of the triplet excitons.

In D-A- CF_3 and D-A-CN emitters with maximal rISC rates and EQE values, the key role of the ^3CT - ^1CT transition is revealed. Within the developed TADF model taking into account the distribution of rotational conformers of emitters in doped films, efficient conversion of triplet excitons to the singlet ones is explained by low energy gap and reorganization energy between the ^3CT and ^1CT states in all rotamers. The existence of rotamers itself is crucial because it enables reasonable SOC for the ^3CT - ^1CT transition. The contribution of the ^3LE - ^1CT transition increases together with the decrease of acceptor strength and ICT-strength in general. In the most blue shifted D-A-MeO and especially D-A-Pi, rotamers with high deviation from optimal geometry undergo rISC exclusively via ^3LE - ^1CT transitions, which is relatively slow due to high reorganization energy. This leads to the

decrease of TADF efficiency and, in our opinion, lower EQE and increased efficiency roll-off in OLED.

Our investigations reveal that for the design of efficient TADF-OLED emitters, the enhancement of the $^3\text{CT}-^1\text{CT}$ transition is as much important as that of $^3\text{LE}-^1\text{CT}$ one. For the fast-rISC deep-blue emitters both of these rISC mechanisms should be well optimized. In view of high inhomogeneity of rotational conformers in doped films, these requirements should be fulfilled not only for the emitter in optimal geometry, but also for its isomers trapped in non-equilibrium geometries during film preparation.

3.5 References

- [1] S. Hirata, Y. Sakai, K. Masui, H. Tanaka, S. Y. Lee, H. Nomura, N. Nakamura, M. Yasumatsu, H. Nakanotani, Q. S. Zhang, K. Shizu, H. Miyazaki, C. Adachi, *Nature Materials* **2015**, 14, 330-336.
- [2] H. Kaji, H. Suzuki, T. Fukushima, K. Shizu, K. Suzuki, S. Kubo, T. Komino, H. Oiwa, F. Suzuki, A. Wakamiya, Y. Murata, C. Adachi, *Nat Commun* **2015**, 6, 8476.
- [3] Q. S. Zhang, D. Tsang, H. Kuwabara, Y. Hatae, B. Li, T. Takahashi, S. Y. Lee, T. Yasuda, C. Adachi, *Adv. Mater.* **2015**, 27, 2096-2100.
- [4] M. N. BerberanSantos, J. M. M. Garcia, *J. Am. Chem. Soc.* **1996**, 118, 9391-9394.
- [5] A. Endo, M. Ogasawara, A. Takahashi, D. Yokoyama, Y. Kato, C. Adachi, *Adv. Mater.* **2009**, 21, 4802-4806.
- [6] A. Endo, K. Sato, K. Yoshimura, T. Kai, A. Kawada, H. Miyazaki, C. Adachi, *Appl. Phys. Lett.* **2011**, 98, 083302.
- [7] H. Uoyama, K. Goushi, K. Shizu, H. Nomura, C. Adachi, *Nature* **2012**, 492, 234-238.
- [8] Q. S. Zhang, H. Kuwabara, W. J. Potscavage, S. P. Huang, Y. Hatae, T. Shibata, C. Adachi, *J. Am. Chem. Soc.* **2014**, 136, 18070-18081.
- [9] F. B. Dias, J. Santos, D. R. Graves, P. Data, R. S. Nobuyasu, M. A. Fox, A. S. Batsanov, T. Palmeira, M. N. Berberan-Santos, M. R. Bryce, A. P. Monkman, *Adv. Sci.* **2016**, 3, 1600080.
- [10] R. S. Nobuyasu, Z. J. Ren, G. C. Griffiths, A. S. Batsanov, P. Data, S. K. Yan, A. P. Monkman, M. R. Bryce, F. B. Dias, *Adv. Optical Mater.* **2016**, 4, 597-607.
- [11] M. K. Etherington, J. Gibson, H. F. Higginbotham, T. J. Penfold, A. P. Monkman, *Nature Commun* **2016**, 7, 13680.
- [12] J. Gibson, A. P. Monkman, T. J. Penfold, *Chemphyschem* **2016**, 17, 2956-2961.

- [13] P. K. Samanta, D. Kim, V. Coropceanu, J. L. Bredas, *J. Am. Chem. Soc.* **2017**, 139, 4042-4051.
- [14] R. Braveenth, H. Lee, J. D. Park, K. J. Yang, S. J. Hwang, K. R. Naveen, R. Lampande, J. H. Kwon, *Adv. Funct. Mater.* **2021**, 31, 2105805.
- [15] X.-L. Chen, X.-D. Tao, Z. Wei, L. Meng, F.-L. Lin, D.-H. Zhang, Y.-Y. Jing, C.-Z. Lu, *ACS Appl. Mater. Interfaces* **2021**, 13, 46909-46918.
- [16] Z. Qiu, W. Xie, Z. Yang, J.-H. Tan, Z. Yuan, L. Xing, S. Ji, W.-C. Chen, Y. Huo, S.-j. Su, *Chemical Engineering Journal* **2021**, 415, 128949.
- [17] J.-L. He, F.-C. Kong, B. Sun, X.-J. Wang, Q.-S. Tian, J. Fan, L.-S. Liao, *Chemical Engineering Journal* **2021**, 424, 130470.
- [18] Y. Xiang, Y. Zhao, N. Xu, S. Gong, F. Ni, K. Wu, J. Luo, G. Xie, Z.-H. Lu, C. Yang, *J. Mater. Chem. C* **2017**, 5, 12204.
- [19] G. Kreiza, D. Berenis, D. Banevičius, S. Juršėnas, T. Javorskis, E. Orentas, K. Kazlauskas, *Chemical Engineering Journal* **2021**, 412, 128574.
- [20] I. E. Serdiuk, M. Monka, K. Kozakiewicz, B. Liberek, P. Bojarski, S. Y. Park, *J. Phys. Chem. B* **2021**, 125, 2696-2706.
- [21] M. Mońka, I. E. Serdiuk, K. Kozakiewicz, E. Hoffman, J. Szumilas, A. Kubicki, S. Y. Park, P. Bojarski, *J. Mater. Chem. C* **2022**, 10, 7925-7934.
- [22] I. S. Park, S. Y. Lee, C. Adachi, T. Yasuda, *Adv. Funct. Mater.* **2016**, 26, 1813-1821.
- [23] K. C. Pan, S. W. Li, Y. Y. Ho, Y. J. Shiu, W. L. Tsai, M. Jiao, W. K. Lee, C. C. Wu, C. L. Chung, T. Chatterjee, Y. S. Li, K. T. Wong, H. C. Hu, C. C. Chen, M. T. Lee, *Adv. Funct. Mater.* **2016**, 26, 7560-7571.
- [24] C. Li, A. K. Harrison, Y. Liu, Z. Zhao, F. B. Dias, C. Zeng, S. Yan, M. R. Bryce, Z. Ren, *Chemical Engineering Journal* **2022**, 435, 134924.

- [25] C. Y. Chan, L. S. Cui, J. U. Kim, H. Nakanotani, C. Adachi, *Adv. Funct. Mater.* **2018**, 28, 1706023.
- [26] Z. N. Li, W. B. Li, C. Keum, E. Archer, B. M. Zhao, A. M. Z. Slawin, W. Huang, M. C. Gather, I. D. W. Samuel, E. Zysman-Colman, *J. Phys. Chem. C* **2019**, 123, 24772-24785.
- [27] M. Yokoyama, K. Inada, Y. Tsuchiya, H. Nakanotani, C. Adachi, *Chem. Commun.* **2018**, 54, 8261-8264.
- [28] R. Komatsu, H. Sasabe, Y. Seino, K. Nakao, J. Kido, *J. Mater. Chem. C* **2016**, 4, 2274-2278.
- [29] F. Hundemer, L. G. von Reventlow, C. Leonhardt, M. Polamo, M. Nieger, S. M. Seifermann, A. Colsmann, S. Bräse, *Chemistryopen* **2019**, 8, 1413-1420.
- [30] Y. H. Lee, S. Park, J. Oh, S. J. Woo, A. Kumar, J. J. Kim, J. Jung, S. Yoo, M. H. Lee, *Adv. Optical Mater.* **2018**, 6, 1800385.
- [31] I. E. Serdiuk, C. H. Ryoo, K. Kozakiewicz, M. Mońka, B. Liberek, S. Y. Park, *J. Mater. Chem. C* **2020**, 8, 6052.
- [32] Q. S. Zhang, B. Li, S. P. Huang, H. Nomura, H. Tanaka, C. Adachi, *Nat. Photonics* **2014**, 8, 326-332.
- [33] L. P. Hammett, *J. Am. Chem. Soc.* **1937**, 59, 96-103.
- [34] C. Hansch, A. Leo, R. W. Taft, *Chem. Rev.* **1991**, 91, 165-195.
- [35] L. S. Zhan, Z. X. Chen, S. L. Gong, Y. P. Xiang, F. Ni, X. Zeng, G. H. Xie, C. L. Yang, *Angew. Chem. Int. Ed.* **2019**, 58, 17651-17655.
- [36] K. Masui, H. Nakanotani, C. Adachi, *Organic Electronics* **2013**, 14, 2721-2726.
- [37] Y. Zhang, S. R. Forrest, *Phys. Rev. Lett.* **2012**, 108, 267404.
- [38] M. Mońka, D. Grzywacz, E. Hoffman, V. Ievtukhov, K. Kozakiewicz, R. Rogowski, A. Kubicki, B. Liberek, P. Bojarski, I. E. Serdiuk, *J. Mater. Chem. C* **2022**, 10, 11719-11729.

- [39] E. W. Evans, Y. Olivier, Y. Puttisong, W. K. Myers, T. J. H. Hele, S. M. Menke, T. H. Thomas, D. Credgington, D. Beljonne, R. H. Friend, N. C. Greenham, *J. Phys. Chem. Lett.* **2018**, 9, 4053-4058.
- [40] D. Di, A. S. Romanov, L. Yang, J. M. Richter, J. P. H. Rivett, S. Jones, T. H. Thomas, M. Abdi Jalebi, R. H. Friend, M. Linnolahti, M. Bochmann, D. Credgington, *Science*. **2017**, 356, 159-163.

Chapter4. Design of deep Blue TADF Materials using CN Substituted sulfone units

4.1. Introduction

For the past two decades, organic light emitting diodes (OLEDs) have drawn tremendous attention for the next generation of displays.^[1-3] In the light emitting materials or OLEDs, phosphors are in the spotlight as high-efficiency OLED light emitting materials because it can boost the internal quantum efficiency (IQE) of electroluminescence up to 100%.^[4] Red and green emitting phosphors have been developed with good color purity and high quantum efficiency. However, In the blue region, it is not only difficult to implement a phosphor with high color purity, but also has a short lifespan due to the instability of the material, making it difficult to commercialize blue OLEDs.^[5-7]

Recently thermally activated delayed fluorescence (TADF) has attracted great attention from the field of organic light emitting diodes (OLEDs) because it can achieve 100% internal quantum efficiency (IQE) of electroluminescence through the reverse intersystem crossing (rISC) process in pure organic molecules.^[8-11] To realize efficient rISC, Adachi *et al.* first embodied a molecular design strategy by using intramolecular charge transfer (ICT) mechanism between bulky electron donor (D) and acceptor (A) units which spatially separate the highest occupied molecular orbital (HOMO) and lowest unoccupied molecular orbital (LUMO) to ensure minimized ΔE_{ST} .^[12-15]

Meanwhile, we recently established the novel structural approach to actively control the color wavelength maintaining TADF characteristics: D-A-X strategy. The DAX strategy firstly maintains the donor (D) and acceptor (A) units in the symmetric TADF emitters (D-A-

D type) to form the main ICT energy states and secondarily substitution is introduced on the opposite side to fine tune the energy state.^[16]

Our investigations reveal that the enhancement of the $^3\text{CT} \rightarrow ^1\text{CT}$ transition is important to design efficient TADF-OLED emitters. Among D-A-X materials, D-A-CN using strongest CN substituent unit exhibited short delayed life time ($\tau_{\text{DF}}=2.10 \mu$) and high rate constants of reverse intersystem crossing ($k_{\text{rISC}}=2.1 \times 10^6 \text{ s}^{-1}$), however the emission showed sky blue region (488 nm) due to increasing ICT strength.

Herein, we designed and synthesized the blue TADF material by using CN Substituted sulfone acceptor on DPS-CBZ showing UV emission.^[17] Systematically photophysical studies were carried out and also the fabrication and characterization of OLED devices were made to explore their potential in high efficiency blue OLED application.

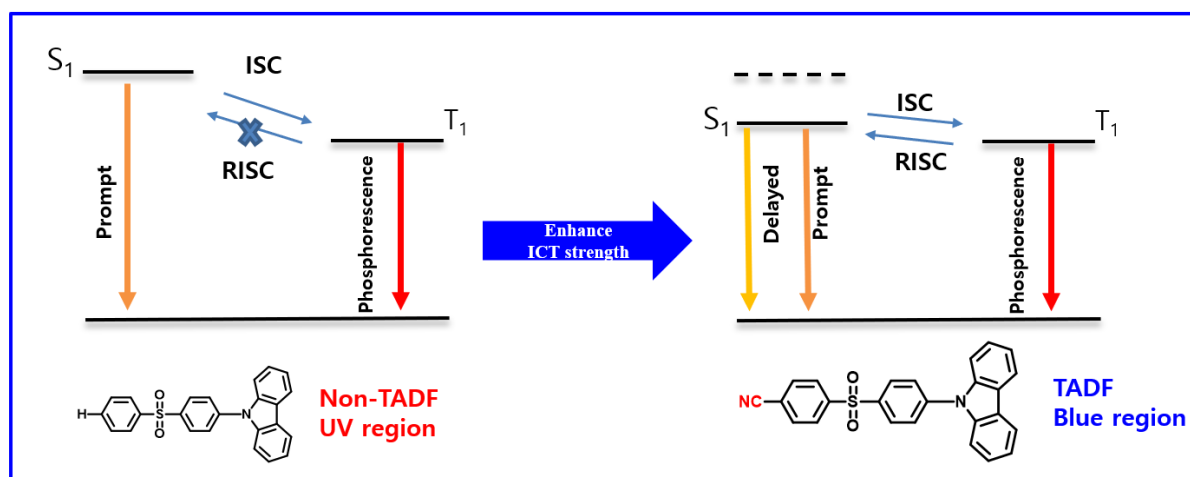
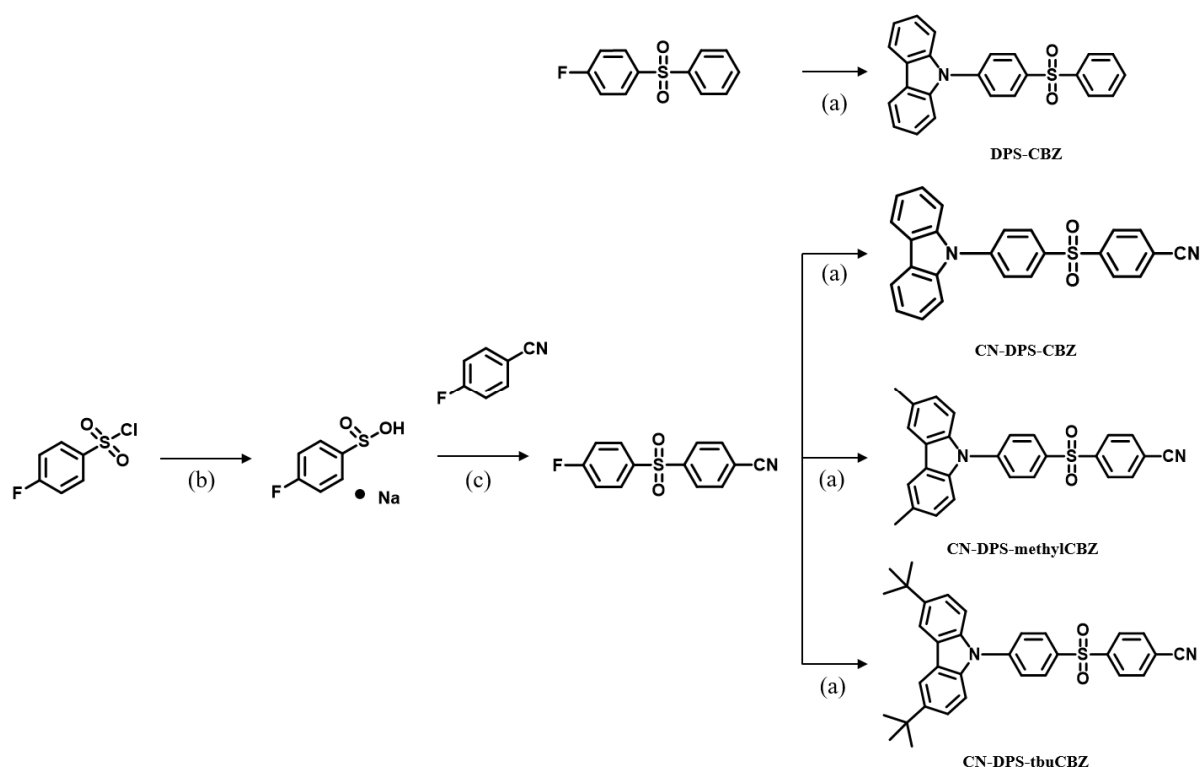


Figure 4.1 Structures of DPS-CBZ

4.2 Experimental Methods



Scheme 4.1 Synthetic routes of TADF materials. (a) Carbazole, NaH, anhydrous DMF, $55\text{ }^\circ\text{C}$
(b) NaSO_3 , NaHCO_3 , H_2O , $80\text{ }^\circ\text{C}$ (c) DMSO, $120\text{ }^\circ\text{C}$

4.2.1 Synthesis of Materials

All reagents were purchased from Sigma Aldrich, TCI, and Alfa Aesar. All experimental glassware was dried in an oven, and all experimental conditions were conducted in an argon or nitrogen environment. The target IDID material were synthesized through the following **scheme 4.1**.

4.2.2 Characterization

Chemical structures were identified by ^1H NMR (Bruker, ADVANCE-300 and ADVANCE-500), ^{13}C NMR (Bruker, Advance-500), high-resolution mass spectrometry (AB SCIEX, Q-

TOF 5600), and elemental analysis (Thermo Fisher Scientific, Flash 1112). UV-vis absorption spectra were recorded using a SHIMADZU UV-1650PC. Steady-state photoluminescence (PL) spectra were obtained with a PTI QuantaMaster 40 spectrofluorometer at room temperature and absolute PL quantum yields (PLQY) were recorded using a 3.2 inch integrating sphere. Low temperature photoluminescence spectra were measured using a Jasco FP-6500 at 77 K. Photoluminescence decay traces were obtained through the time correlated single photon counting (TCSPC) techniques by using a PicoQuant, FluoTime 250 instrument (PicoQuant, Germany). A 377 nm pulsed laser was used as an excitation source and temperature dependent studies were made with a cryostat (Oxford Instruments, Optistat DN). Data analyses were performed using exponential fitting models by FluoFit software. Cyclic voltammetry measurements were performed using a 273A (Princeton Applied Research). Each oxidation potential was calibrated using ferrocene as a reference. LUMO levels were evaluated from the HOMO level and the optical band gap which was obtained from the edge of the absorption spectra. DFT calculations were performed in the gas phase using Gaussian 09 quantum-chemical package. The geometry optimization for ground state of IDID derivatives was carried out using B3LYP functionals with 6-31G (d, p) basis set. TD-DFT calculations were performed using same functional and basis sets that were used.

4.2.3 Device fabrication and Measurement

The patterned ITO substrates were rinsed with acetone and isopropyl alcohol using sonication for 15 min, followed by 15 min UV-ozone-treatment. Organic layers, MoO₃ and Al were thermally evaporated at a deposition rate of 0.6–1 Å s⁻¹ for organic layers, 0.2 Å s⁻¹ for MoO₃, and 4–5 Å s⁻¹ for Al electrode. The current–voltage–luminance (I–V–L) characteristics of the devices were measured with a Keithley-236 source-measure unit, a Keithley-2000 multimeter

unit, and a calibrated Si photodiode (Hamamatsu S5227-1010BQ). The luminance and efficiencies were calculated from the photocurrent measurement data obtained with the Si photodiode. The electroluminescence spectra were obtained by using a spectroradiometer (CS-2000).

4.3 Results and Discussion

4.3.1 Density Functional Theory Calculations

The optimized geometry and electronic properties of target materials were calculated by density functional theory (DFT) and time-dependent DFT (TD-DFT) using the B3LYP functional and the 6-31G** basis set (Figure 1 and Figure S2). In the optimized ground state geometry, all the IDID derivatives showed twisted conformation with dihedral angle of around 40° between the CBZ donor and the DPS acceptor (Figure S2). As was expected, HOMO is located on donor and phenyl units, while LUMO is extended acceptor units (Figure 1). Thus, not only the spatial separation of HOMO and LUMO but also the modest orbital overlap could be achieved at the same time successfully addressing the trade-off between ΔE_{ST} and oscillation strength. With increasing ICT strength, it was calculated that the bandgap (3.27- 4.07 eV) and ΔE_{ST} (0.16 ~ 0.41 eV) were decreased with increasing ICT strength as shown in Figure 1.

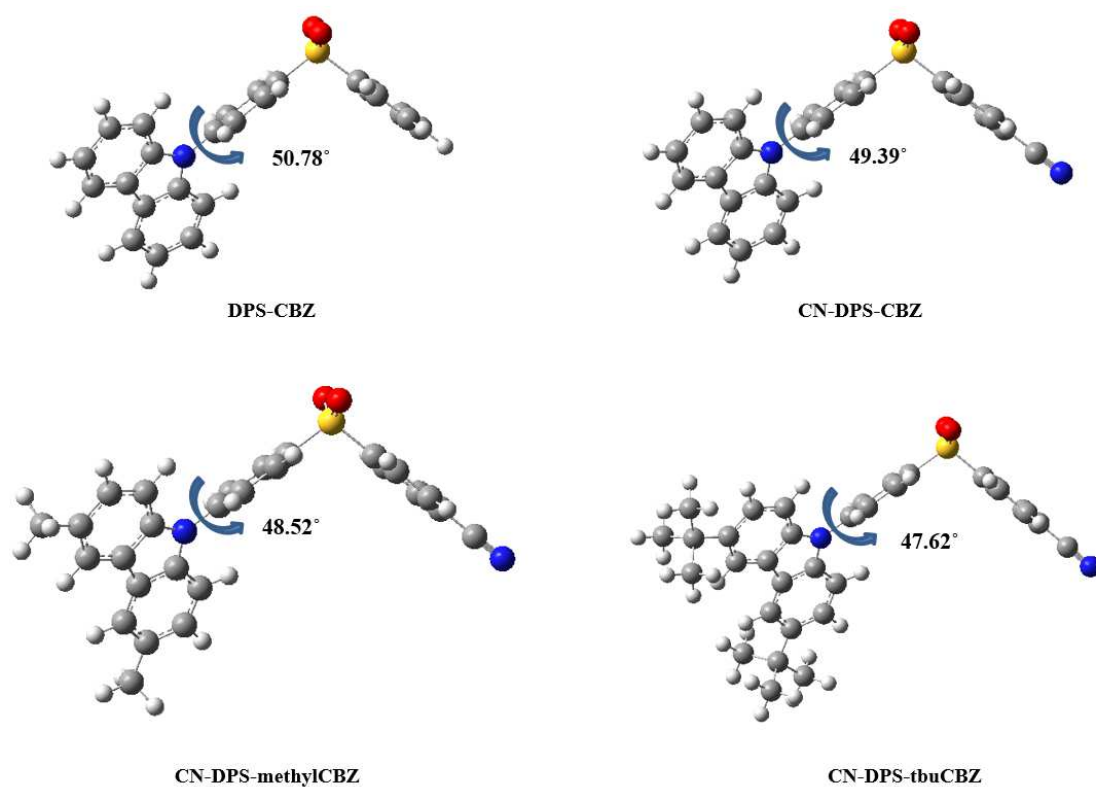


Figure 4.2 Optimized molecular geometries and the dihedral angle.

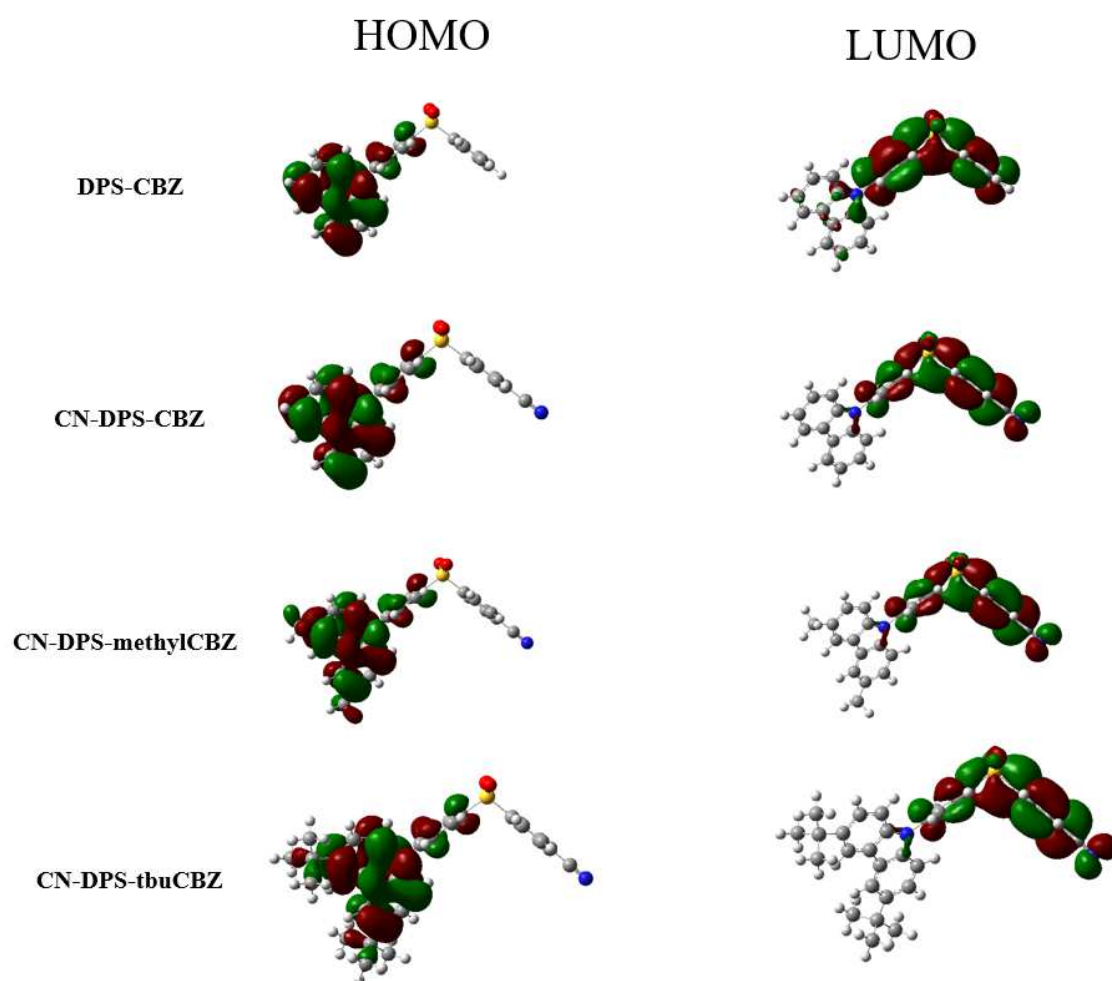


Figure 4.3 Optimized molecular geometries with HOMO and LUMO.

Table 4.1 Cyclic voltammetry of target materials.

	E_g (eV)	HOMO (eV)	LUMO (eV)	ΔE_{ST} (eV)
DPS-CBZ	4.07	-5.63	-1.56	0.41
CN-DPS-CBZ	3.45	-5.78	-2.33	0.19
CN-DPS-methylCBZ	3.29	-5.58	-2.29	0.16
CN-DPS-tbuCBZ	3.27	-5.56	-2.28	0.16

4.3.2 Electrochemical Properties

In order to evaluate the energy level of these compounds, cyclic voltammetry (CV) was carried out in methylene chloride solution using ferrocene as a reference (**Figure 4.4**). DPS-CBZ, CN-DPS-CBZ, CN-DPS-methylCBZ and CN-DPS-tbuCBZ exhibited HOMO levels of -5.62, -5.61, -5.58 and -5.59 eV, respectively. The LUMO level of a material was obtained by adding the optical bandgap to the HOMO level, and were calculated as -2.24, -2.40, -2.48 and -2.52 eV, respectively. The band gaps are 3.38, 3.21, 3.10 and 3.07 eV, respectively.

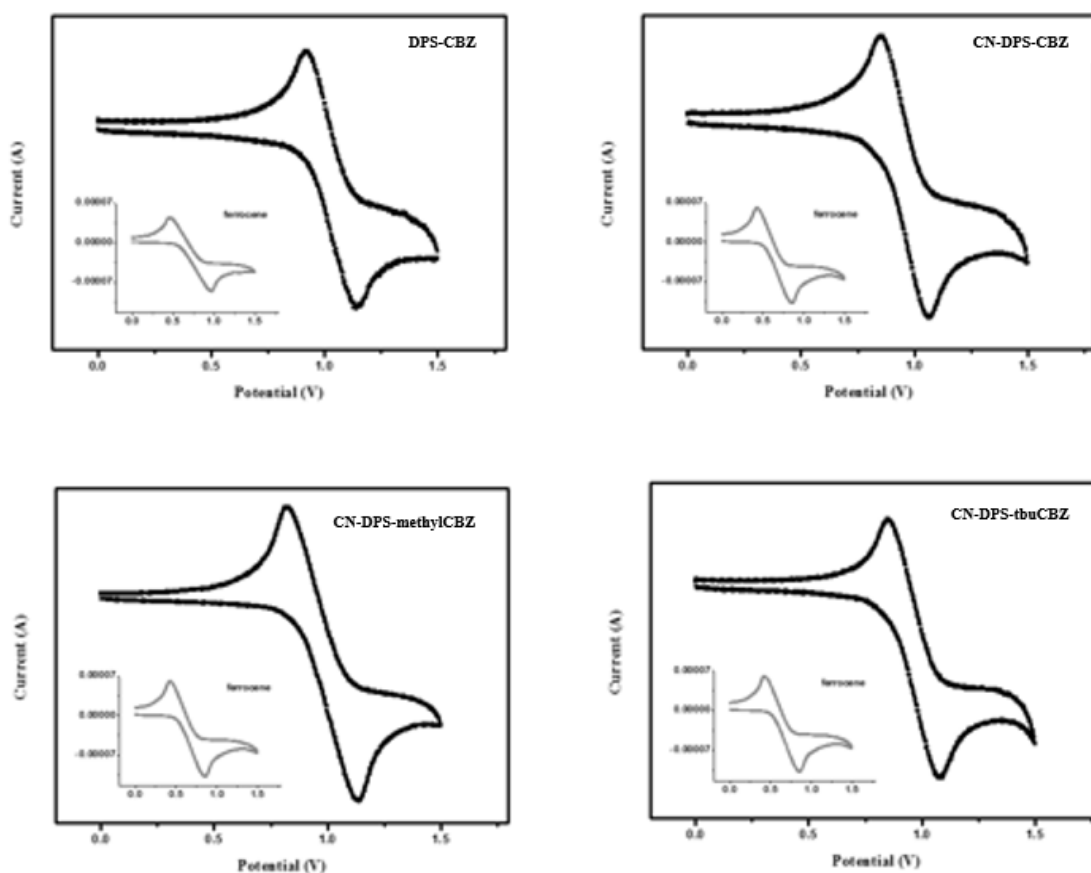


Figure 4.4 Cyclic voltammetry of target materials.

Table 4.2 Cyclic voltammetry of target materials.

	E_g^{opt} (eV)	$E_{HOMO,sol.}(eV)^a)$	$E_{LUMO,sol.}(eV)^b)$
DPS-CBZ	3.38	-5.62	-2.24
CN-DPS-CBZ	3.21	-5.61	-2.40
CN-DPS-methylCBZ	3.10	-5.58	-2.48
CN-DPS-tbuCBZ	3.07	-5.59	-2.52

a) HOMO level was determined by cyclic voltammetry in 5×10^{-3} M methylene chloride solution using ferrocene as a reference.

b) LUMO levels were evaluated with the HOMO level and the optical band gap obtained from the edge of the absorption spectra.

4.3.3 Photophysical Properties

Photophysical properties of target molecules were evaluated by UV-visible absorption (UV-vis) and photoluminescence emission (PL) spectra. (**Figure 4.5**, **Figure 4.6** and **Table 4.3**). It is shown in **Figure 4.5** that DPS-CBZ has the lowest absorption band by the π - π^* transition at 338 nm with absorption coefficient (ϵ) of $1475 \text{ M}^{-1}\text{cm}^{-1}$. On the other hand, all the other molecules showed gradually red-shifted absorption band with increasing ICT strength. CN-DPS-CBZ, CN-DPS-methylCBZ and CN-DPS-tbuCBZ exhibited maximum absorption band at 339 nm (ϵ of $1340 \text{ M}^{-1}\text{cm}^{-1}$), 351 nm (ϵ of $1400 \text{ M}^{-1}\text{cm}^{-1}$) and 355 nm (ϵ of $1270 \text{ M}^{-1}\text{cm}^{-1}$), respectively. The band gaps are 3.38, 3.21, 3.10 and 3.07 eV, respectively.

In toluene solutions, the PL spectra of target compounds showed broad ICT emission with a maximum ranging from 386 nm to 441 nm (deep blue) (**Figures 4.5**). DPS-CBZ exhibited UV ($\lambda_{\text{PL,max}}=386 \text{ nm}$) fluorescence emission with 52 nm of FWHM. CN-DPS-CBZ, which introducing the electron-withdrawing CN unit on DPS acceptor, showed bathochromic shift of photoluminescence ($\lambda_{\text{PL,max}}=415 \text{ nm}$) compared to DPS-CBZ. Such a behavior was caused by increasing electron-accepting power of the diphenylsulfone (DPS), resulting in increasing ICT strength and thus stabilized the ^1CT -state energy. Additionally, the electron-releasing substituents on carbazole caused bathochromic shift of PL compared to CN-DPS-CBZ ($\lambda_{\text{PL,max}} = 439 \text{ nm}$ for CN-DPS-methylCBZ and 441 nm for CN-DPS-tbuCBZ) due to electron-releasing units enhancing the donating power of carbazole units.

The emission spectra of these compounds in 6 wt% PMMA film also showed emission wavelength like in solution state. DPS-CBZ, CN-DPS-CBZ, CN-DPS-methylCBZ and CN-DPS-tbuCBZ exhibited maximum emission wavelength at 394 nm (FWHM of 58 nm), 425 nm

(FWHM of 75 nm), 445 nm (FWHM of 85 nm) and 447 nm (FWHM of 88 nm), respectively. The values of PL quantum yields (PLQYs, Φ_{PL}) are 0.75, 0.72, 0.82 and 0.81, respectively.

The transient decay lifetime measurement was carried out to explore different emission components of the target molecules using the Time Correlated Single Photon Counting (TCSPC) technique in 10 wt% DPEPO film (**Figure 4.8**). Notably, decay profiles of all compounds consisted not only of the prompt fluorescence (PF) but also of the delayed fluorescence (DF). The delayed fluorescence lifetime (τ_{DF}) of CN-DPS-CBZ, CN-DPS-methylCBZ and CN-DPS-tbuCBZ were measured to be 46.7, 28.6 and 26.0 μs , respectively (**Table 2**).

We further analyzed the exciton dynamics of the S_1 and T_1 states on the basis of their photophysical transition rates. The rate constants of radiative process were obtained from PLQY and PF lifetime data (**Table 4.4**); CN-DPS-CBZ exhibited rate constant of reverse intersystem crossing (k_{RISC}) $0.80 \times 10^5 \text{ s}^{-1}$. On the other hand, CN-DPS-methylCBZ and CN-DPS-tbuCBZ exhibited higher rate constant of reverse intersystem crossing (k_{RISC}) 1.4×10^5 and $1.7 \times 10^5 \text{ s}^{-1}$, respectively. Efficient triplet up-conversion could be occurred owing to small ΔE_{ST} .

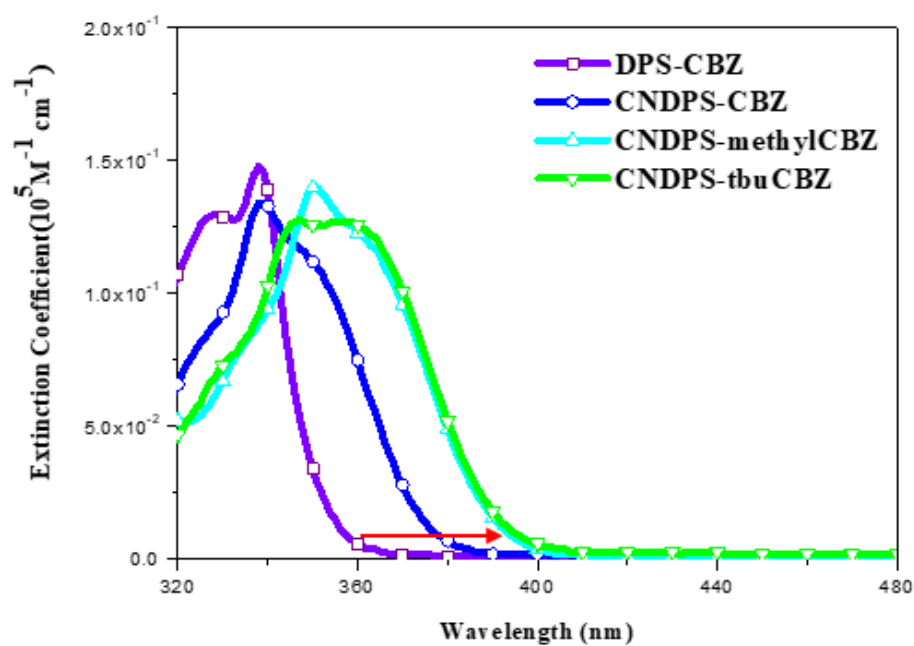


Figure 4.5 Absorption spectra of target molecules. (toluene, $c=1 \times 10^{-5} \text{M}$)

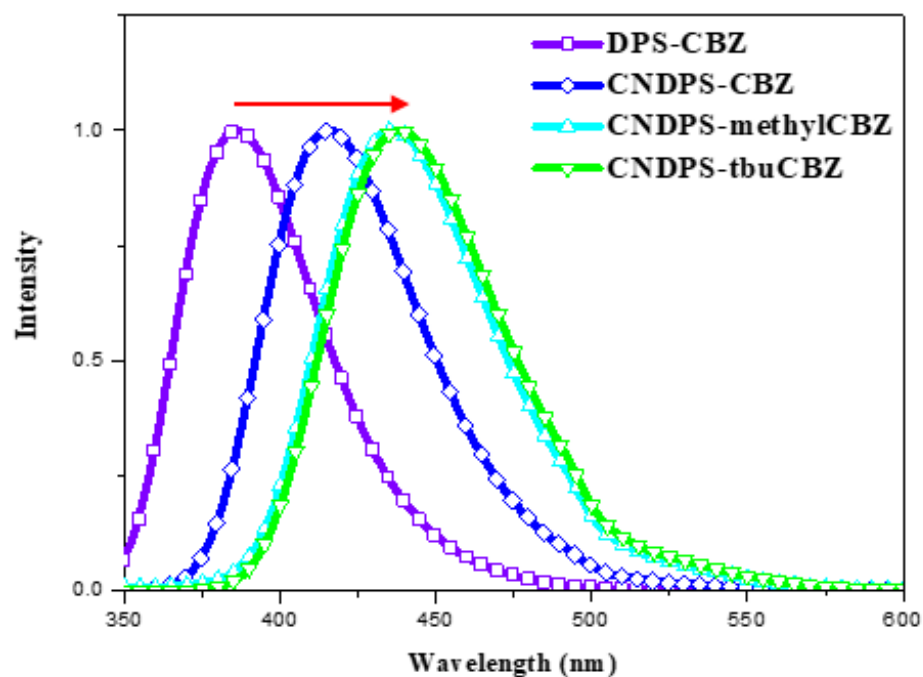


Figure 4.6 Normalized photoluminescence spectra of target molecules.

(toluene, $c=1 \times 10^{-5} \text{M}$)

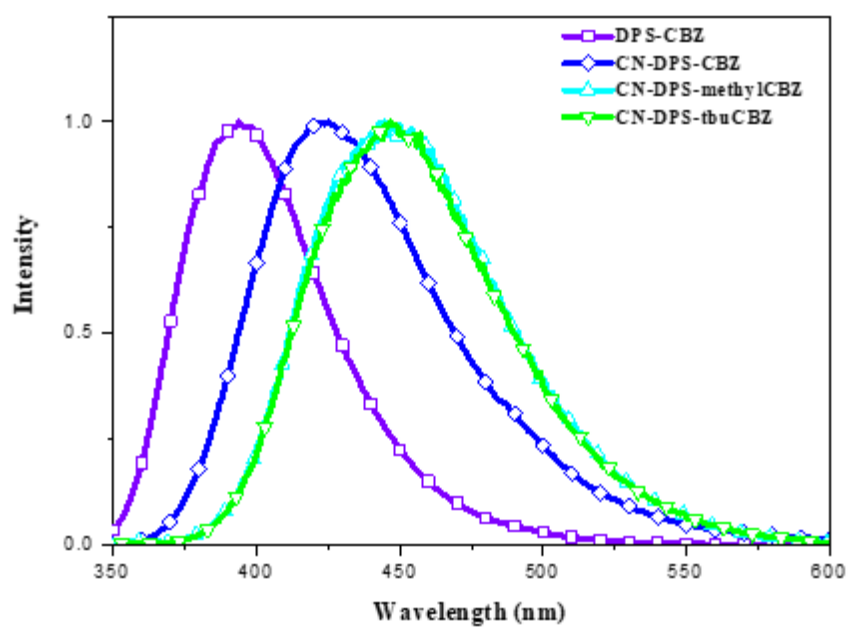


Figure 4.7 Normalized photoluminescence spectra of target molecules.

(10 wt% in DPEPO film)

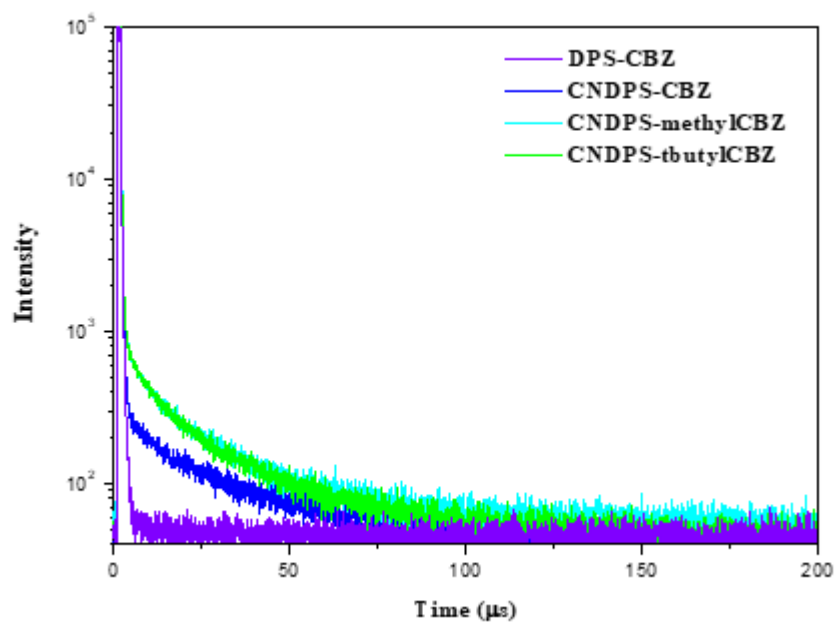


Figure 4.8 Temperature-dependent PL decay spectra (10 wt% in PMMA film)

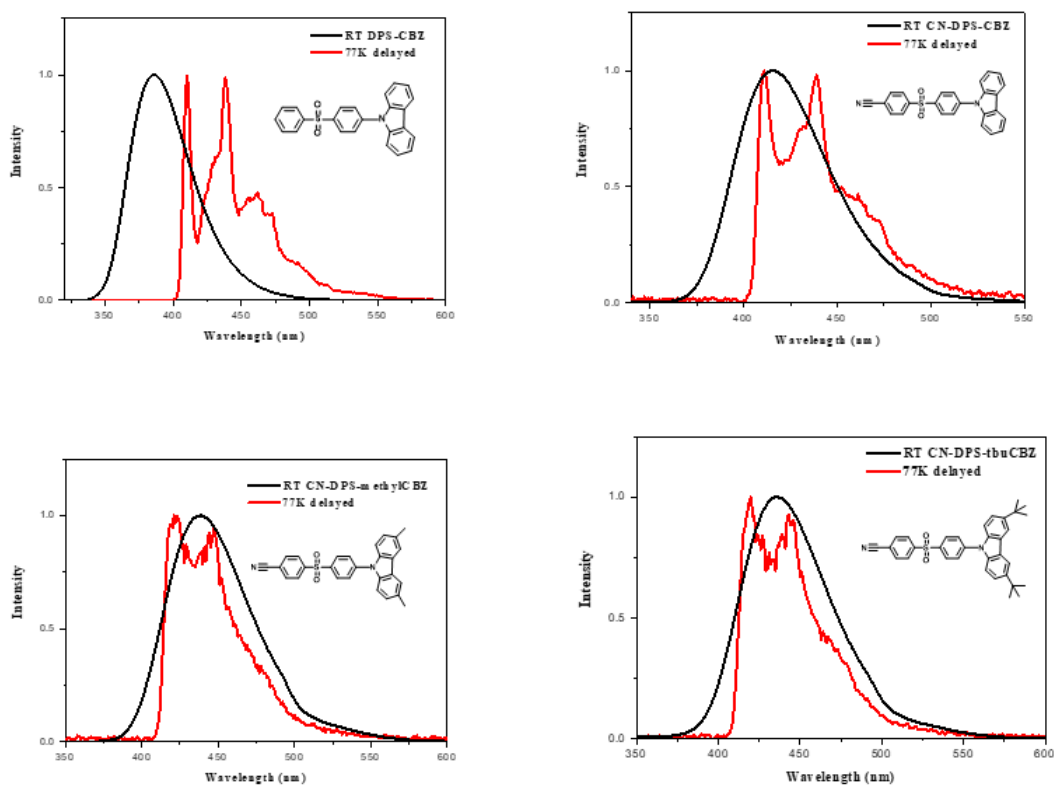


Figure 4.9 Fluorescence and phosphorescence spectra (toluene, $c=1 \times 10^{-5} \text{M}$)

Table 4.3 The summary of physical and photophysical properties of TADF materials.

	$\lambda_{\text{abs,max}}^{\text{a)}$ [nm]	$\epsilon^{\text{a)}$ [$\text{M}^{-1}\text{cm}^{-1}$]	Band gap [eV]	$\lambda_{\text{PL,max}}^{\text{b)/c)}$ [nm]	FWHM [nm]	$\Phi_{\text{ab}}^{\text{d)/e)/}$ [%]	$\Delta E_{\text{ST}}^{\text{i)}$ [eV]
DPS-CBZ	338	1480	3.38	386/394	52/58	66/75	0.53
CN-DPS-CBZ	339	1340	3.21	415/425	58/75	67/78	0.38
CN-DPS-methylCBZ	351	1400	3.10	439/445	63/85	67/82	0.24

CN-DPS- tbuCBZ	355	1270	3.07	441/447	64/88	69/81	0.22
-------------------	------------	------	------	----------------	--------------	--------------	------

^{a)} UV-vis absorption and PL spectra measured in 1×10^{-5} M toluene solution. ^{b,c)} PL spectra measured in 1×10^{-5} M toluene solution and 10 wt% PMMA doping films. ^{d,e)} Absolute PL quantum yields recorded in degassed 1×10^{-5} M toluene solution and 10 wt% PMMA doping films using an integrating sphere. ⁱ⁾ Energy gap between S_1 and T_1 estimated from the fluorescence and the phosphorescence spectra in 1×10^{-5} M toluene solution.

Table 4.4 The summary of rate constants in DPEPO films.

	$\tau_{PF}^{a)}$	$\tau_{DF}^{a)}$	$\Phi_{PF}^{b)}$	$\Phi_{DF}^{b)}$	k_r	k_{nr}	k_{ISC}	k_{rISC}
	[ns]	[μ s]	[%]	[%]	[10^6 s^{-1}]	[10^6 s^{-1}]	[10^6 s^{-1}]	[10^6 s^{-1}]
DPS-CBZ	19.5	-	75.0	-	38.5	12.82	-	-
CN-DPS- CBZ	18.7	46.7	26.6	45.4	14.3	8.13	31.1	0.08
CN-DPS- methylCBZ	19.2	28.6	20.5	61.5	10.7	2.34	39.1	0.14
CN-DPS- tbuCBZ	18.5	26.0	18.6	62.4	10.1	2.36	41.6	0.17

^{a)}Lifetime calculated from the prompt (τ_{PF}) and delayed (τ_{DF}) fluorescence decay in DPEPO 10 wt% doping films; ^{b)} Φ_{PF} (the prompt PLQY) and Φ_{DF} (the delayed PLQY) were obtained from the prompt and delayed proportions in transient decay curves of 10 wt% DPEPO doping films; k_r , k_{nr} – the rate constant of radiative and nonradiative decay of singlet excited state; k_{ISC} , k_{rISC} – rate constant of intersystem crossing and reverse intersystem crossing.

4.3.4 OLED Performances

To examine the possible OLEDs application, CN-DPS-CBZ, CN-DPS-methylCBZ and CN-DPS-tbuCBZ were selected due to their high PLQY and TADF characteristics. Multi-layered OLED devices were fabricated comprising glass substrate/ITO (indium tin oxide) anode/MoO₃ (10 nm)/TCTA (30 nm)/mCP (10nm)/EML (20 nm)/DPEPO (10 nm)/TmPyPb (30 nm)/LiF (1 nm)/Al (100 nm). ITO, MoO₃, LiF, and Al were used as the anode, hole-injection layer, electron-injection layer and the cathode, respectively. Di-[4-(*N,N*-ditolyl-amino)-phenyl]-cyclohexane (TAPC) and 1,3,5-tri(*m*-pyrid-3-yl-phenyl) benzene (TmPyPB) were used as hole-transport layer (HTL) and electron-transport layer (ETL), respectively. Emitting layers (EML) incorporating 10%-TADF materials in 4,4'-bis(carbazol-9-yl) biphenyl (DPEPO) host were vacuum evaporated. The energy-level diagram of the devices and the molecular structure are shown in **Figure 4.11**.

The current density–voltage–luminance (*J*–*V*–*L*) curve and the EQE versus luminance characteristics of the devices are shown in **Figure 4.12** and **Figure 4.13**, from which the detailed device parameters are extracted and summarized in **Table 4.3**. The OLED devices of Tria-phIDID and BP-phIDID were shown to turn on at 4.4, 4.3 and 4.3 V to give blue emission (EL_{max} at 439, 448 and 448 nm), with CIE coordinates of (0.16,0.08), (0.16,0.13) and (0.16,0.13), respectively. As shown in **Table 4.3**, the maximum luminance efficiency, power efficiency, and external quantum efficiency values for CN-DPS-CBZ were 17.90 cd A⁻¹, 11.71 lm W⁻¹ and 17.7%, respectively and those for CN-DPS-methylCBZ were 22.45 cd A⁻¹, 15.43 lm W⁻¹, 22.2%, respectively and those for CN-DPS-tbuCBZ were 22.96 cd A⁻¹, 14.14 lm W⁻¹, 22.6%, respectively. It indicates that triplet excitons are effectively utilized through the TADF mechanism in the device. But, EQE values of devices decreased to 10.1%, 15.5% and 15.6%

at a luminance of 100 cd m^{-2} . It is likely due to that triplet excitons were quenched by triplet–triplet annihilation (TTA) and singlet–triplet annihilation (STA) at high current density.^[18,19]

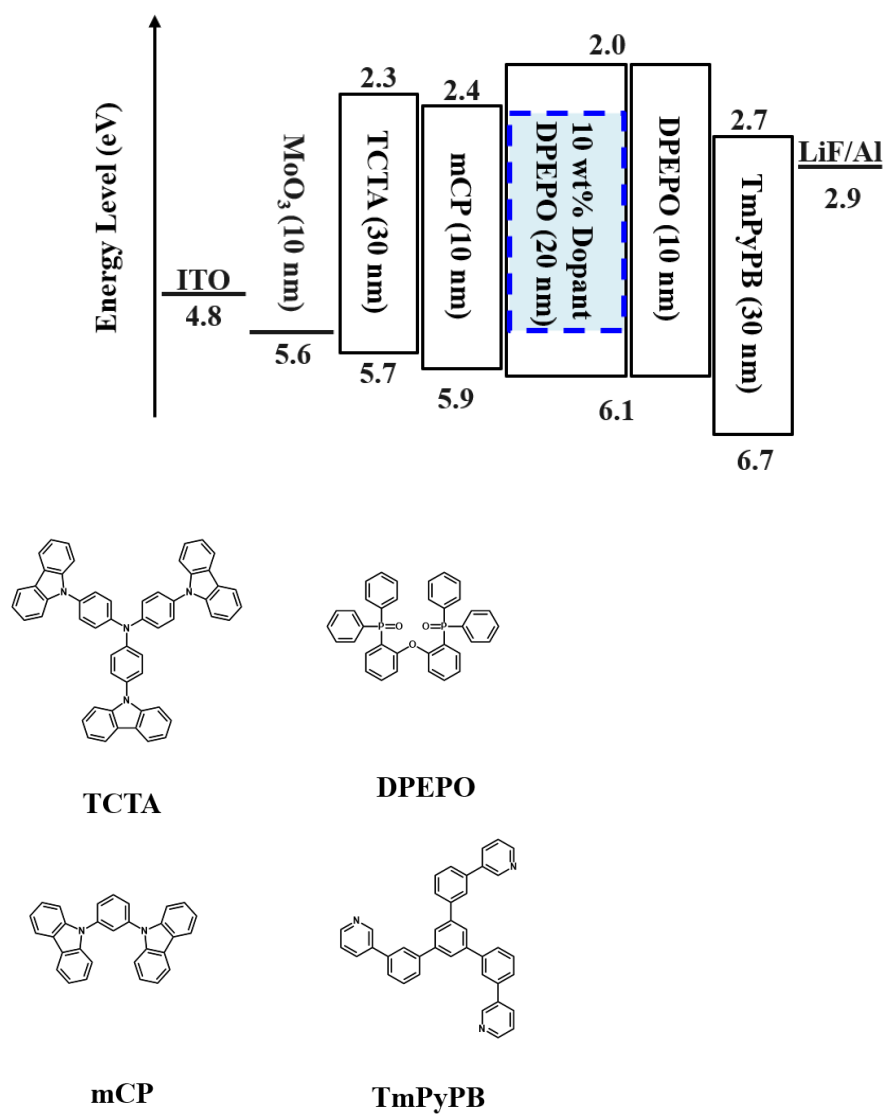


Figure 4.11 the energy-level diagram of the devices and the molecular structure

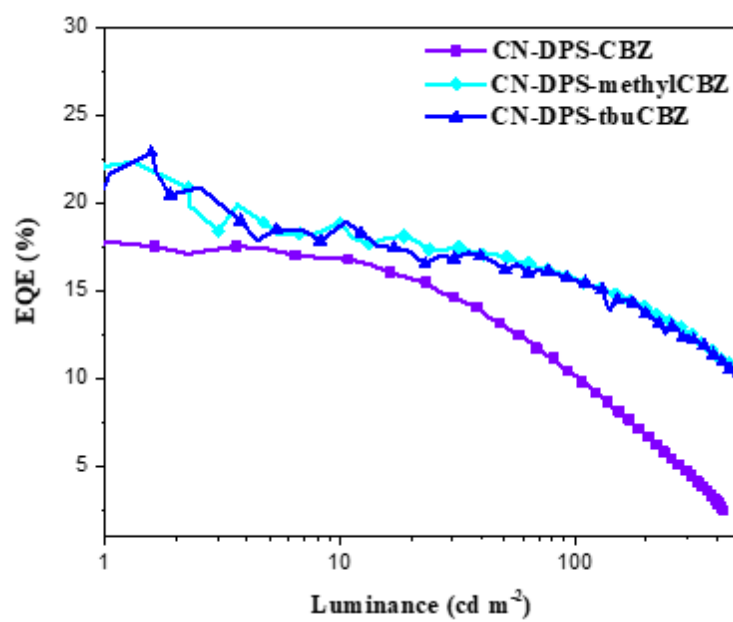


Figure 4.12 External quantum efficiency of OLED devices

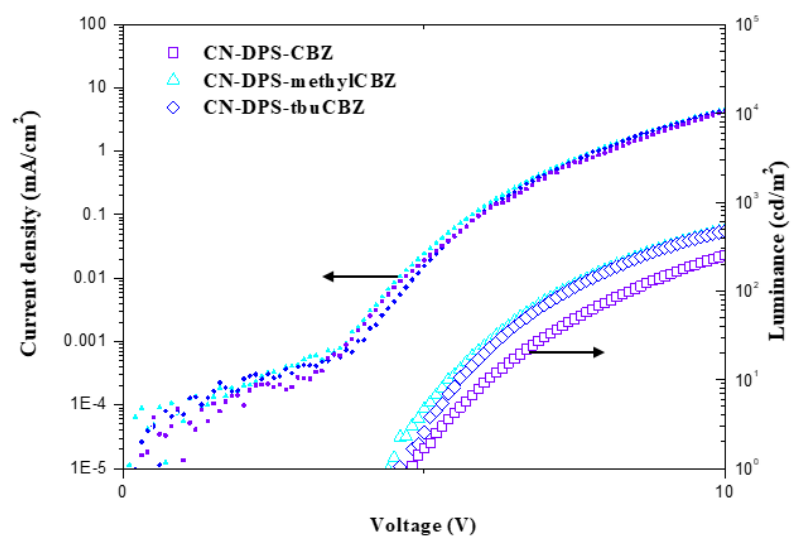


Figure 4.13 *J*-*V*-*L* characteristics of OLED devices

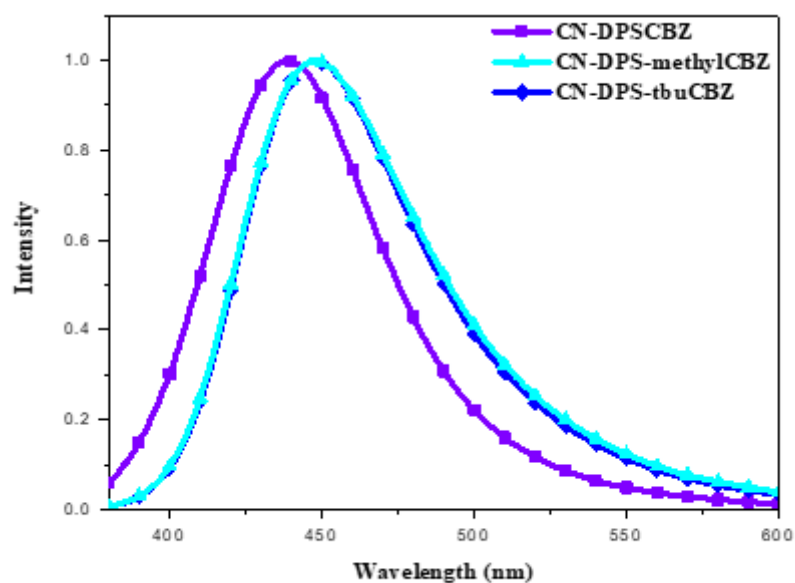


Figure 4.14 EL spectra for OLED devices

Table 4.3. Device performances of the target materials.

	$V_{on}^{a)}$	$\lambda_{max}^{b)}$	FWHM	CIE ^{c)}	$CE_{max}^{d)}$	$PE_{max}^{e)}$	$EQE^{f)}$
	[V]	[nm]	[nm]	(x,y)	[cd A ⁻¹]	[lm W ⁻¹]	[%]
CN-DPS-CBZ	4.4	439	65	(0.16,0.08)	17.90	11.71	17.7
CN-DPS-methylCBZ	4.3	448	71	(0.16,0.13)	22.45	15.43	22.2
CN-DPS-tbuCBZ	4.3	448	70	(0.16,0.13)	22.96	14.14	22.6

^{a)}turn-on voltage at 1 cd m⁻²; ^{b)}EL maximum wavelength; ^{c)}measured at 0.1 mA cm⁻²; ^{d)}maximum current efficiency; ^{e)}maximum power efficiency; ^{f)}maximum external quantum efficiency.

4.4 Conclusion

A new series of CN-substituted molecules were designed and synthesized to develop a high efficiency TADF material. DPS-CBZ exhibited UV ($\lambda_{\text{PL,max}}=386$ nm) fluorescence emission and just a single component of fluorescence lifetime. On the other hand, thanks to ideally control of the energy states, CN substituted emitters show blue region emissions from 425 to 447 nm and exhibit delayed lifetime. Organic light emitting diodes (OLEDs) based blue emitters exhibit efficient external quantum efficiency from 17.7% to 22.6%.

4.5 References

- [1] C. W. Tang, S. A. VanSlyke, *Applied Physics Letters* **1987**, *51*, 913-915.
- [2] T. Tsujimura, W. Zhu, S. Mizukoshi, N. Mori, K. Miwa, S. Ono, Y. Maekawa, K. Kawabe, M. Kohno, SID Symposium Digest of Technical Papers 2007, 38, 84-88.
- [3] S.-M. Lee, J. H. Kwon, S. Kwon and K. C. Choi, *IEEE Transactions on Electron Devices*, 2017, **64**, 1922-1931.
- [4] M. A. Baldo, D. F. O'Brien, Y. You, A. Shoustikov, S. Sibley, M. E. Thompson and S. R. Forrest, *Nature*, 1998, **395**, 151-154.
- [5] J. R. L. a. R. Joseph, Principles of fluorescencespectroscopy, Springer Science & Business Media 2013.
- [6] F. B. V. Sivasubramaniam, S. Hanning, H. P. Loebl, V. van 24 Elsbergen, H. Boerner, U. Scherf and M. Kreyenschmidt, *J. Fluorine Chem.* 2009, 130.
- [7] A. H. a. B. K. n. S. Schmidbauer, *Adv. Mater.* 2013, 25.
- [8] S. Hirata, Y. Sakai, K. Masui, H. Tanaka, S. Y. Lee, H. Nomura, N. Nakamura, M. Yasumatsu, H. Nakanotani, Q. S. Zhang, K. Shizu, H. Miyazaki, C. Adachi, *Nature Materials* **2015**, 14, 330-336.
- [9] H. Kaji, H. Suzuki, T. Fukushima, K. Shizu, K. Suzuki, S. Kubo, T. Komino, H. Oiwa, F. Suzuki, A. Wakamiya, Y. Murata, C. Adachi, *Nat Commun* **2015**, 6, 8476.
- [10] Q. S. Zhang, D. Tsang, H. Kuwabara, Y. Hatae, B. Li, T. Takahashi, S. Y. Lee, T. Yasuda, C. Adachi, *Adv. Mater.* **2015**, 27, 2096-2100.
- [11] M. N. BerberanSantos, J. M. M. Garcia, *J. Am. Chem. Soc.* **1996**, 118, 9391-9394.
- [12] A. Endo, M. Ogasawara, A. Takahashi, D. Yokoyama, Y. Kato, C. Adachi, *Adv. Mater.* **2009**, 21, 4802-4806.

- [13] A. Endo, K. Sato, K. Yoshimura, T. Kai, A. Kawada, H. Miyazaki, C. Adachi, *Appl. Phys. Lett.* **2011**, 98, 083302.
- [14] H. Uoyama, K. Goushi, K. Shizu, H. Nomura, C. Adachi, *Nature* **2012**, 492, 234-238.
- [15] Q. S. Zhang, H. Kuwabara, W. J. Potscavage, S. P. Huang, Y. Hatae, T. Shibata, C. Adachi, *J. Am. Chem. Soc.* **2014**, 136, 18070-18081.
- [16] C. H. Ryoo, J. Han, J.-h. Yang, K. Yang, I. Cho, S. Jung, S. Kim, H. Jeong, C. Lee, J. E. Kwon, I. E. Serdiuk, S. Y. Park, *Advanced Optical Materials* n/a, 2201622.
- [17] Z. Yang, Z. Mao, X. Zhang, D. Ou, Y. Mu, Y. Zhang, C. Zhao, S. Liu, Z. Chi, J. Xu, Y.-C. Wu, P.-Y. Lu, A. Lien, M. R. Bryce, *Angewandte Chemie International Edition* 2016, 55, 2181.
- [18] Masui, K.; Nakanotani, H.; Adachi, C, *Org. Electron.* **2013**, 14, 2721-2726.
- [19] Zhang, Y.; Forrest, S. R, *Phys. Rev. Lett.* **2012**, 108, 267404.

Chapter5. Multiple Resonance Thermally Activated Delayed

Fluorescence Enhanced by Tetraphenyl Silyl Group

5.1. Introduction

Organic light-emitting diodes (OLEDs) have attracted tremendous attention across the academic and industrial field since the pioneering work of Tang *et al.*^[1] Although OLEDs have recently been developed that can be employed in display panels, there remain several problems to be overcome, which is the poor performance of deep-blue OLEDs compared with green and red OLEDs.^[2] Although the color coordinates are satisfied in blue fluorescent emitters, there are a limit of maximum theoretical internal quantum efficiency (IQE) of 25%.^[3] While phosphorescent emitters achieve maximum IQE of 100%, development of new emitters are still demanded because phosphorescent dyes contain expensive and rare noble-metal to satisfy their emitting mechanism and highly efficient blue emitters are still absent.^[4-5]

Recently, an approach to solve the blue problem by using the TADF mechanism is actively progressing due to achieve 100% (IQE) of electroluminescence through the reverse intersystem crossing (rISC) process of pure organic molecules.^[6-9] Adachi et al. first embodied a molecular design strategy by using intramolecular charge transfer (ICT) mechanism between electron donor (D) and acceptor (A) units which spatially separates the highest occupied molecular orbital (HOMO) and lowest unoccupied molecular orbital (LUMO) to minimize ΔE_{ST} .^[10-13] Even though donor-acceptor (D-A) type TADF materials have exhibited great device performance, these CT characteristic emitters have problems of color purity due to broad emission spectra with a wide full width at half- maximum (FWHMs) and hard to realize the deep blue emission with CIE_y < 0.08.

As an alternative, Hatakeyama et al. demonstrated new type of molecular design

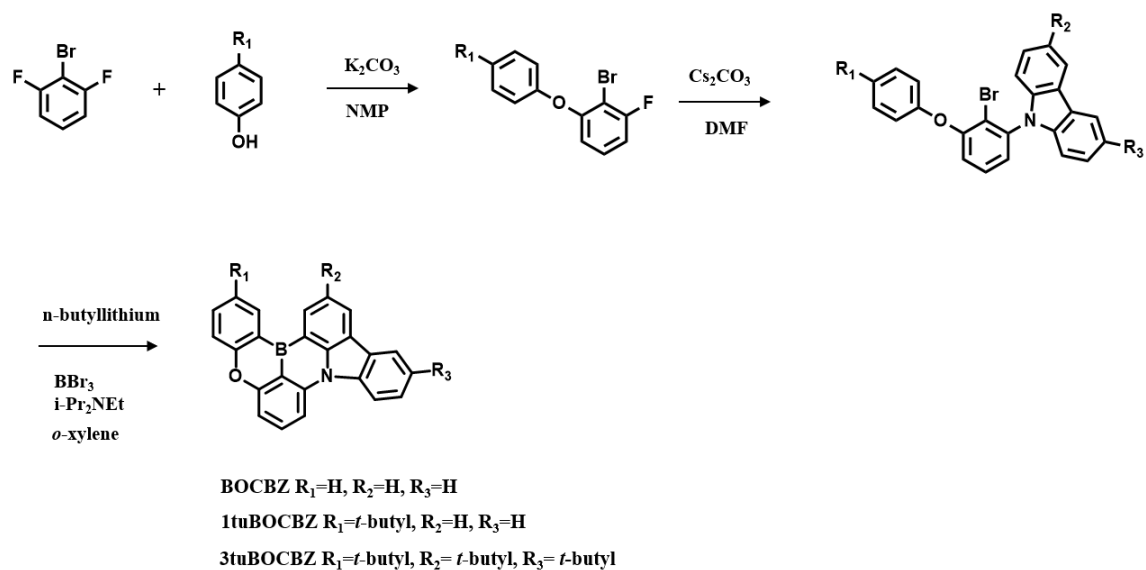
strategy by using a multiple resonance (MR) effect.[14] It has rigid π -conjugated structure consisting of an electron-deficient boron atom and an electron-rich nitrogen atom, exhibiting alternating HOMO and LUMO distributions by the resonance effect. The rigid backbone structure suppressed vibrational motions and guarantee a small full width at half-maximum (FWHM).

The first MR-TADF materials, DABNA-1 and DABNA-2, showed blue emission of 459 and 469 nm for DABNA-1 and DABNA-2, respectively. Also, they exhibited high EQE values of 13.5% and 20.2% with color coordinates of (0.13, 0.09) and (0.12, 0.13). Since then, a number of MR-TADF materials have been developed and ν -DABNA developed by Hatakeyama group.

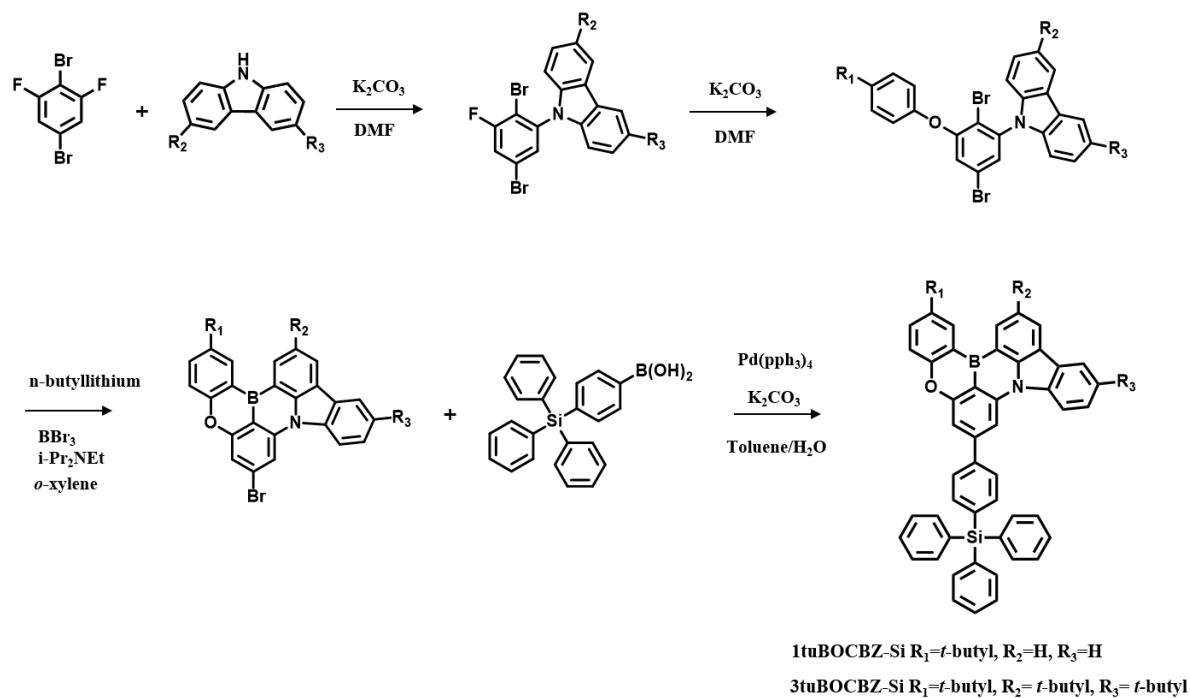
[15] ν -DABNA is a fused form of two boron atoms and six nitrogen atoms and it exhibited a maximum emission wavelength of 469 nm and a half width of 18 nm, so it is known as the state-of-art blue light-emitting material. However, ν -DABNA has a slight unsatisfactory result in blue color. Therefore, development of deep blue MR type emitters is still demanded and challenging work. [16]

We designed and synthesized BOCBZ unit. In addition, to reduce intermolecular interactions, t-butyl group and tetraphenyl silyl group were introduced on BOCBZ units. Particularly The tetraphenyl silyl group is a bulky group and has the advantage of not only increasing the thermal stability of the material, but also has effect on energy states of the material. Systematically photophysical studies were carried out to explore their potential in high efficiency blue OLED application.

5.2 Experimental Methods



Scheme 5.1 Synthetic routes of MR TADF materials.



Scheme 5.2 Synthetic routes of MR TADF materials.

5.2.1 Synthesis of Materials

All reagents were purchased from Sigma Aldrich, TCI, and Alfa Aesar. All experimental glassware was dried in an oven, and all experimental conditions were conducted in an argon or nitrogen environment. The target IDID material were synthesized through the following **scheme 5.1** and **scheme 5.2**.

5.2.2 Characterization

Chemical structures were identified by ^1H NMR (Bruker, ADVANCE-300 and ADVANCE-500), ^{13}C NMR (Bruker, Advance-500), high-resolution mass spectrometry (AB SCIEX, Q-TOF 5600), and elemental analysis (Thermo Fisher Scientific, Flash 1112). UV-vis absorption spectra were recorded using a SHIMADZU UV-1650PC. Steady-state photoluminescence (PL) spectra were obtained with a PTI QuantaMaster 40 spectrofluorometer at room temperature and absolute PL quantum yields (PLQY) were recorded using a 3.2 inch integrating sphere. Low temperature photoluminescence spectra were measured using a Jasco FP-6500 at 77 K. Photoluminescence decay traces were obtained through the time correlated single photon counting (TCSPC) techniques by using a PicoQuant, FluoTime 250 instrument (PicoQuant, Germany). A 377 nm pulsed laser was used as an excitation source and temperature dependent studies were made with a cryostat (Oxford Instruments, Optistat DN). Data analyses were performed using exponential fitting models by FluoFit software. Cyclic voltammetry measurements were performed using a 273A (Princeton Applied Research). Each oxidation potential was calibrated using ferrocene as a reference. LUMO levels were evaluated from the HOMO level and the optical band gap which was obtained from the edge of the absorption spectra. DFT calculations were performed in the gas phase using Gaussian 09 quantum-chemical package. The geometry optimization for ground state of IDID derivatives was carried out using B3LYP functionals with 6–31G (d, p) basis set. TD-DFT calculations were performed

using same functional and basis sets that were used.

5.3 Results and Discussion

5.3.1 Density Functional Theory Calculations

The optimized geometry and electronic properties were calculated by density functional theory (DFT) and time-dependent DFT (TD-DFT) using the B3LYP functional and the 6-31G** basis set (**Figure 5.1, Figure 5.2, Figure 5.3 and Table 5.1**). BOCBZ derivatives showed similar orbital distribution. The LUMO were predominantly located on the boron atom and *ortho/para* positions of boron atom, while HOMO was resided on nitrogen atom and *meta* position of boron atom. Thus, we could expect that the BOCBZ derivatives exhibited multiple resonance TADF properties due to their well-separated HOMO/LUMO arrangement. BOCBZ, 1tbuBOCBZ, 3tbuBOCBZ, 1tbuBOCBZ-Si and 3tbuBOCBZ-Si exhibited calculated HOMO levels of -5.40, -5.34, -5.21, -5.34 and -5.22 eV, respectively. The LUMO level were calculated -1.78, -1.73, -1.67, -1.81 and -1.75 eV, respectively. The band gaps are 3.62, 3.61, 3.54, 3.54 and 3.47 eV, respectively. The calculated singlet levels are 3.11, 3.10, 3.04, 3.05 and 2.98 eV and triplet levels are 2.65, 2.63, 2.59, 2.59 and 2.54 eV. The ΔE_{ST} value is 0.46, 0.46, 0.45, 0.46 and 0.44 eV for BOCBZ, 1tbuBOCBZ, 3tbuBOCBZ, 1tbuBOCBZ-Si and 3tbuBOCBZ-Si, respectively.

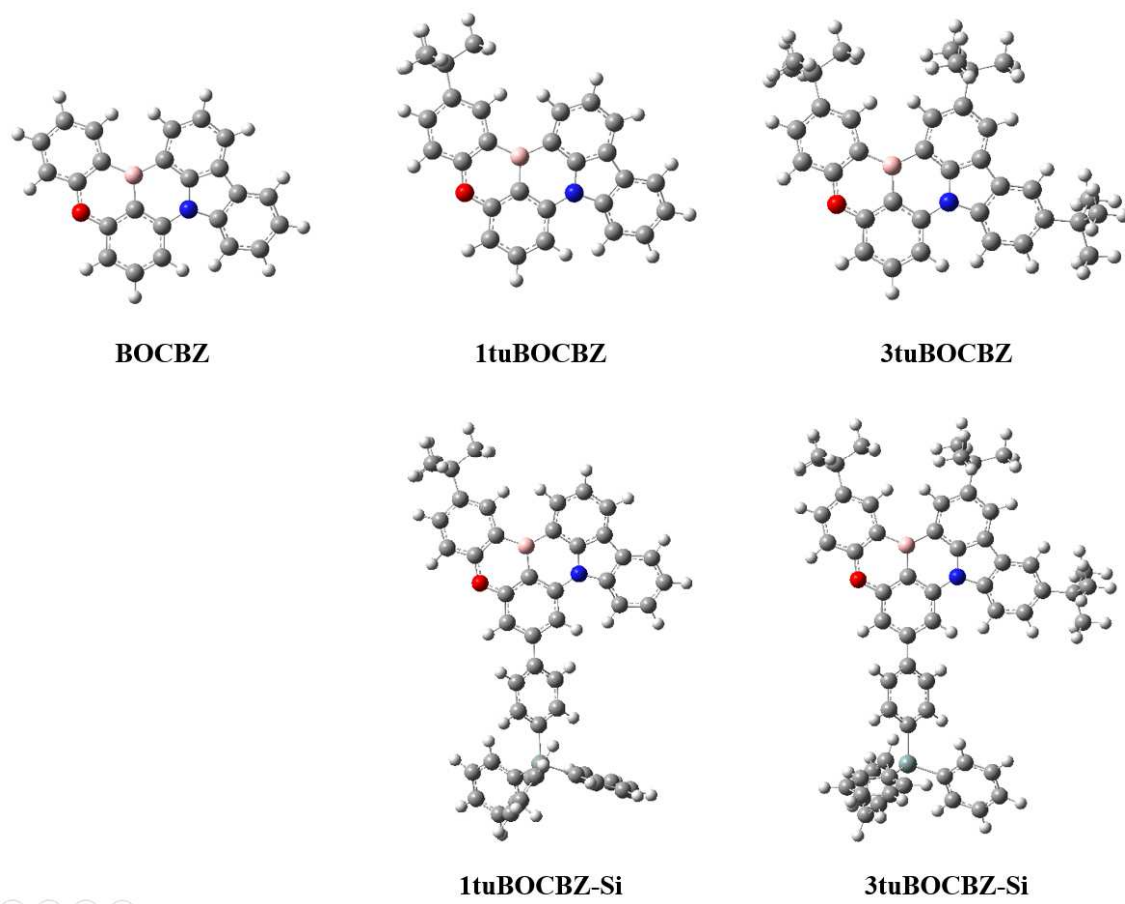
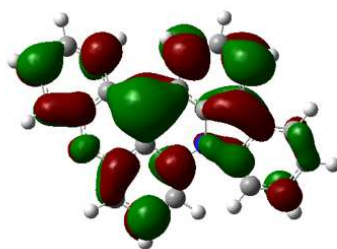
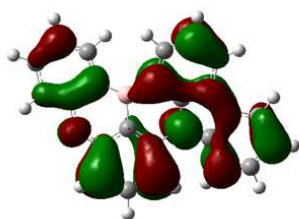


Figure 5.1 Optimized molecular geometries of BOCBZ derivatives.

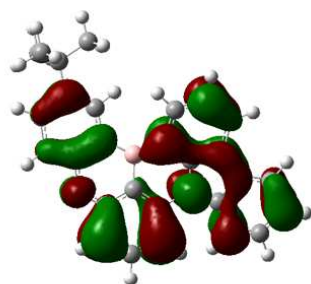
HOMO

LUMO

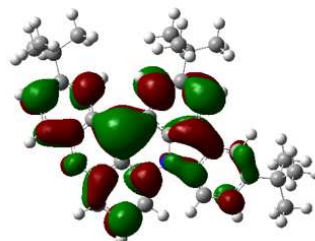
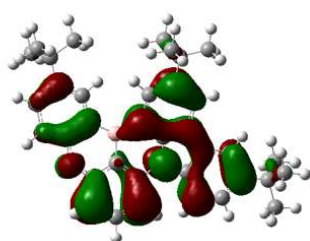
BOCBZ



1tuBOCBZ



3tuBOCBZ



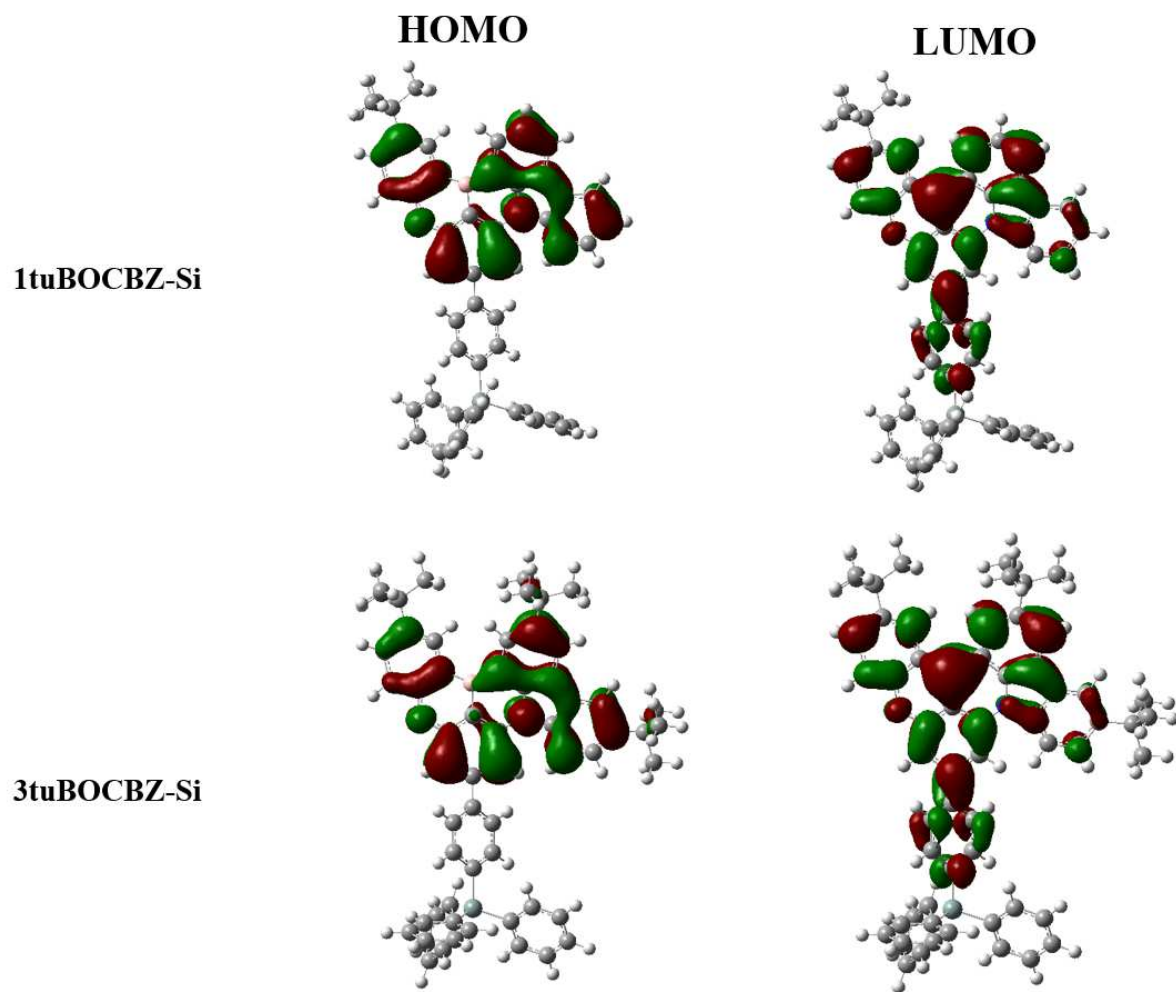


Figure 5.2 Optimized molecular geometries with HOMO and LUMO.

Table 5.1 DFT-calculation of target materials.

	E_g (eV)	HOMO (eV)	LUMO (eV)	ΔE_{ST} (eV)
BOCBZ	3.62	-5.40	-1.78	0.46
1tbuBOCBZ	3.61	-5.34	-1.73	0.46
3tbuBOCBZ	3.54	-5.21	-1.67	0.45
1tbuBOCBZ-Si	3.54	-5.34	-1.81	0.46
3tbuBOCBZ-Si	3.47	-5.22	-1.75	0.44

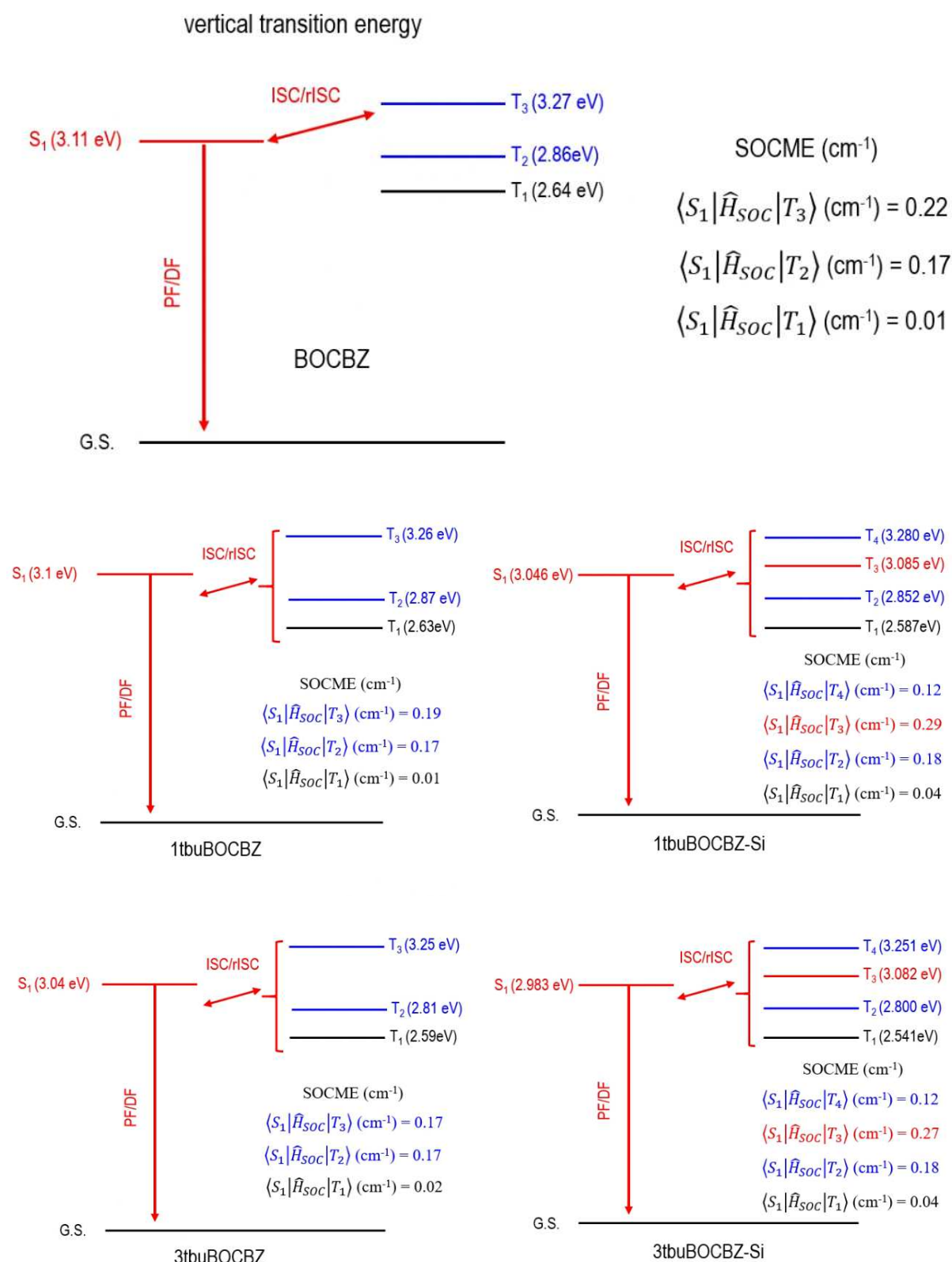


Figure 5.3 Transition energies for S_1 and T_n states ($n=1,2,3$ and 4) and associated SOC matrix elements.

5.3.2 Electrochemical Properties

In order to evaluate the energy level of these compounds, cyclic voltammetry (CV) was carried out in methylene chloride solution using ferrocene as a reference (**Figure 5.4**). BOCBZ, 1tbuBOCBZ and 3tbuBOCBZ exhibited HOMO levels of -5.50, -5.51 and -5.49 eV, respectively. The LUMO level of a material was obtained by adding the optical bandgap to the HOMO level, and were calculated as -2.71, -2.74 and -2.75, respectively. The band gaps are 2.79, 2.77 and 2.74 eV, respectively.

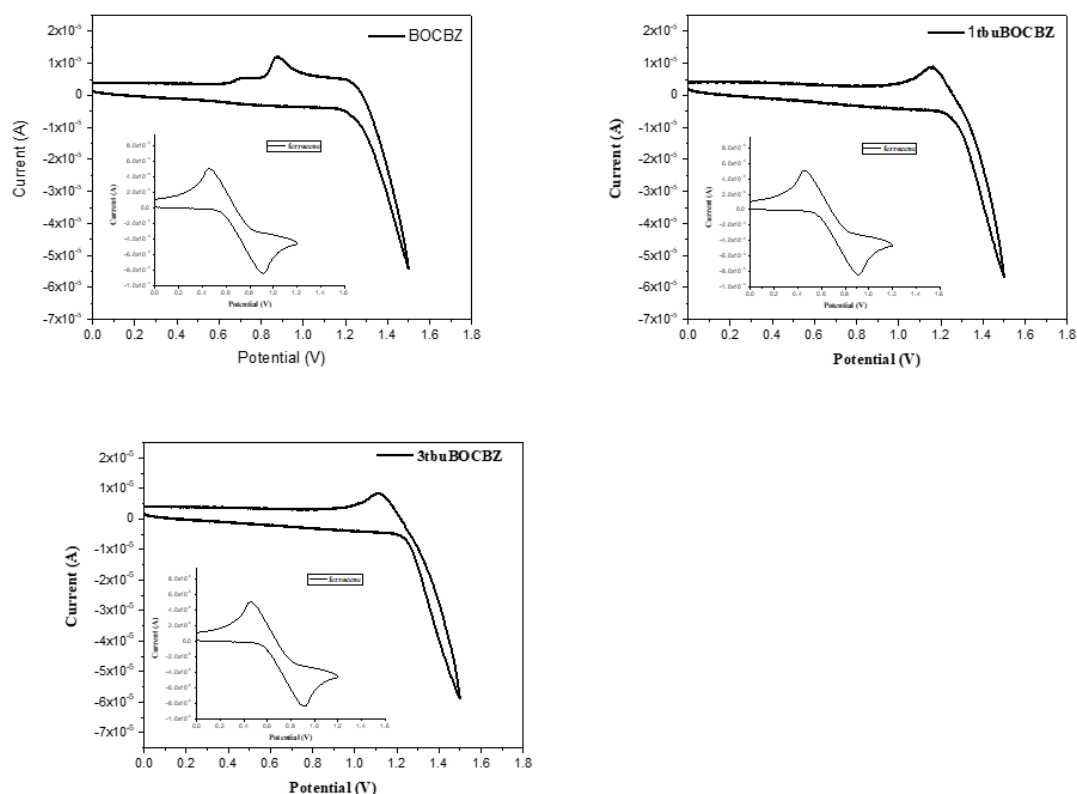


Figure 5.4 Cyclic voltammetry of target materials.

Table 5.2 Cyclic voltammetry of target materials.

	$E_{\text{HOMO, sol.}}(\text{eV})^{\text{a)}$	$E_{\text{LUMO, sol.}}(\text{eV})^{\text{b)}$
BOCBZ	-5.50	-2.71
1tbuBOCBZ	-5.51	-2.74
3tbuBOCBZ	-5.49	-2.75
1tbuBOCBZ-Si	-	-
3tbuBOCBZ-Si	-	-

a) HOMO level was determined by cyclic voltammetry in 5×10^{-3} M methylene chloride solution using ferrocene as a reference.

b) LUMO levels were evaluated with the HOMO level and the optical band gap obtained from the edge of the absorption spectra.

5.3.3 Photophysical Properties

Photophysical properties of target molecules were evaluated by UV-visible absorption (UV-vis) and photoluminescence emission (PL) spectra. (**Figure 5.5**, **Figure 5.6**, **Figure 5.7** and **Table 5.3**). It is shown in **Figure 5.5** that BOCBZ has absorption band below 350 nm and the strong absorption peaks at 427 nm with absorption coefficient (ϵ) of $33700 \text{ M}^{-1}\text{cm}^{-1}$. For 1tbuBOCBZ exhibited similar absorption band ($\lambda_{\text{abs, max}}=427 \text{ nm}$) and ϵ value ($35900 \text{ M}^{-1}\text{cm}^{-1}$) compared to that of BOCBZ. On the other hand, 3tbuBOCBZ showed a 7 nm red-shift of absorption band ($\lambda_{\text{abs, max}}=434 \text{ nm}$, $\epsilon= 38000 \text{ M}^{-1}\text{cm}^{-1}$). The introduction of tetraphenylsilane (-Si) moiety on the BOCBZ units caused bathochromic shift of absorption band. (432 and 438 nm for 1tbuBOCBZ-Si and 3tbuBOCBZ-Si, respectively). Moreover, 1tbuBOCBZ-Si and 3tbuBOCBZ-Si showed the increasing absorption band in UV-light region at around 300 nm - 350 nm, which could be attributed to the π - π^* transition of the tetraphenylsilane (-Si) moieties. The energy gap was estimated from the onset of the absorption band and showed energies of 2.79, 2.77, 2.74, 2.74 and 2.71 eV, respectively.

In toluene solutions, the PL spectra of BOCBZ exhibited deep blue colored emission ($\lambda_{\text{PL,max}}=444$ nm) with 28 nm of FWHM. For 1tbuBOCBZ showed similar emission spectrum ($\lambda_{\text{PL,max}}=444$ nm) and FWHM (28 nm) compared to that of BOCBZ. On the other hand, 3tbuBOCBZ showed a 6 nm red-shift of emission maximum ($\lambda_{\text{PL,max}}=450$ nm, FWHM = 28 nm). The introduction of tetraphenylsilane (-Si) moiety on the BOCBZ units caused bathochromic shift of emission spectrum (449 and 455 nm for 1tbuBOCBZ-Si and 3tbuBOCBZ-Si, respectively) and reducing of FWHM (24 nm for 1tbuBOCBZ-Si and 3tbuBOCBZ-Si).

The emission spectra of these compounds in 1 wt% PMMA film also showed emission wavelength like in solution state. BOCBZ, 1tbuBOCBZ, 3tbuBOCBZ, 1tbuBOCBZ-Si and 3tbuBOCBZ-Si exhibited maximum emission wavelength at 443 nm (FWHM of 38 nm), 444 nm (FWHM of 41 nm), 448 nm (FWHM of 34 nm), 452 nm (FWHM of 45 nm) and 457 nm (FWHM of 38 nm), respectively. The values of PL quantum yields (PLQYs, Φ_{PL}) are 0.91, 0.92, 0.91, 0.91 and 0.90, respectively.

The transient decay lifetime measurement was carried out to explore different emission components of the target molecules using the Time Correlated Single Photon Counting (TCSPC) technique in 1 wt% PMMA film (**Figure 5.8**). Notably, decay profiles of all compounds consisted not only of the prompt fluorescence (PF) but also of the delayed fluorescence (DF). The delayed fluorescence lifetime (τ_{DF}) of BOCBZ, 1tbuBOCBZ, 3tbuBOCBZ, 1tbuBOCBZ-Si and 3tbuBOCBZ-Si were measured to be 35.5, 33.9, 30.4, 27.2 and 25.6 μs , respectively (**Table 5.4**).

We further analyzed the exciton dynamics of the S_1 and T_n states on the basis of the ir photophysical transition rates. The rate constants of radiative process were obtained from PLQY and PF lifetime data (Table 4.4). The k_{RISC} values of the BOCBZ, 1tbuBOCBZ, 3tbuBOCBZ, 1tbuBOCBZ-Si and 3tbuBOCBZ-Si were measured to be 4.34,

4.61, 5.06, 6.942 and $7.50 \times 10^4 \text{ s}^{-1}$, respectively. The compounds with the tetraphenylsilane (-Si) moiety RISC rate faster than that of the BOCBZ compounds, indicating that triplet up-conversion occurs efficiently in the case of the tetraphenylsilane-substituted materials. According to TD-DFT (**Figure 5.3**), 1tbuBOCBZ-Si and 3tbuBOCBZ-Si showed additional triplet state (T_3 state; 3.085 and 3.082 eV) with improving SOMCE (0.29 and 0.27 cm^{-1}). The attachment of the tetraphenylsilane (-Si) unit dispersed the LUMO, improved CT characteristics, and shortened the delayed fluorescence lifetime. Additionally, $\langle S_1 | \hat{H}_{SOC} | T_1 \rangle$ of 1tbuBOCBZ-Si and 3tbuBOCBZ-Si was improved by the heavy-atom effect of Si atoms, similar to S and Se atoms in MR-TADF.

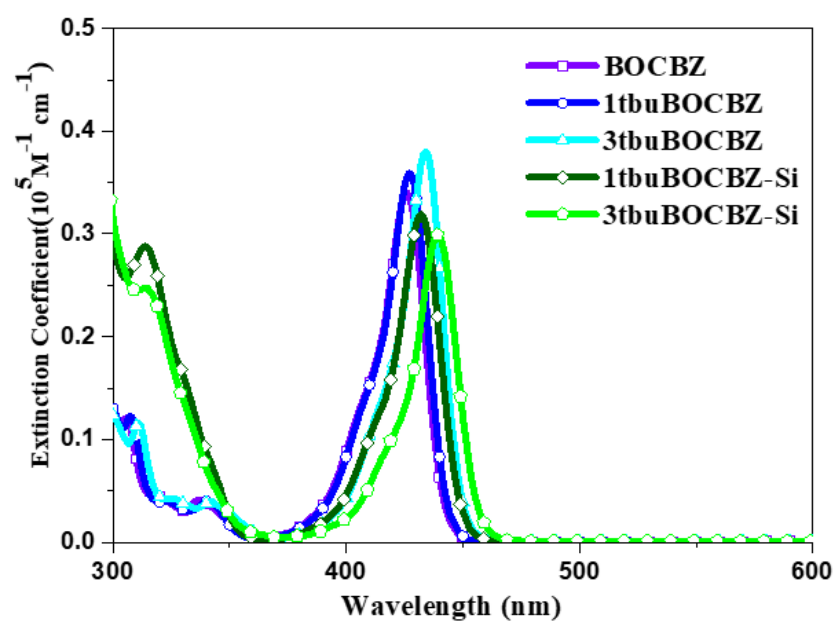


Figure 5.5 Absorption spectra of target molecules. (toluene, $c=1 \times 10^{-5} \text{ M}$)

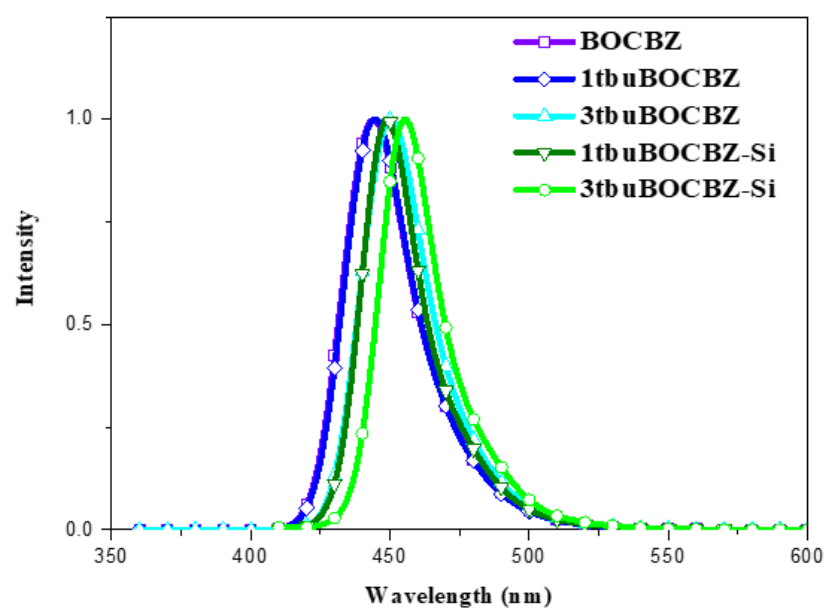


Figure 5.6 Normalized photoluminescence spectra of target molecules. (toluene, $c=1 \times 10^{-5} \text{ M}$)

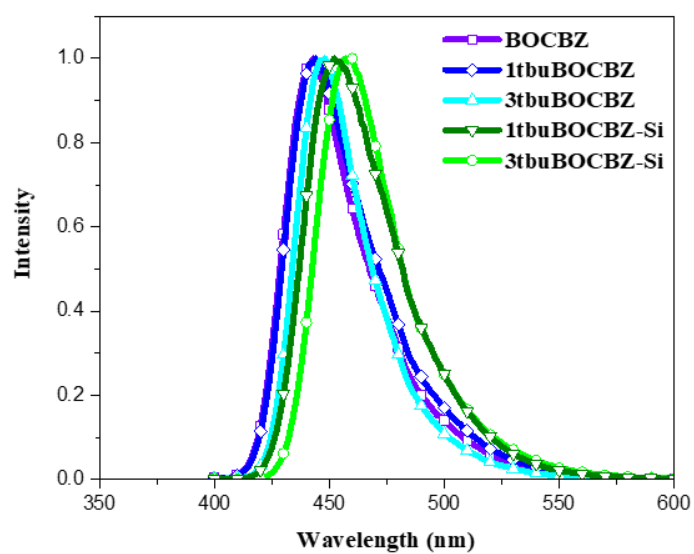


Figure 5.7 Normalized photoluminescence spectra of target molecules.
(1 wt% in PMMA film)

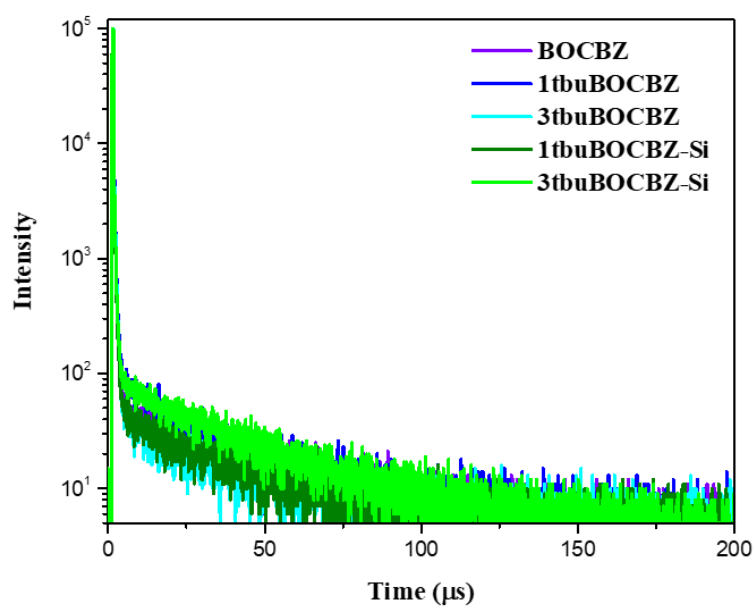


Figure 5.8 Temperature-dependent PL decay spectra (1 wt% in PMMA film).

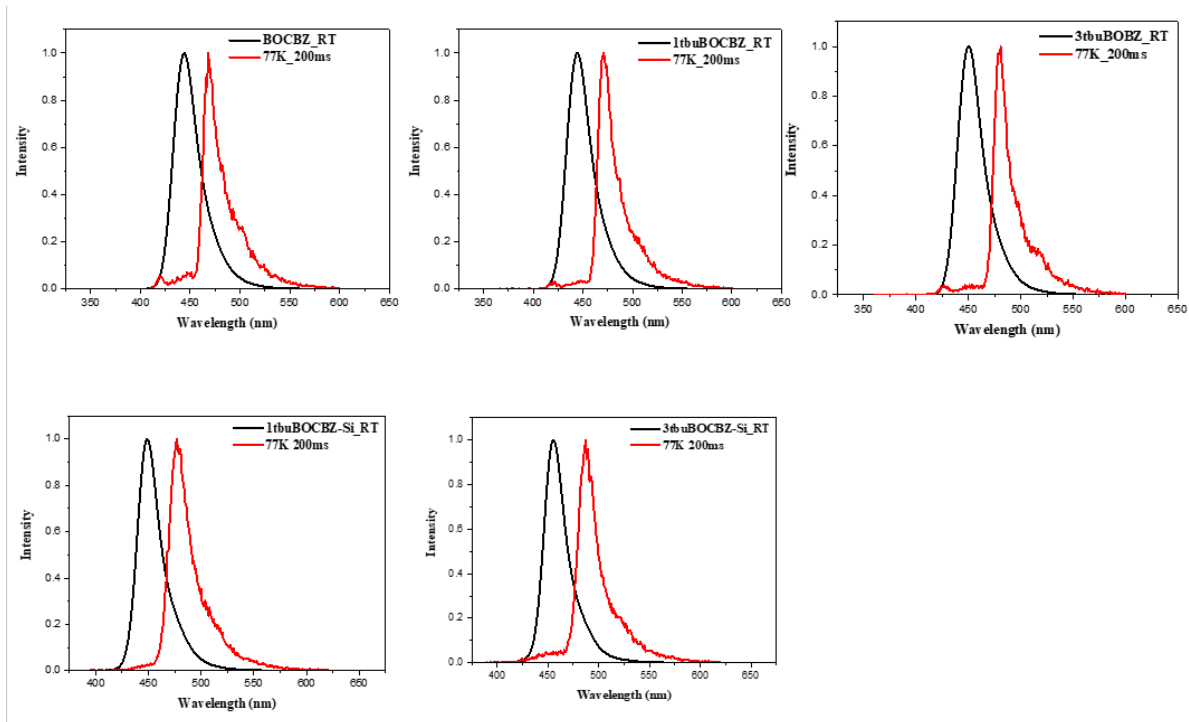


Figure 5.9 Fluorescence and phosphorescence spectra (toluene, $c=1 \times 10^{-5} \text{M}$)

Table 5.3 The summary of physical and photophysical properties of BOCBZ derivatives.

	$\lambda_{\text{abs,max}}^{\text{a)}$	$\epsilon^{\text{a)}$	Band gap	$\lambda_{\text{PL,max}}^{\text{b/c)}$	FWHM	$\Delta E_{\text{ST}}^{\text{d)}$
	[nm]	[$\text{M}^{-1} \text{cm}^{-1}$]	[eV]	[nm]	[nm]	[eV]
BOCBZ	427	33700	2.79	444/443	28/38	0.24
1tbuBOCBZ	427	35900	2.77	444/444	28/41	0.25
3tbuBOCBZ	434	38000	2.74	450/448	28/34	0.25
1tbuBOCBZ-Si	432	31900	2.74	449/452	24/45	0.20
3tbuBOCBZ-Si	438	29600	2.71	455/457	24/38	0.20

^{a)} UV-vis absorption and PL spectra measured in $1 \times 10^{-5} \text{M}$ toluene solution. ^{b,c)} PL spectra measured in $1 \times 10^{-5} \text{M}$ toluene solution and 1 wt% PMMA doping films. ^{d)} Energy gap between S_1 and T_1 estimated from the fluorescence and the phosphorescence spectra in $1 \times 10^{-5} \text{M}$ toluene solution.

Table 5.4 The summary of rate constants of BOCBZ derivatives in PMMA films.

	$\tau_{PF}^{a)}$	$\tau_{DF}^{a)}$	$\Phi_{PF}^{b)}$	$\Phi_{DF}^{b)}$	k_r	k_{nr}	k_{ISC}	k_{rISC}
	[ns]	[μ s]	[%]	[%]	[10^7 s^{-1}]	[10^6 s^{-1}]	[10^7 s^{-1}]	[10^4 s^{-1}]
BOCBZ	9.1	35.47	0.59	0.32	6.50	6.43	3.85	4.34
1tbuBOCBZ	9.2	33.89	0.59	0.33	6.40	5.57	3.91	4.61
3tbuBOCBZ	10.8	30.39	0.59	0.32	5.48	5.42	3.24	5.06
1tbuBOCBZ-Si	9.6	27.20	0.48	0.43	5.02	4.97	4.90	6.94
3tbuBOCBZ-Si	9.8	25.64	0.47	0.43	4.78	5.31	4.90	7.50

^{a)}Lifetime calculated from the prompt (τ_{PF}) and delayed (τ_{DF}) fluorescence decay in PMMA 1 wt% doping films; ^{b)} Φ_{PF} (the prompt PLQY) and Φ_{DF} (the delayed PLQY) were obtained from the prompt and delayed proportions in transient decay curves of 1 wt% PMMA doping films; k_r , k_{nr} – the rate constant of radiative and nonradiative decay of singlet excited state; k_{ISC} , k_{rISC} – rate constant of intersystem crossing and reverse intersystem crossing.

5.4 Conclusion

A new series of MR-type TADF molecules were designed and synthesized to develop a high efficiency blue TADF material. BOCBZ emitters were effective in achieving a real deep-blue emission from 444 to 455 with high PLQY. Particularly, compounds with the tetraphenylsilane (-Si) moiety RISC rate faster than that of the BOCBZ compounds, indicating that triplet up-conversion occurs efficiently in the case of the tetraphenylsilane-substituted materials. It could be forming an additional triplet state enhancing SOC between S_1 and T_n state. Additionally, $\langle S_1 | \hat{H}_{SOC} | T_1 \rangle$ of 1tbuBOCBZ-Si and 3tbuBOCBZ-Si was improved by the heavy-atom effect of Si atoms, similar to S and Se atoms in MR-TADF.

5.5 References

- [1] C. W. Tang, S. A. VanSlyke, *Applied Physics Letters* **1987**, *51*, 913-915.
- [2] J. R. L. a. R. Joseph, Principles of fluorescencespectroscopy, Springer Science & Business Media 2013.
- [3] Z. Xu, B. Z. Tang, Y. Wang and D. Ma, *Journal of Materials Chemistry C*, 2020, **8**, 2614-2642.
- [4] F. B. V. Sivasubramaniam, S. Hanning, H. P. Loeb, V. van 24 Elsbergen, H. Boerner, U. Scherf and M. Kreyenschmidt, *J. Fluorine Chem.* 2009, 130.
- [5] A. H. a. B. K. n. S. Schmidbauer, *Adv. Mater.* 2013, 25.
- [6] S. Hirata, Y. Sakai, K. Masui, H. Tanaka, S. Y. Lee, H. Nomura, N. Nakamura, M. Yasumatsu, H. Nakanotani, Q. S. Zhang, K. Shizu, H. Miyazaki, C. Adachi, *Nature Materials* **2015**, *14*, 330-336.
- [7] H. Kaji, H. Suzuki, T. Fukushima, K. Shizu, K. Suzuki, S. Kubo, T. Komino, H. Oiwa, F. Suzuki, A. Wakamiya, Y. Murata, C. Adachi, *Nat Commun* **2015**, *6*, 8476.
- [8] Q. S. Zhang, D. Tsang, H. Kuwabara, Y. Hatae, B. Li, T. Takahashi, S. Y. Lee, T. Yasuda, C. Adachi, *Adv. Mater.* **2015**, *27*, 2096-2100.
- [9] M. N. BerberanSantos, J. M. M. Garcia, *J. Am. Chem. Soc.* **1996**, *118*, 9391-9394.
- [10] A. Endo, M. Ogasawara, A. Takahashi, D. Yokoyama, Y. Kato, C. Adachi, *Adv. Mater.* **2009**, *21*, 4802-4806.
- [11] A. Endo, K. Sato, K. Yoshimura, T. Kai, A. Kawada, H. Miyazaki, C. Adachi, *Appl. Phys. Lett.* **2011**, *98*, 083302.
- [12] H. Uoyama, K. Goushi, K. Shizu, H. Nomura, C. Adachi, *Nature* **2012**, *492*, 234-238.

- [13] Q. S. Zhang, H. Kuwabara, W. J. Potscavage, S. P. Huang, Y. Hatae, T. Shibata, C. Adachi, *J. Am. Chem. Soc.* **2014**, 136, 18070-18081.
- [14] T. Hatakeyama, K. Shiren, K. Nakajima, S. Nomura, S. Nakatsuka, K. Kinoshita, J. Ni, Y. Ono and T. Ikuta, *Adv Mater*, 2016, **28**, 2777-2781.
- [15] Y. Kondo, K. Yoshiura, S. Kitera, H. Nishi, S. Oda, H. Gotoh, Y. Sasada, M. Yanai and T. Hatakeyama, *Nature Photonics*, 2019, **13**, 678-682.
- [16] Zhang, Y.; Zhang, D.; Wei, J.; Liu, Z.; Lu, Y.; Duan, L, *Angew. Chem., Int. Ed.* 2019, 131, 17068–17073.
- [17] Oda, S.; Kawakami, B.; Kawasumi, R.; Okita, R.; Hatakeyama, T. *Org. Lett.* 2019, 21, 9311–9314.
- [18] Sun, D.; Suresh, S. M.; Hall, D.; Zhang, M.; Si, C.; Cordes, D. B.; Slawin, A. M.; Olivier, Y.; Zhang, X.; Zysman-Colman, E, *Mater. Chem. Front.* 2020, 4, 2018–2022.
- [19] Qiu, X.; Tian, G.; Lin, C.; Pan, Y.; Ye, X.; Wang, B.; Ma, D.; Hu, D.; Luo, Y.; Ma, Y. *Adv. Opt. Mater.* 2021, 9, No. 2001845.

국 문 초 록 (Korean Abstract)

유기발광다이오드를 위한 신규 열 활성화 지연 형광체의 분자 설계 및 합성에 관한 연구

유기발광 다이오드(organic light emitting diode, 이하 ‘OLED’ 로 지칭)는 발광원리와 그 소자의 구동원리의 특성상 백라이트유닛(back light unit)이 필요 없어 기기의 소형·초박형화에 적합하며, 구동 전력이 낮을 뿐 아니라, 높은 색 재현율, 넓은 시야각, 빠른 반응속도 등의 장점으로 기존 디스플레이(LCD, PDP 등)의 한계를 극복할 수 있는 차세대 디스플레이 장치이고, 유기전자분야의 핵심 목표인 유연한 디스플레이(flexible display)를 구현할 수 있는 핵심 기술이다. 이러한 장점들을 기반으로 OLED에 대한 학술적·산업적 연구개발이 활발히 이루어져 소형 전자기기의 디스플레이로서 양산이 이루어져 왔고 점차 대형화가 진행되고 있는 상황이다. 하지만 아직까지는 각 색 요소(청색, 녹색, 적색) 발광체의 발광효율과 소자수명이 개선이 요구되는 상황이며, 특히 고효율 청색 발광체의 부재가 기술적 진전의 최대 난제이다.

OLED 발광 재료는 발광 메커니즘에 따라 형광(fluorescence) 물질과 인광(phosphorescence) 물질로 나뉜다. 전기적 여기에 의한 여기자(exciton)는 양자 통계역학적 생성 비에 의하여 25%의 일중항 여기자(singlet exciton)와 75%의 삼중항 여기자(triplet exciton)로 나뉘게 되는데, 이 중 일중항 여기자가 기저상태(ground state)로 안정화가 되며 내는 빛을 형광이라 하고, 삼중항 여기자가 기저상태로 안정화되며 내는 빛을 인광이라 한다. 따라서 최대 100%의 발광효율을 낼 수 있는 인광체가 고효율 OLED 발광체로서 각광받고 있지만, 소자수명이 짧을 뿐 아니라 전이금속 및 란탄족 등

고비용 희토류 원소를 포함하는 등의 단점이 있다.

최근, 일본 Kyushu 대학의 Adachi group에서는 열활성지연형광(thermally activated delayed fluorescence, 이하 TADF) 현상을 이용한 OLED 소자를 보고 하였다. TADF 현상은 발광체의 일중항과 삼중항의 에너지 준위차가 매우 작아 역계간교차(reverse intersystem crossing)가 상온에서 매우 활발하게 일어날 수 있어, 중원소(heavy atom) 없이도 형광체에서 $\mu\text{s} \sim \text{ms}$ 수준의 발광수명을 갖는 지연된 형광이 발현되는 현상이다. 따라서 일반적인 형광체에서는 사용할 수 없었던 75%의 삼중항 여기자를 활성화시켜 100%의 내부양자효율 구현이 가능한 메커니즘으로, 앞서 언급한 인광체의 단점들을 극복하고 고효율 OLED를 구현할 수 있는 새로운 방안으로써 많은 연구가 활발히 이루어지고 있다. 이러한 배경에서, 본 연구에서는 유기발광다이오드를 위한 신규 열 활성 지연 형광체의 분자 설계 및 합성에 관한 연구를 진행하였다.

Chapter 2에서는 인돌로[3,2-b]인돌 (indolo[3,2-b]indole, 이하 'IDID') 기반의 신규 TADF 전자주개골격 구조로서의 응용 가능성을 확인하기 위하여 연구진행 하였다. 이를 통해서 전 가시광 영역의 IDID 기반 ICT발광체를 확보하였고 이들의 구조 물성 상관관계 분석을 통해서 TADF메커니즘을 규명하였다.

Chapter 3에서는TADF 특성을 유지하되, 발광영역을 능동적으로 조절하고자 ICT 세기를 조절하는 합리적인 분자설계를 하였다(D-A-X 전략). 이를 기반으로 TADF 물질의 에너지를 능동적으로 조절할 수 있었으며, 이들의 구조물서 상관관계 분석을 통해서 꺾여있는 구조에서 분자 진동을 통해서 충분히 ^1CT 와 ^3CT 사이에서 스핀전환이 가능하다는 메커니즘을 규명하였다.

Chapter 4에서는 D-A-X 전략을 자외선 영역의 일반 형광체인 DPS-CBZ에 도입하여 분자 내 전하이동 (Intramolecular Charge Transfer) 특성을 제어하여 청색 TADF 분자를 개발하고자 하였다. 이를 통하여 청색 TADF 발광체를 확보할 수 있었고 성공적으로 OLED로 적용하였다.

Chapter 5에서는 보론과 질소를 적절하게 배치하여 다중공명효과 전략 (multiple resonance effect)을 통해 신규 청색 TADF 발광체를 개발하고자 하였다. 이를 통하여 청색 TADF 발광체인 BOCBZ 유도체를 확보할 수 있었다. 더 나아가 테트라페닐실릴 작용기를 BOCBZ구조체에 도입하여 TADF 특성을 개선한 청색 발광체를 확보하였고 이들의 특성평가를 통하여 유의미한 구조 물성 상관관계를 도출하였다.

학번: 2015-22772